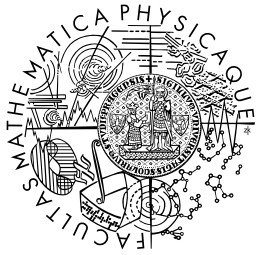

FACULTY
OF MATHEMATICS
AND PHYSICS
Charles University

DOCTORAL THESIS

Michal KNAPEK

Study of cooperative dislocation phenomena in solids by the acoustic emission technique

Department of Physics of Materials

Supervisor of the doctoral thesis:	doc. RNDr. F. Chmelík, CSc.
Study programme:	Physics
Study branch:	Physics of Condensed Matter and Materials Research

Prague 2016

I declare that I carried out this doctoral thesis independently, and only with the cited sources, literature and other professional sources.

I understand that my work relates to the rights and obligations under the Act No. 121/2000 Sb., the Copyright Act, as amended, in particular the fact that the Charles University has the right to conclude a license agreement on the use of this work as a school work pursuant to Section 60 subsection 1 of the Copyright Act.

Prague, August 15, 2016 Michal Knapek

This doctoral thesis would not be possible without the help of many people in many ways. It is also the product of a good number of coincidences and encounters with people who have changed the course of my academic and scientific career. Above all, had not Dr. Aba Teleki and Dr. Boris Lacsný from the Constantine the Philosopher University in Nitra (under whose supervision I did earn my Master degree) made me acquainted with my doctoral supervisor, Prof. František Chmelík, I might not have pursued a scientific career.

I am very grateful to Prof. František Chmelík for introducing me to the profuse fields of Materials science and for his constant support and guidance throughout my doctoral studies. I am also thankful to Dr. Patrik Dobroň for his help with the mechanical tests and lengthy, fruitful discussions ("Patrik, do you have a minute?"), to Prof. Pavel Lukáč for numerous valuable advices and critical reading of the manuscript, and to Dr. Peter Minárik for the discussions and helping me with scanning electron microscopy.

A significant part of the work presented in this thesis was carried out in cooperation with Prof. Andreas Mortensen from the Laboratory of Mechanical Metallurgy, École polytechnique fédérale de Lausanne (EPFL), Switzerland and his team, especially his Ph.D. student Suzanne Verheyden, with whom we worked together on aluminum microwires testing and who took the SEM images. I would also like to thank Dr. Kseniya Illková, who, during her stay at EPFL, prepared metal foams investigated in this thesis.

Development of the experimental set-up and subsequent testing of the micropillars presented in this work took place mainly during my 6-months stay at the Department of Materials Physics, Eötvös Loránd University in Budapest. I am grateful to the head of the department, Prof. István Groma, and his colleagues, namely Dr. Péter Dusán Ispánovity, Ádám Hegyi, Prof. Zoltán Dankházi, and Dr. Gábor Varga for immense effort in refining the experimental procedures and rich discussions about the data interpretation. I am particularly indebted to my colleague Dr. Kristián Máthis who had initiated this collaboration several years ago, helped extensively to make my stay possible, and also participated in the experimental work.

I would also like to thank other members of my home institution—Department of Physics of Materials, Charles University—as well as the members of both host institutions who were not mentioned above, for creating a positive atmosphere and for being always friendly and helpful.

I am grateful to my family and all the friends for their support and trusting in me (often even without knowing what my work was actually about). I would

also like to acknowledge all the great Czech breweries whose products helped me to relax and regain inner strength after working long hours, and, at the same time, my thanks go to many friends and colleagues in Prague, but especially Mariia Zimina, for being always around to team up at such ill moments.

This thesis came into being also on the grounds of the financial support of the Grant Agency of Charles University in Prague (grant No. 94621), and the Czech Science Foundation (grant No. 15-10821S).

-MK-

Title: Study of cooperative dislocation phenomena in solids by the acoustic emission technique

Author: Michal KNAPEK

Department: Department of Physics of Materials

Supervisor: doc. RNDr. František Chmelík, CSc., Department of Physics of Materials

Abstract: Plastic deformation of micron-scale crystalline materials differs considerably from bulk specimens, as it is characterized by random strain bursts. Three categories of metallic samples were investigated in this thesis: micron-scale copper micropillars with varied geometries, submillimeter-scale aluminum microwires, and aluminum and aluminum-magnesium salt-replicated foams. Very precise fabrication methods and sensitive measurement set-ups consisting of uniaxial compression and tensile tests with concurrent acoustic emission (AE) recording were developed. These fine methods allowed for investigations of effects related to plastic deformation at micrometer scales, i.e. the dislocation dynamics associated with the stress drops. Size effects in plastic deformation, as well as clear correlations between the stress drops and the AE events, were found in microsamples, confirming that dislocation avalanches are indeed responsible for the stochastic character of deformation processes also at microscales. Open-cell pure aluminum and aluminum-magnesium foams produced by salt replication with cells between 25 and 400 µm in average diameter and relative densities between 25 and 45 % were also tested as one of the very few materials where, thanks to its structure, the abovementioned effects are manifest also in a bulk form. Size effect in the mechanical properties was evidenced in pure aluminum foams. Moreover, the Portevin-Le Châtelier (PLC) effect was found in the aluminum-magnesium foams. To account for the deformation behavior and the occurrence of PLC effect within such complicated structures, the AE signals accompanying the compression of tested samples were further evaluated using advanced frequency analysis and statistical methods.

Keywords: microsamples; size effect; metal foams; plastic deformation; acoustic emission

Názov práce: Štúdium kooperatívnych dislokačných javov v pevných látkach metódou akustickej emisie

Autor: Michal KNAPEK

Katedra: Katedra fyziky materiálů

Školiteľ: doc. RNDr. František Chmelík, CSc., Katedra fyziky materiálů

Abstrakt: Plastická deformácia kryštalických látok v ráde mikrometrov sa značne líši od správania makroskopických vzoriek, keďže deformácia mikrovzoriek je charakterizovaná náhodnými skokmi na deformačných krivkách. V práci boli skúmané tri typy kryštalických materiálov, a to: medené vzorky typu "micropillar" s rôznymi rozmermi, hliníkové mikrovlákna a hliníkové a hliník-horčíkové peny vyrobené metódou replikácie kompaktovaných soľných foriem. Vyvinuté boli precízne metódy výroby vzoriek a vysokocitlivé meracie zariadenia pozostávajúce z jednoosích tlakových a ťahových skúšok so súčasným záznamom akustickej emisie (AE), ktoré boli použité na skúmanie efektov spojených s plastickou deformáciou v mikrometrických škálach (dynamika dislokačných procesov v súvislosti s nespojitosťami plastickej deformácie). V mikrovzorkách bol objavený bol tzv. veľkostný jav v plastickej deformácii, ako aj priame korelácie medzi skokmi na deformačných krivkách s udalosťami AE. Tento výsledok priamo potvrdzuje, že dislokačné lavíny sú zodpovedné za stochastický charakter deformačných procesov taktiež na mikroškálach. Replikované hliníkové a hliník-horčíkové peny s otvorenými pórmi s priemernou veľkosťou 25–400 µm a relatívnymi hustotami v rozmedzí 25–45 % boli tiež skúmané ako jeden z mála materiálov, v ktorom sa vďaka jeho štruktúre prejavujú vyššie spomínané javy aj v makroskopickom meradle. V hliníkových penách bol taktiež pozorovaný veľkostný jav v mechanických vlastnostiach. V hliník-horčíkových penách sa navyše prejavil tzv. Portevinov-Le Châtelierov (PLC) jav. Na objasnenie deformačných vlastností a PLC javu v rámci výrazne komplikovanej štruktúry kovových pien boli signály AE, ktoré boli generované počas mechanického zaťaženia vzoriek, podrobne analyzované pomocou pokročilej frekvenčnej analýzy a štatistických metód.

Kľúčové slová: mikrovzorky; veľkostný jav; kovové peny; plastická deformácia; akustická emisia

Contents

Introduction

Deformation of metals and other crystalline materials, due to its scientific and application importance, has been the subject of research efforts for a long time. It is well-known that below a certain stress level (called *yield stress*), materials deform in a reversible way, i.e. elastically, and above this level, they typically undergo irreversible changes in shape and structure. The latter phenomenon is called *plastic deformation*. The dominant mechanism for producing plastic strain is the collective motion of mutually interacting *dislocations* (line defects in the crystalline lattice) [1, 2]. Although the movement of an individual, single dislocation produces a finite slip localized at its glide plane, the plastic response of a macroscopic specimen, due to the huge number of moving dislocations, is typically smooth in time and space, thus resembling a viscous flow process. Consequently, the mechanical properties, e.g. the yield stress, have been assumed to be not dependent on the specimen size and shape [3].

It has been discovered very recently, however, that if the size of the specimen is decreased to about 10 µm in at least one direction, this picture changes remarkably. Specifically, the deformation process becomes inhomogeneous both in time and space. Such behavior was first demonstrated on cylindrical Ni single crystals (micropillars) fabricated using the focused ion beam (FIB) technique [2, 4]. It was found that if the pillar diameters ranged from 1 to 40 µm, the stress-strain curves become irregular, exhibiting random serrations. Another, even more intriguing feature, is that this phenomenon is accompanied by a strong size effect, i.e., the small samples become much harder [2, 4]. Since the discovery, identical behavior has been observed in a wide range of fcc materials such as copper [5], aluminium [6], gold [7] and Ni-based superalloys [8], and also for bcc [9–11] and other materials [12–16]. Besides FIB milling, alternative methods have been also developed recently for the production of microsamples, such as preferential etching [17, 18], electroplating through a template [19], or microcasting [20–22]. In [23] the size effect was found in cast aluminum microwires.

The first explanation of size effects was based on the assumption of dislocation depletion, that is, in small specimens dislocations escape the crystal before multiplication can take place [24]. Another breaking observation was the finding that the strain burst events (dislocation avalanches) associated with the steps on the stress-strain curves obey a scale-free size distribution. This result, first revealed by the acoustic emission (AE) experiments on ice single crystals [25], and later by direct measurement on Ni single crystalline micropillars [26] and by computer simulation [25, 27], signifies that dislocation networks may behave as self-organized dynamic systems in the critical state.

Nanotechnology is nowadays already capable of producing numerous new materials and devices on the (sub)micrometer scale [28, 29] and it has become indispensable to understand plasticity of microsamples and its underlying physics. In order to be able to design microdevices, detailed physical properties of the deformation processes should be studied. This is undoubtedly the reason why the investigation of plastic properties of microsamples initiated an extensive research interest in the recent years. The breakthrough experiments described above opened many questions concerning micron-scale crystal plasticity and most of them are linked with collective dislocation dynamics. Research in this field thus represents a timely and world-wide novel scientific activity, having also a great potential for significant technological impact.

Objectives of the thesis

The first experimental evidence on the nature of strain bursts was obtained by detecting AE signals during mechanical loading of specimens [25, 30, 31]. These signals are emitted during the correlated motion of a large number of dislocations, i.e., due to the dislocation avalanches. To date, such measurements have been carried out solely on bulk single- and poly- crystals. Based on the literature review, analogous experiments have not yet been performed on microsamples, such as those that will be investigated in this thesis. To this end, very fine and sensitive experimental set-ups are needed whose development will be described in this work. The experiments on various types of specimens presented here are therefore expected to deliver valuable results on the nature of dislocation origin of the AE signals. Within the studied sizes ($\sim$1–100 µm), the size effects and inhomogeneous deformation should occur, but the crystal remains still large in the sense that it contains enough dislocations to behave in a collective manner.

A significant part of the thesis is devoted to the mechanical properties and AE response of microcellular metallic materials (or "metal foams"). Up to now, there have been only a limited number of studies making use of the AE technique in order to shed more light on the deformation mechanisms in metal foams [32–37]. Moreover, these works focused mainly on the evaluation of the basic AE parameters. It should be stressed that metal foams belong to very few materials in which the abovedescribed size effects can be directly studied on a macroscopic scale. Owing to the fabrication process, the grain size of the metal making the salt-replicated open-cell foams is typically larger than the pore size. Therefore, the structural units of the foam (e.g. struts) are single crystals with dimensions (e.g. strut thickness) approaching scales of microns. Consequently, very fine struts are expected to behave under load in a similar manner as the micropillars. Naturally, due to the complex shape of the foam, many various deformation

modes (bending, torsion, tension, etc.) are concurrently present in contrast to the in contrast to the uniaxial compression of micropillars or tension of microwires. For this reason, finding a link between the macroscopic response and the local behavior on the struts level is rather challenging. On the other hand, the macroscopic metal foam can be tested by any conventional testing methods available for bulk materials. In this thesis, two types of foams will be studied: a) open-cell pure aluminum foams and b) open-cell aluminum foams containing 2 wt. % of magnesium (Al2Mg), both with the pore sizes ranging between 25 and 400 µm. The results from deformation testing of metal foams will be compared with the investigations on single-crystalline copper micropillars of different geometries tested in compression and single-crystalline aluminum microwires tested in tension, all with the simultaneous recording of the AE signal. These results will be supplemented by advanced statistics and signal processing methods.

Based on the objectives outlined above the following results were expected to be achieved:

- Development of sensitive experimental set-ups that will allow for simultaneous recording of deformation and acoustic response of mechanically-loaded microsamples, thus utilizing the AE technique (as a method which proved many times to be very effective in studying deformation dynamics of bulk materials) also at microscales.
- Experimental examination of statistical properties of stress drops by coupling the copper micropillar compression and aluminum microwire tensile tests with the AE measurements.
- Elucidation of an influence of microscopic size effects on the properties of macroscopic metal foam specimens with the help of advanced analyses of the AE signals.
- Assessing the differences in the mechanical and AE response between mechanically loaded pure aluminum foams and aluminum alloyed with 2 wt.% of magnesium foams.

All these novel results are potentially of high scientific interest. Together, they can contribute to a more complete picture of micron-scale plasticity, especially of its stochastic aspects.

1. Theoretical background

1.1 Plastic deformation of bulk face centered cubic (fcc) metals

When load is applied to a metallic single crystal, it undergoes elastic deformation up to a critical point (yield point), where irreversible (plastic) deformation begins to take place. Plastic deformation is typically realized by slip along the closest packed direction (glide direction) in the closest atomic packing plane (glide plane), the combination of which is referred to as a glide or slip system [38]. In fcc single crystals, there are 12 possible glide systems along which plastic deformation can take place. For a single crystal loaded in tension, the plastic deformation begins in the slip system when the shear stress first reaches a critical value (critical resolved shear stress, τ), independent of the tensile stress or any other normal stress on the lattice plane. This critical shear stress is related to the stress required to move dislocations across the slip plane. The critical resolved shear stress is given by the well-known Schmid and Boas relation [39]:

$$\tau = \frac{F}{A_0} \cos\phi \cos\lambda, \tag{1.1}$$

where F is the applied tensile force, A_0 is the initial crystal cross-section perpendicular to the loading direction, ϕ is the angle between the normal of the slip plane and the tensile axis, and λ is the angle between the slip direction and the tensile axis (Fig. 1.1). Thus, the critical resolved shear stress τ is independent on the orientation of the crystal.

Loading a single crystal oriented in a way that the critical resolved shear stress is reached only for one glide system will result in the occurrence of shear bands (steps along the surface of the crystal as the sections of the crystal slide relative to one another). On the other hand, the orientation favourable for activation of more than one glide system will initiate a less straightforward behavior. There is in general a strong influence of the crystal orientation on the mechanical response of tested samples [23]. In other words, the initial yield stress and the shear strain vs. resolved shear stress curves vary from sample to sample depending (among other factors) on the position of the crystal lattice relative to the loading axis.

During the conventional tensile test, the ends of the specimen are constrained. The crystal planes cannot glide freely and thereby they are forced to rotate towards the tensile axis. Thus, the slip plane gradually re-orients as the length of the specimen changes, what can, in turn, lead to the initiation of slip in different systems (see Fig. 1.1). In compression, on the other hand, the slip plane normal

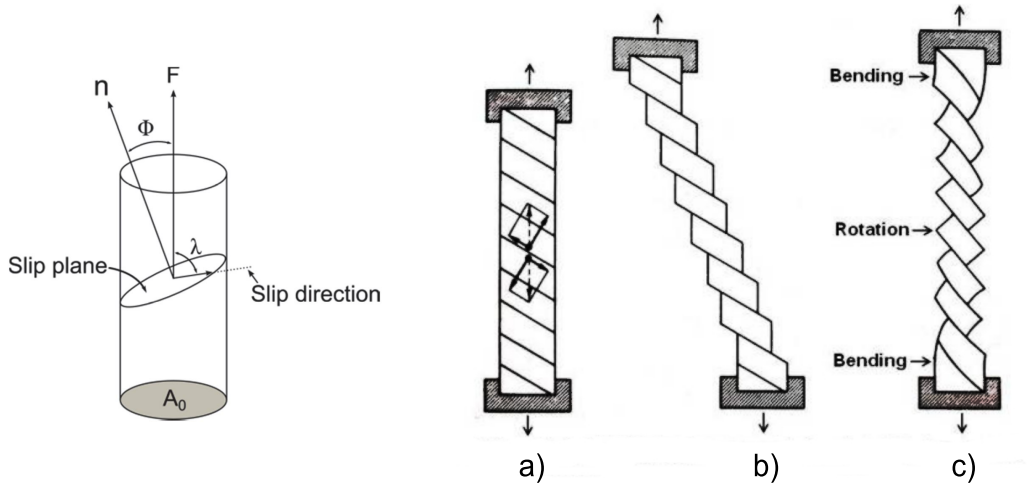

Figure 1.1: Left: Necessary parameters to calculate the critical resolved shear stress along a glide system [23], Right: Scheme of a specimen strained in tension, a) before the test, b) test with ends not constrained, c) test with constrained ends [40].

rotates towards the compression axis, resulting also in the changes in cross-section shape [40].

1.1.1 Microstructure and slip bands

As discussed above, during the deformation of single crystals, slip bands emerge along the surface of the crystal and the dislocation microstructure evolves constantly. Pure fcc single crystals oriented for single slip firstly deform with very few obstacles present in the crystal. Dislocations generated from Frank-Read sources can thus move long distances and escape at the surface, leaving behind them long and fine, uniformly distributed slip lines [41, 42].

With increasing strain, the dislocation activity on secondary systems increases and slip traces from these systems become visible [43]. Dislocations from primary system typically interact with dislocations on the secondary systems, giving rise to the formation of barriers hindering dislocation motion on all glide systems [44]. As the density of these barriers increases, the mean free path of gliding dislocations is reduced. Therefore, moving dislocations are more likely to pile up against these obstacles or tangle around them than to escape at the surface [23]. Consequently, the work hardening rate increases significantly, following the Taylor relationship:

$$\tau = \tau_0 + \alpha_T G b \sqrt{\rho_\mathrm{d}}, \tag{1.2}$$

where τ_0 is a constant representing the friction stress within the crystal, α_T is a correction factor between 0.4–1, G is the shear modulus, b is the Burgers vector and ρ_d is the density of dislocations. In this way, dislocation cell structures

typically develop, consisting of regions of high dislocation density (cell walls) and regions nearly free of dislocations (cell centers) [44, 45].

1.2 Mechanical behavior at the micro and sub-micrometre scale

It was shown by Taylor [46] as early as in 1924 that fine metallic wires exhibit higher strength than bulk specimens. This puzzling effect was later extensively investigated on metallic whiskers (long single crystals of high perfection) in the 1950's and 1960's (see e.g. [47–49]) and yield points close to the theoretical strength were even observed for the smallest diameters <5 µm. Such mechanical behavior was explained by the requirement for high stresses to activate dislocation sources in defect-free samples, while the stress needed for their continued operation was much lower [50].

Since the pioneering work of Uchic et al. in 2005 describing a methodology for the preparation of nickel single-crystalline micropillars by focused ion beam (FIB) and testing them in compression [8], many other research groups have used the same production method for various metals (having crystal structures also other than fcc), and size ranges [5–10]. All these studies reported that under compression the micropillars exhibit:

- a jerky plastic deformation consisting of stochastically discrete intermittent strain bursts (Fig. 1.2) separated by intervals of nearly elastic loading,
- increase in the metal flow stress when the pillar diameter is decreased below a few tens of micrometres.

FIB-milled micropillars are not defect-free and contain a high amount of dislocations. It was shown in [51] that the resolved shear stress τ normalized by the shear modulus G as a function of diameter d normalized by the magnitude of Burgers vector b follows a power-law:

$$\frac{\tau}{G} = c\left(\frac{d}{b}\right)^{m}, \tag{1.3}$$

where c is an empirical constant and m is the power-law exponent of the size effect. However, if the crystals are pristine (free of defects), the relation between strength and pillar diameter is different [23]. For example, in molybdenum solid solution micropillars prepared by selective etching, a resolved shear stress close to the theoretical strength was observed, regardless of the pillar diameter [17]. It was later confirmed by transmission electron microscopy [52] and white beam Laue

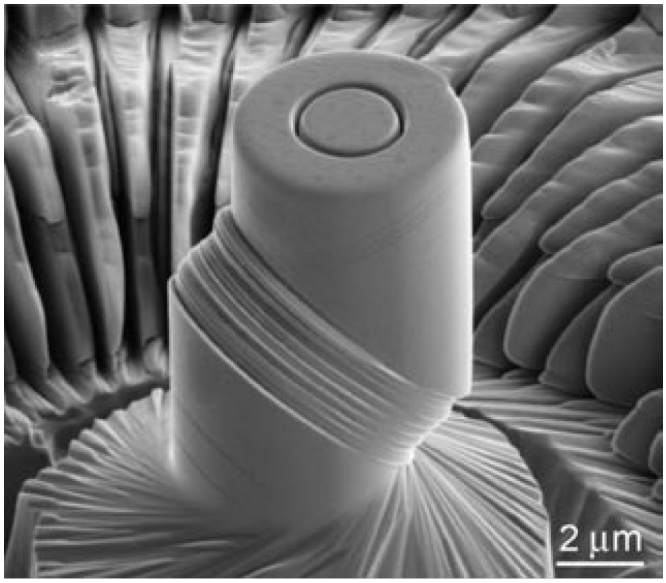

Figure 1.2: An SEM image of compressed 5 µm diameter micropillar sample of pure nickel oriented for single slip [55].

microdiffraction [53] that such micropillars were dislocation-free. This suggests that the high stress required for yield is associated with dislocation nucleation, as in the case of whiskers. Similar material was pre-strained to 4 % and 11 % prior to etching of micropillars [54]. The subsequent compression tests showed significantly lower resolved shear stresses, with values similar to those of pure molybdenum FIB-milled micropillars [11, 51].

Comparable pre-strain experiments were carried out also on non-pristine micropillars prepared by FIB milling, which is known to cause surface damage [56]. Results show that whereas pre-strained submicrospecimens exhibit a yield size effect similar to that without pre-straining, microspecimens show no size effect anymore [57, 58]. This suggests that at microscales, dislocation interactions by forest hardening dominate, whereas in the submicroregime a size dependent mechanisms govern the mechanical behavior [57, 59].

1.2.1 Theories for the size effect

Many theories involve surface-related effects since the surface to volume ratio increases as the sample size decreases. It was proposed in [60] that mobile dislocations escape at the free surface, where they are attracted due to image forces. As a result, the dislocation density decreases with strain and higher stresses are needed for activation of less favorable dislocation sources [23].

Greer and Nix [24, 61] suggested that under stresses nano- (rather than micro-) scale specimens can reach a state of *"dislocation starvation"* since in small crys-

tals mobile dislocations are annihilated at free surfaces before being multiplied. Consequently, the crystals become starved of dislocations and significantly higher stresses are required for nucleation of new dislocations during the deformation.

Different mechanisms were proposed addressing primarily the size effect in micropillars [62–67], namely source truncation, exhaustion hardening, and weakest link theory. General premises of these models involve representing dislocation source operations in a discrete fashion, and then evaluating the effect of sample size on the source lengths, and therefore also on their operation strengths [15]. In more plain words, within (sub)micrometer samples, typical double-pinned Frank-Read sources are truncated by the free surface and become single-ended sources leading to smaller average source lengths. As a result, higher stresses are required for the activation of such sources. In addition, once the longest source is activated, typical forest hardening may occur causing the shutdown of activated sources and higher stress is required to activate the second longest source [23].

The activation of abovementioned mechanisms is also dependent on the initial dislocation density. Considering the initial dislocation density in the range from 10^{12} to $10^{13}\mathrm{m}^{-2}$, Kiener [68] classified the size dependency of the plastic response into three domains:

1. Nanometer regime ($\leq$100 nm), where the deformation is typically carried by partial dislocations. Samples (e.g. whiskers) often contain no dislocation sources and thus exhibit strength values close to the theoretical strength required for the homogeneous nucleation of dislocations in a uniformly stressed crystal.

2. Intermediate regime (between 0.1 and 1 µm), where the strength depends on the statistics of activating only a few dislocation sources. Dislocation networks are not formed in this regime and deformation is carried by individual dislocations. Escape of a dislocation through the surface before it can multiply is very likely and higher stresses are needed to activate new dislocation sources.

3. Micrometer regime (above 1 µm), where dislocation interactions and networks govern the plastic response in a bulk-like manner [63]. However, if the distance between dislocations approaches the same scale as the specimen size ($\sim$1 µm for dislocation density of 10^{12} m^{-2}), the plastic deformation starts to be carried by individual dislocations and depends on the distribution of dislocation sources. The plasticity then transforms itself into the abovementioned intermediate regime and becomes source-controlled.

1.3 Microcellular metallic materials

Light cellular materials are rather ubiquitous in nature. Typical examples are bones, wood, cork, corals,... In the past decades, man-made materials having a relatively high volume fraction of void space (or in other words, a low relative density) have drawn attention and many research groups have focused on their development and characterization, inspired by lightweight cellular structures found in nature. Artificial cellular materials include polymers, ceramics, and metals, and among them, microcellular metals, (often simply called "metal foams"), are very attractive because they combine features, both structural and functional, that make them uniquely suited for certain applications [69]. Physical and mechanical properties offered by porous metals cannot be obtained with dense metals, or either dense or porous polymers and ceramics [70]. Typical applications of porous metals are lightweight structures, mechanical damping, vibration control, acoustic absorption, energy absorbers, packaging, heat exchangers, biocompatible inserts, and filters [70, 71]. Further specific examples can be found in e.g. [72, 73].

1.3.1 Structure of microcellular metallic materials

To describe the microstructure of low-density materials, the following definition is commonly used: A cellular solid is an assembly of cells with solid edges and (if present) solid faces, which are packed together to fill space [69]. If the porosity constitutes an interconnected network, i.e. the solid material is contained in the cell edges only and the cells connect through open faces, the material is called open-celled ("sponge-like"). On the other hand, if the faces within the structure are also solid, the foam is termed close-celled (see also Fig. 1.3). The term mesostructure designates the foam microstructure on the scale of several cells, i.e., the architecture of solid matter making the foam. This additional element of structure, namely the scale and shape of the pores, is a key determinant of the properties it will display [72]. It is possible to picture the porous metal as being more like an arrangement of thin, regular strut-like elements, rather than isolated pores. Then the most important parameters are not those of the pores, but those relating to the struts, such as the strut length (the distance between contact points or nodes) the strut diameter and the cross-sectional shape, thus reminding of the essential parameters of micropillars and other microsamples. Porous metals are often stochastic structures and are therefore subject to statistical variations in parameters associated with their structure. Provided samples are sufficiently large, these variations are smoothed out in the measurements and calculations to give average values [72].

Most metallic foams already available on the market are closed-cell. They are advantageous for structural performance, however, they cannot be used for

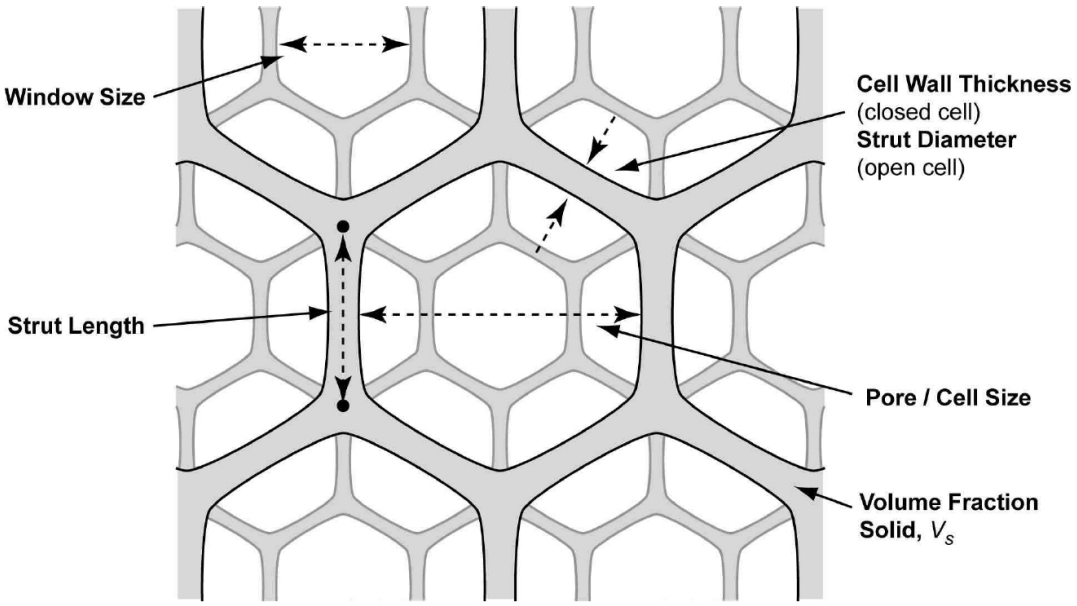

Figure 1.3: Schematic diagram of different structural features in the mesostructure of metal foams [72].

applications that require a fluid flow through the material (filters, catalysers, or heat exchangers). There are also some limitations due to the processing routes, as their structure generally features inhomogeneities in the density and cell size, a limited range of density and cell size achievable, and only a limited choice of the constitutive material is offered. Commercial open-pore cellular metals can, on the other hand, feature regular and reproducible structures. The processes by which they are produced are rather intricate [69]. One of such techniques, called salt-replication, was utilized in this work for the production of open-pore metal foams.

1.3.2 Production techniques

Metal foams can be produced using a very wide range of processing technologies and processes, which have been reviewed in e.g. [71–80]. The state of the metal (solid, liquid, gas or vapor) during the pore-creation process is the most common criterion to classify the diverse production methods. Another possibility is to categorize the metal foams according to the topology of the porosity (so-called mesostructure or "architecture"). The advantage of this approach is that the products fall into six natural families of porous metal, which generally share many characteristics and properties (details in [72]):

1. Isolated porosity – the pores are diluted and isolated in the solid metal; the pores are formed e.g. due to the Kirkendall effect [81] or chemical reactions of noble metals containing oxygen at elevated temperatures [82].

2. "True metal foam" – tightly packed gas bubbles which are separated by thin metal membranes.

3. Foam precursor – pre-existing polymer foam is used to create the structure of the metal foam (e.g. investment casting or metal deposition on polymer foam).

4. Porosity created by packing – assembly of individual elements leaving open spaces between them.

5. Porosity created by phase change - phase transition takes place in which single phase transforms into multiple phases one of which is gas that creates the porous structure (solidification with gas evolution, dealloying, ...).

6. Regular lattices – typically composed of regular beam elements; periodic metallic structures in contrast to five abovementioned classes, which are stochastic in nature.

As mentioned above, salt-replicated foams are of interest in this thesis. This type of cellular metals belongs to the fourth group, where porosity is created by packing and only this production route will be elaborated in this work in more detail. Porosity created by packing can be prepared by partial densification of packed metal elements in a form of powders, fibers or more complicated structures (e.g. hollow spheres). In order to create a solid contact between these elements, sintering is typically employed. On the other hand, the final foamed material from this group can be created in an "inverse manner", called the *replication processing*. This term is used to designate processes by which a liquid metal infiltrates open pores in a highly porous solid pattern (also called preform or space holder) prepared by packing of sodium chloride or other particles. Sodium chloride has numerous advantages: it is non-toxic, cheap and readily available in high amounts. Furthermore, after the processing, it can be easily leached in water [72]. The salt-replication technique used to prepare metal foams investigated in this thesis will be described later in detail.

1.3.3 Size effect in plastic deformation of microcellular metallic materials

Pore size effect

The ratio between the pore size and the width of uniaxial specimens manifests itself above a certain value, at which the deformation or fracture of edge or boundary pores contributes significantly to the overall sample response. In other words, the struts at the foam surface are unconnected at one end and therefore essentially unloaded. This, in turn, makes plastic deformation of porous structures scale-dependent [72, 83–85]. Test samples must, therefore, have a width that exceeds

a certain number of cell diameters in all dimensions for data to be characteristic of bulk material deformation [84, 86]. To obtain meaningful results, samples of microcellular material should be at least 20 cells across in all directions [72].

Plasticity size effect

The intrinsic size of the pores can affect the plastic stresses of porous metals, also for test samples much larger than the pores. This occurs when the size of pores or struts within metal becomes comparable with that of substructural features governing the plastic deformation of metals (e.g. mean dislocation separation distance or subgrain size). When the pore or strut diameter falls below a few micrometers, free surfaces start interfering with dislocation glide and this, in turn, alters the local in-situ flow stress of the metal within the porous material.

This effect is in metallurgy generally known as the crystal plasticity size effect. In microcellular metals, the effect closely resembles that found in testing small-scale specimens, such as micropillars produced by FIB milling [13, 88]. Measurements of the pore-size dependent flow stress of highly porous metals containing fine-scale structures are thus very interesting, not only *per se*, but also for the information they provide on the deformation of small metallic structures more generally. Such micropieces are already found in microelectromechanical systems (MEMS) and other microsystems. The investigations of metal foams are very attractive because such microscopic effects can be readily examined by conventional methods used for bulk samples instead of rather challenging experiments on microspecimens. Studies of the plasticity size effect in fine (µm-scale) replicated open-pore microcellular metals typically show a significant increase in

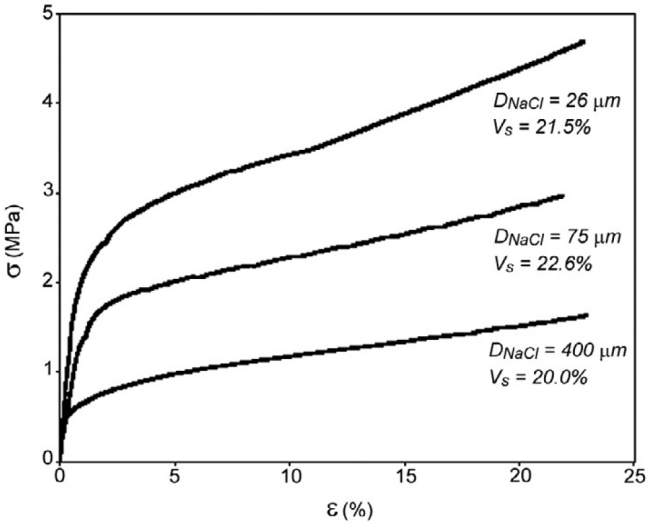

Figure 1.4: Example compressive stress–strain curves obtained for replicated aluminium foams of different mean pore size but similar density [87].

the flow stress with decreasing pore size below roughly 100 µm [87, 89–91].

Porous metals with nanometric pores one to two orders of magnitude finer compared with replicated metal foam can be produced by selective dissolution of a two-phase alloy or by dealloying. When the pore size falls roughly below ten nanometers, a different size-effect is evidenced. At the very high internal surface to volume ratio characteristic of nanoporous metals, surface stresses may contribute considerably to the internal stress equilibrium within the solid. In other words, a significant proportion of atoms in the solid is situated along pore surfaces and are thus differently bonded [72]. The size effects on flow stress in these materials can be enormous (although more challenging to measure). It is well documented that in nanoporous metals the in-situ metal flow stress increases with decreasing strut size, and can reach values (given the very small strut sizes that can be attained by dealloying) approaching the theoretical shear strength, to the point where occasionally the nanoporous metal is harder than the same metal in bulk form [92–95].

2. Acoustic emission

Acoustic emission (AE) are transient elastic waves generated in materials due to sudden localized and irreversible structure changes [96]. The AE technique belongs to non-destructive techniques (NDT), as it is capable of detecting structural changes within the material without destruction of tested part. Unlike in other NDT techniques (e.g. ultrasonic [97]), the AE technique is passive: the detected energy is released within the test object rather than being supplied by the testing method. Moreover, AE detects movement while most methods detect existing geometrical discontinuities [98].

Main advantages of the AE technique are:

- the technique does not require a careful preparation of the test sample surfaces as is required for scanning NDT techniques;
- it provides the detection and registration of growing defects that allows defining the degree of the damage in the test sample, related e.g. to its mechanical strength;
- it allows tracking of various processes and real-time evaluation of object condition.

The detection of AE is based on its physical nature. When the material is subjected to external force, a released energy in the AE source forms the stress pulse propagating through the material as transient elastic waves. At the surface of the material, it is transformed into a certain wave mode which corresponds to the geometrical configuration and the dimensions of the specimen. In other words, the material breakdown produces AE, which travels outward from the source, echoing through the body until it arrives at the sensor. The wave component perpendicular to the surface is detected e.g. by a piezoelectric transducer attached to the specimen surface, either directly or using a waveguide. The sensor converts displacements into an electrical signal which is transmitted to the AE measuring system and further processed (see Fig. 2.1) [99].

The AE equipment typically consists of the sensor (transducer), preamplifier, amplifier, A/D converter, signal analyzer and computer with special software. The scheme is presented in Fig. 2.2.

2.1 Microscopic origin of acoustic emission

There are three main dislocation processes which can produce AE during mechanical loading of metals [96]:

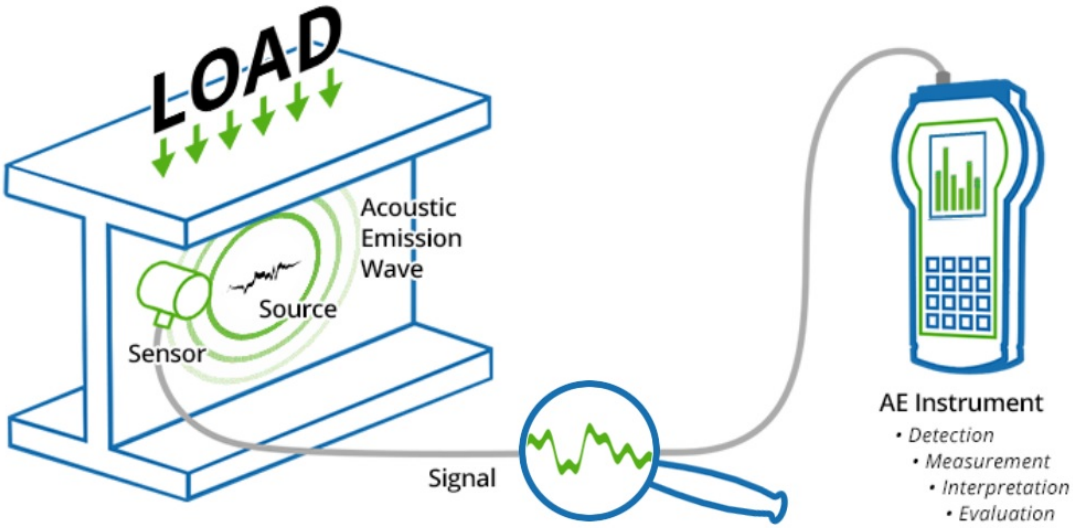

Figure 2.1: Scheme of the AE acquisition process [100].

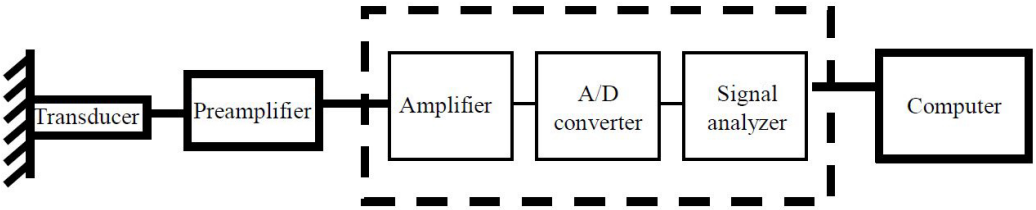

Figure 2.2: Diagram showing the typical AE equipment [99].

- Relaxation of stress fields caused by the passage of dislocations;
- Annihilation of dislocation - disappearance of stress fields of annihilated dislocations causes AE [101];
- "Bremsstrahlung" - acoustic radiation of accelerated (decelerated) dislocations, analogical to the electromagnetic radiation of a charged particle [96].

The energy released due to the annihilation of dislocation and Bremsstrahlung is 2-3 orders lower than that released due to dislocation slip.

The AE is detected as a displacement of the material surface Δy. Scruby et. al [102] studied the growth of a dislocation loop in an isotropic material and calculated the maximum displacement Δy produced by the longitudinal wave arrival at the epicenter (a location on the surface where the front of the moving wave reaches the surface of the material). The maximum surface displacement Δy for a simple case of AE generated by the growth of n dislocation loops in an

isotropic material can be derived:

$$\Delta y = \frac{nbrvc_T^2}{Dc_L^3} \tag{2.1}$$

where b is the Burgers vector, c_L and c_T are longitudinal and transversal wave velocities, r is the final radius of loop, v is the velocity of loop growth, and D is the depth of loop below the surface. A displacement which can be detected by a piezoelectric transducer is of the order of 10^{-13} m. Movement of a single dislocation typically produces the displacement of 10^{-15} m, which is not detectable [103]. Therefore, a passage of a single dislocation under common experimental conditions, or annihilation of a single dislocation pair, can hardly be expected to produce detectable AE signals. Yet, AE is detected during plastic deformation of metals and alloys, thus giving evidence that the processes of plastic deformation are characterized by cooperative dislocation dynamics. The most familiar example of AE generated during plastic deformation is that of the so-called "tin cry". Plastic deformation of tin crystals produces a clearly audible emission which is due to twinning within the tin crystal [104]. An interesting analogy can be made to the AE phenomenon by comparing it to earthquakes, which can be regarded as largest natural occurring AE sources. Earthquakes release seismic waves which are elastic waves that propagate through the Earth's crust and are detected by means of a network of seismometers located around the world [105].

The regular application of the AE technique as an in situ investigation method has started with a comprehensive study by Kaiser [106]. In particular, simple estimations show that a measurable stress drop of a few hundredth of MPa requires cooperative motion of the order of 10^5 dislocations through the sample cross-section, whereas, as mentioned above, the motion of a few hundred dislocations can provoke a measurable acoustic event [107]. Indeed, significant AE accompanies even macroscopically smooth deformation curves of pure materials [108]. Consequently, this technique is particularly useful for the study of the mechanisms of plastic deformation and failure in wide time and space ranges [96, 109, 110].

2.2 AE data analysis approaches

Two broad approaches can be employed for analysis of recorded AE data: traditionally used *parameter-based approach* and modern *waveform-based approach*.

2.2.1 Parameter-based analysis

In parameter based approach, signal parameters are used to assess the signal characteristics. Since the data streaming leads to huge data files (many gigabytes), this standard procedure is used in most of AE applications to extract significant acoustic events in real time, without recording the continuous signal itself. A typical AE signal along with commonly used parameters is shown in Fig. 2.3.

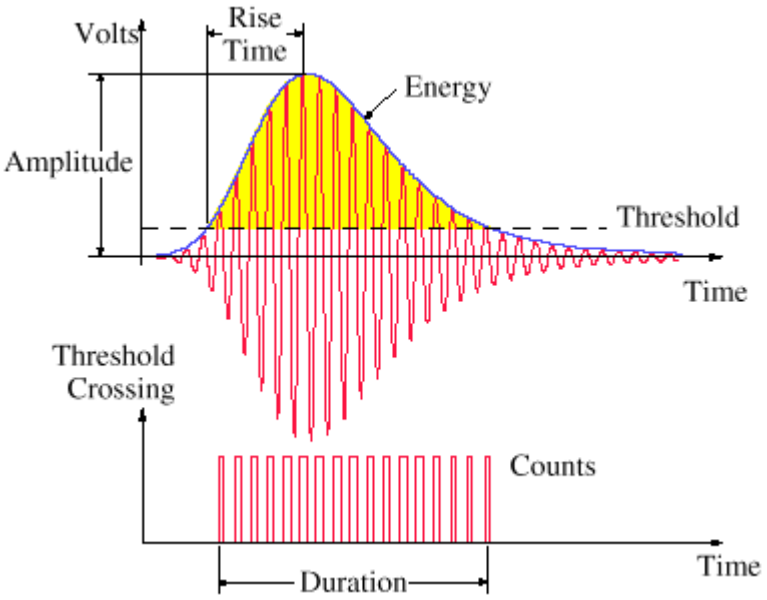

Figure 2.3: Parameter-based processing of the AE signal [111].

- *Threshold.* Recording is triggered once the output signals reach a set threshold value. This value is set to remove as much noise as possible, but care should be taken so that weak signals are not missed by setting too high threshold.
- *AE event.* A signal that exceeds the threshold and causes a system channel to accumulate data.
- *Amplitude.* Peak voltage of the signal waveform (representing the AE event) is closely related to the magnitude of the source event. The amplitude of the signals is expressed in volts or in AE decibel scale, where 1 µV at the sensor is defined as 0 dB. Preamplifier gain (in dB): $\mathrm{dB_{AE}} = 20 \log (\mathrm{V_{max}}/1\ \mu\mathrm{V})$.
- *Rise time.* The interval between the time when the signal is triggered and the time the signal reaches the maximum amplitude.
- *Duration.* The interval between the time when the signal is triggered and the time the signal decreases below the threshold value.

- *Energy.* Various ways of expressing energy exist (area under the amplitude curve is one of the most common).
- *Counts.* The number of times a signal crosses the threshold within the event duration.

Two basic types of the AE signal may be distinguished (Fig. 2.4). *Continuous emission* has an erratic character and is typically characterized by low energy waves produced simultaneously by a large number of sources. Dislocation motion, i.e. the activity of Frank-Read sources and piling up of dislocations at obstacles, dislocation annihilation, recrystallization and martensitic phase transformation can be the sources of continuous AE signal. *Burst (transient) emission* has an avalanche-like character. The emitted energy is higher (possibly by 10–14 orders of magnitude) than for continuous emission. Typical sources of burst AE are instabilities in plastic deformation (Portevin-Le Châtelier effect), twinning, crack nucleation and propagation.

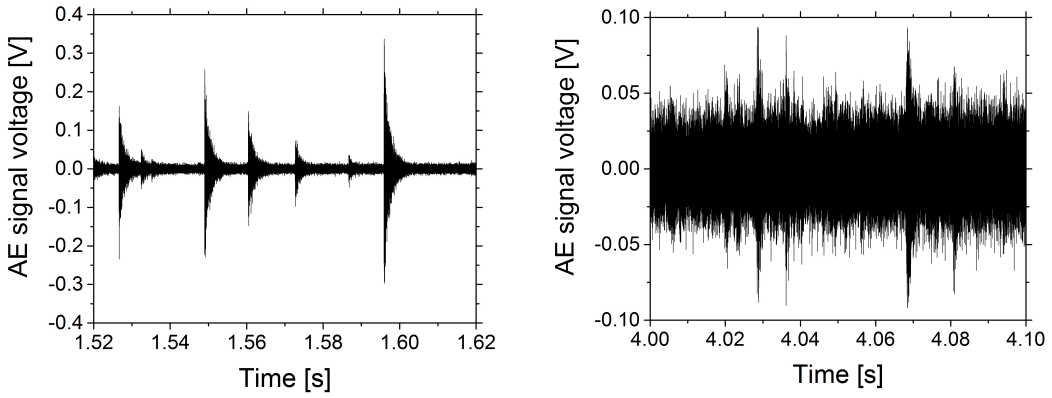

Figure 2.4: Two types of the AE signals: burst signals (left) and continuous signals (right).

2.2.2 Waveform-based analysis

It was shown in the previous section that in the parameter-based analysis only some of the parameters of the AE signal are recorded, but not the signal itself. This minimizes the amount of stored data and enables fast data recording. With the availability of better AE devices and higher computing resources, it is nowadays possible to perform quick data acquisition and record complete waveforms [105]. If the data streaming technique is used and the entire raw AE signal is stored, a signal parametrization described above can be performed any time later. This approach has an advantage that individualization parameters can be tuned and chosen based on inspection of the recorded signal. The parameters used for the individualization of AE events are shown in Fig. 2.5.

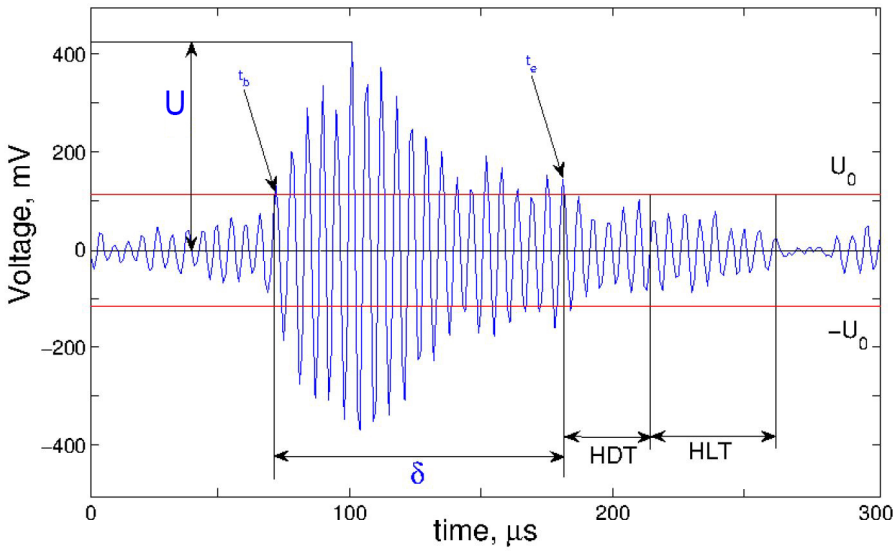

Figure 2.5: Parameters used for the individualization of AE events [109].

- *Threshold voltage* U_0. An event is considered to start when the signal surpasses U_0. This parameter is aimed at cutting off the part of the acoustic signal below the noise level.

- *Hit definition time, HDT.* The event is considered to have come to an end if the signal remains below U_0 longer than during HDT.

- *Hit lockout time, HLT* (also called *"dead time"*). After detecting the end of an event, no measurement is performed during HLT in order to filter out sound reflections. The HLT is triggered at the end of HDT. Consequently, the sum of HDT and HLT represents the minimum time between the end of one event and the start of the next one.

It is obvious that the choice of U_0, HDT, and HLT may influence on the identification of the AE events and, therefore, on the apparent statistical distributions of their characteristics. The conventional AE studies apply "rules of thumb" to set the appropriate time parameters.

In statistical investigations, the maximum amplitudes U of acoustic events are frequently examined. It was shown that there is a proportionality relationship between U and the strain increment caused by the dislocation avalanche: $U \sim \Delta\varepsilon$. Its feasibility is confirmed, e.g., by experiments on ice single crystals, which showed proportionality between the global AE activity and plastic deformation [112]. Weiss et al. [108] provide arguments that this relationship should be valid in a more general case, e.g., for a decay following a power-law, as expected in the case of avalanche-like behavior.

The waveform analysis approach offers better data interpretation capability by allowing also the use of numerous signal post-processing techniques. Frequency analysis of recorded signals is the most commonly used tool and is performed by means of Fourier transform or time-frequency analyses (e.g. short time Fourier transform and wavelet analysis). Such analyses can provide information about the nature of the AE sources and help in distinguishing among them [105].

Fourier transformation allows determining the frequency spectrum by decomposing the analyzed signal $f(t)$ into the sum of harmonic functions $\{e^{ikt}\}$:

$$f(t) = \sum_{k=-\infty}^{\infty} f_k e^{ikt}, \tag{2.2}$$

where f_k is the contribution of the frequency k, given by the following relationship:

$$f_k = \frac{1}{2\pi} \int_{-\pi}^{\pi} f(t) e^{-ikt} \mathrm{d}t. \tag{2.3}$$

However, fast Fourier transform (FFT) is usually applied in practice [113]. This analysis is particularly efficient when the analyzed signal is composed of several harmonics. Then, the output of the computation provides their frequency and intensities. The applications of FFT are, however, not limited to these cases. In fact, the Fourier transformation often provides important pieces of information on the nature of complex signals.

In addition to FFT analysis of the AE waveforms, the Fourier spectral analysis can be also applied to the continuously recorded signal in order to examine the evolution of the emitted energy and the characteristic frequency of the signal [114]. The data set can be divided into overlapping windows and the power spectral density function $P(f)$ of each subset is computed using FFT. Two characteristics can be particularly useful, namely the AE signal "energy" E

$$E = \int_{f_{min}}^{f_{max}} P(f) \mathrm{d}f \tag{2.4}$$

and the median frequency f_{med}:

$$\int_{0}^{f_{med}} P(f) \mathrm{d}f = \int_{f_{med}}^{\infty} P(f) \mathrm{d}f. \tag{2.5}$$

The variations in the average energy and median frequency reflect the variations in the degree of correlation in the motion of dislocations generating the AE [109, 114].

3. Microsamples: experimental procedure

3.1 Copper micropillars

Experiments on the copper micropillars were carried out in cooperation with the Department of Materials Physics, Eötvös Loránd University in Budapest (ELTE, Budapest).

Due to the statistical nature of micropillar deformation, a vast amount of samples is needed to obtain relevant data sets. The easiest and most conventional method for micropillar fabrication is the FIB milling [115]. The main advantage of this method is that the process of ion milling can be controlled visually. In order to shorten the fabrication time of micropillars, a number of growing (FIB-less) methods were developed [116, 117]. These, however, do not allow for the production of pillars from any type of material; and there is also a very limited control over the initial dislocation density in the sample. Moreover, the pillars produced by growing suffer from only a weak connection between the substrate and the microsample itself [118].

To fabricate micropillar specimens by the FIB milling, two approaches are commonly applied, namely *lathe* and *top-down* (or *annular*) milling [119]. Lathe milling uses an ion beam almost perpendicular to the axis of micropillar that is being produced. The substrate is slowly rotated, thus leaving behind a specimen of cylindrical shape. This procedure is usually carried out on one of the sides of a thin layer of substrate material. With the top-down technique, the pillar axis is parallel to the ion beam and the ion "etch" the surface of the material. In this case, however, the height and tapering of micropillars are poorly controlled. A new method outlined in this thesis combines the advantages of both presented fabrication techniques. Using this improved method, a non-tapered micropillar can be fabricated anywhere on the surface of a bulk material; furthermore, much shorter preparation times are required [120].

3.1.1 Sample preparation

In-situ micropillar deformation tests demand very careful and precise sample preparation. In order to obtain required surface properties, orientation, and initial dislocation density, the following steps were performed.

After a short etching, the copper substrate was electropolished in phosphoric

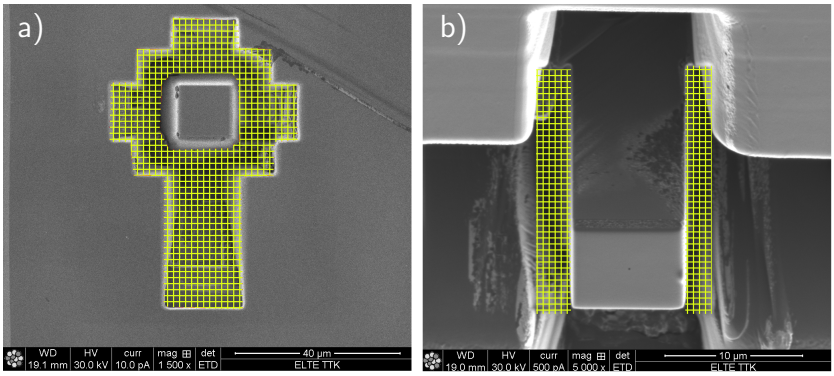

Figure 3.1: a) The initial FIB milling step marked by the grid to fabricate the "raw" pillar and the hole around it, that is necessary to allow for carrying out the compression test. At this milling step, 30 nA ion current is applied. b) The second milling step with 45° ion direction angle (see Fig. 2, too). The area removed by this step is marked by the grid. The ion current is 5 nA. Both pictures are taken from the ion direction. (Courtesy of P. D. Ispánovity, ELTE)

acid aqueous solution with 60 mA/mm^2 current density. The lattice orientation was measured using electron back-scattered diffraction (EBSD). The sample was cut by electric discharge machining to have a surface orientation [1 2 3]. After this step, another electropolishing was carried out and subsequently the sample was heat treated for 72 hours at 400 °C in vacuum. After the heat treatment, the surface was electropolished again with 30 mA/mm^2 current density and the orientation was checked again by EBSD.

After the surface preparation processes, a "surrounding hole" was milled around the intended pillar using 30 nA ion current. The FIB milling pattern is marked by the grid in Fig. 3.1a. The sample was oriented so that the normal vector of the surface was parallel to the ion beam direction. Then, a thin Pt layer was deposited onto the top surface of the micropillar. The Pt cap acts as a shield and thus helps to fabricate smooth and parallel surfaces on the pillar sides. This, in turn, eliminates effects related to the misalignment of the compressing tip (discussed below). To proceed to the next step, the stage is tilted by 7° (due to the 52° ion-electron beam angle, this results in a 45° angle of the ion beam with respect to the surface normal vector). In order to prevent inaccurate positioning of the microscope stage, a 2 µm cross was imprinted onto the geometric center of the top surface of the micropillar. Subsequently, the steps explained in Fig. 3.2 were performed. In order to further decrease tapering [121], a final, refining step was done with 30 pA ion beam overtilted by 1° with respect to the pillar axis.

Apart from the first step explained above, the fabrication is performed at high angles with respect to the substrate surface. This increases the effectiveness of

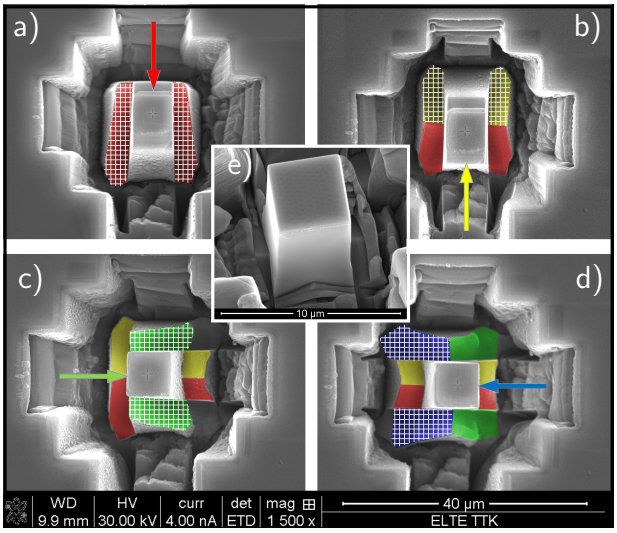

Figure 3.2: The details on the second, finalizing, step of the micropillar fabrication procedure with ion current of 5 nA. a) After the first step seen in Fig. 1 the sample is tilted by 45° resulting in a tilted ion beam direction. After this step, two rectangular FIB patterns (marked by the red grid) are used to obtain the surface marked by red. b) The sample is then rotated by 180°, and two rectangular FIB patterns are used again to obtain the surface marked by yellow. With a rotation by 90°, and repeating the two previous steps, the surfaces marked by green c) and blue d) are attained. In order to have a pillar with smooth surface and practically no tapering, the process is repeated with ion currents of 1 nA and 100 pA. The final rectangular pillar is shown in the inset e). (Courtesy of P. D. Ispánovity, ELTE)

milling by a factor of 2.5–3 compared with the perpendicular beam setup commonly used [122]. The 45° milling direction applied in the second phase also allows us to fabricate micropillars anywhere on the flat sample surface.

It should be mentioned that the Ga ion beam forms an irradiated layer on the micropillar surface. However, a slightly tilted final "polishing" step with significantly reduced ion beam current and acceleration voltage decreases the thickness of this layer to the negligible values, given the size of studied micropillars [123].

In summary, the most important advantages of the proposed milling procedure are:

- the micropillars can be fabricated at any position on the surface,
- the preparation is touchless, therefore any potential deformation of the pillar is avoided during the whole production process, and finally,
- the effects related to tapering and Ga implantation can be significantly diminished.

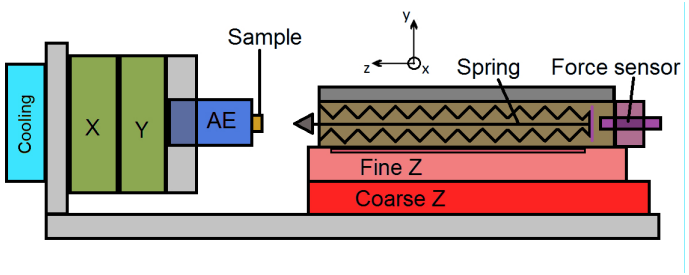

Figure 3.3: Scheme of the in-situ device NANOTEST. (Courtesy of A. Hegyi, ELTE)

3.1.2 In-situ device

In-situ micromechanical tests require the testing device to be placed inside the chamber of the scanning electron microscope (SEM). Such a device was developed at ELTE, Budapest, to be used in an FEI Quanta 3D SEM for the tests presented in this work. The sketch of the apparatus is shown in Fig. 3.3.

Two linear ultrasonic motors are used for the X and Y positioning of the sample. The AE transducer is mounted on the top of the two stages. In Z direction other two stages are used. One is a linear step-motor stage used for the raw motion of the compressing tip to bring it closer to the sample. The other one, mounted on the linear step-motor stage, is a piezoelectric positioning (PEP) stage with a resolution of 0.1 nm. During the actual compression test, only this "finer" stage is being moved. In order to measure the external force, a standard spring mounted on the PEP stage is used, with high transversal but very weak longitudinal stiffness. The elongation e of the spring is measured by a capacitive sensor with 0.1 nm resolution. If the PEP stage is moved by a distance x, and the capacitive sensor measures elongation e, then the sample deformation can be calculated as $x - e$. The acting force can be also determined $F = se$, where s is the stiffness of the spring. The pillar compression is performed using a flat punch diamond tip. It should be mentioned that to avoid charging of the compressing head in the SEM, a tip doped with boron is used. Due to the intermittent character of plastic deformation at small scales, it is also crucial to have a fast enough feedback controlling system. This is achieved by means of an analogic PID-type feedback electronics and a fast 16 bit AD converter. The range and the resolution parameters of the device are summarized in Tab. 3.1.

To achieve listed resolutions, the thermal and elastic elongation of device components must be negligible in the course of the test (typically several minutes). To this end, a number of improvements had to be done to the compression device. A foremost problem was how to reduce the heat produced by the motors of the stages. The Quanta 3D SEM has an environmental stage with a Peltier sample holder to set the sample temperature. The cold point of the Peltier

stage is mounted at the bottom of the device. In this manner, the temperature is stabilized at 15 °C. Another important issue that needed to be eliminated were vibrations of the force sensor spring which arise in the vacuum (due to a non-existent damping in the absence of air). To hamper this rather disturbing effect, strong permanent magnets were placed close to the lamellae of the force-measuring spring, thus providing the necessary damping due to the eddy currents.

Table 3.1: Parameters of the nanodeformation device

Part name	**Total range**	**Resolution**	**Accuracy**
X and Y	±8 mm	0.5 µm	0.01 µm
Z coarse	9 mm	2 µm	0.5 µm
Z fine	35 µm	1 nm	0.1 nm
Force sensor	20 or 50 mN	1 or 2.5 µN	1 or 2.5 µN

3.1.3 Acoustic emission measurement

The AE measuring system was approached to shed more light on the dynamic processes occurring during the plastic deformation of micropillars. In bulk materials, a direct correlation of the AE parameters with the stress-strain curves can reveal the activation of different deformation mechanisms [108, 124–126]. It is important to note again that the collective motion of at least several tens of dislocations is necessary in order to obtain a detectable AE signal [127]. Therefore, the AE signals reflect the cooperative character of dislocation motion. Intermittent strain bursts resulting from a collective dislocation activity observed during the compression of microsamples indicate that the AE technique has a great potential to provide information on these dynamic processes, even if those are invisible on the deformation curves. To the best knowledge of our research team, the study presented in this work is the first attempt to record the AE signals during the micropillar compression.

3.2 Aluminum microwires

The development of a net-shaped microspecimen casting process was done in the Laboratory of Mechanical Metallurgy, École polytechnique fédérale de Lausanne (EPFL, Lausanne), and was inspired by a process invented for the production of open cell aluminum foams by replication (described in Chapter 5) [23].

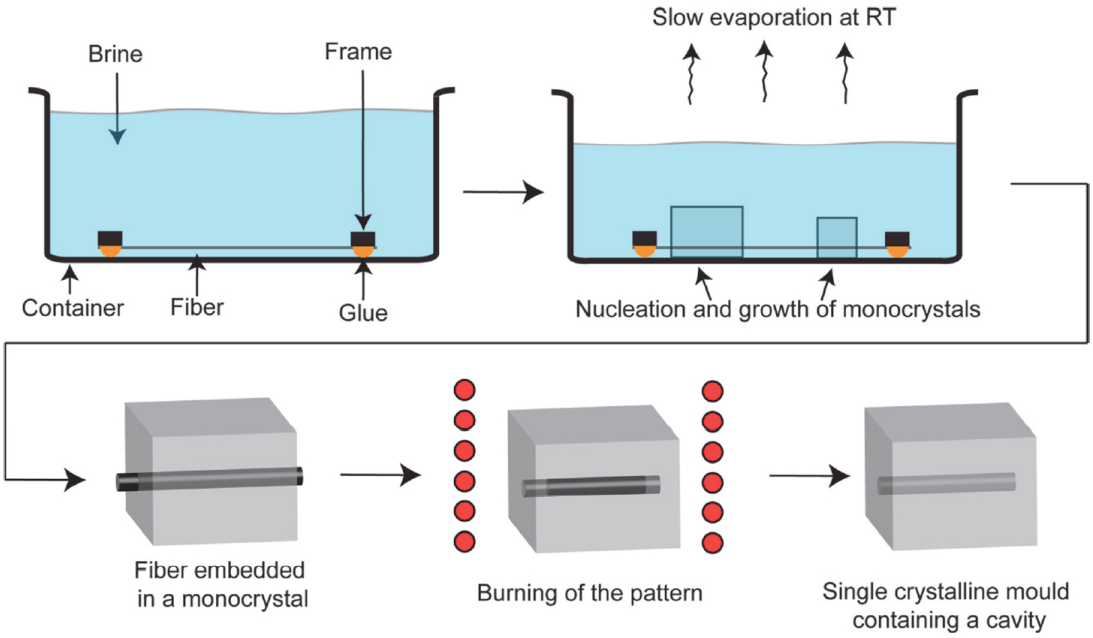

Figure 3.4: Overall process flow chart for the production of single-crystalline NaCl moulds [23].

3.2.1 Casting process

Moulds prepared by brine crystallization

The mould prepared by this method is composed of one large NaCl grain. The process consists of the following steps (shown also in Fig. 3.4) [23]:

1. Rapid pyrolysable fiber patterns were slightly stretched and individually glued on a PVC frame by an Araldite rapid glue. A slightly undersaturated salt solution was prepared, filtrated to remove all dust particles, placed on an anti-vibration container and covered with a hemispherical cover. Then the fiber-containing solution was left so that water could slowly evaporate.

2. Salt single crystals often nucleated on the stretched wires and intimately surrounded them (full crystallization can take up to 2 months).

3. The pyrolysis was carried out in two steps (temperature increased from RT to 250 °C; kept for 90 min; then increased to 600 °C and kept for 270 min). In this way, salt crystals traversed by a cylindrical cavity were prepared and used as casting moulds.

Infiltration

Infiltration of the hollow parts of the moulds by molten aluminum was accomplished using these steps:

1. After clearly ink-marking the entrance and the exit sides of the cavities, two or three moulds were placed into a graphite coated alumina crucible. Small NaCl grains were poured around the moulds in order to hold them in the crucible with their opened faces horizontally oriented. Above the small grains, coarse salt particles were added to break and filter off the aluminum oxide layer of the molten ingot during infiltration.

2. Finally, a 99.99 % aluminum bar was placed on the top.

3. The chamber containing the crucibles was sealed and placed under vacuum (0.5 mbar) and then slowly brought down into a furnace pre-heated at 710 °C.

4. After ∼45 min, 1.5 MPa of 4N argon gas were applied to push the molten aluminum into the microcavities of the moulds. Upon 3 min waiting time, the chamber was taken out and placed on a copper chill to promote directional solidification.

5. Once cooled, the ingots were removed from the crucibles. The salt moulds were removed from their ingots and cleaned.

Mould leaching

The microcastings were released by leaching the salt moulds in water containing a corrosion inhibitor, namely distilled water containing 0.84 g/l of $NaHCO_3$ and 1.62 g/l of Na_2CrO_4, corresponding to 0.01 mol concentrations of both substances [128].

The wire was then attached to a holder serving as one of tensile machine grip. The aluminum grip had been previously cleaned with ethanol in an ultrasonic bath. The wire was carefully positioned and glued with a drop of low viscosity cyanoacrylate glue. For wires with a diameter larger than 100 µm, a glue sensitive to ultraviolet light is used for the repeated gluing.

3.2.2 Tensile machine

A custom-built tensile testing apparatus was constructed at EPFL, Lausanne, in order to test metallic microwires produced using the abovedescribed method. The machine is displacement controlled and can be used for both tensile and compression testing. The set-up lies on a table placed on a large anti-vibration air-bedded marble block and is composed of three main parts: a binocular microscope, a moving stage, and a load cell (Fig. 3.5).

The force cell and the moving stage are both attached on a rigid block of steel. The moving stage is controlled by a Maxon DC motor (max. 7250 rotation/min)

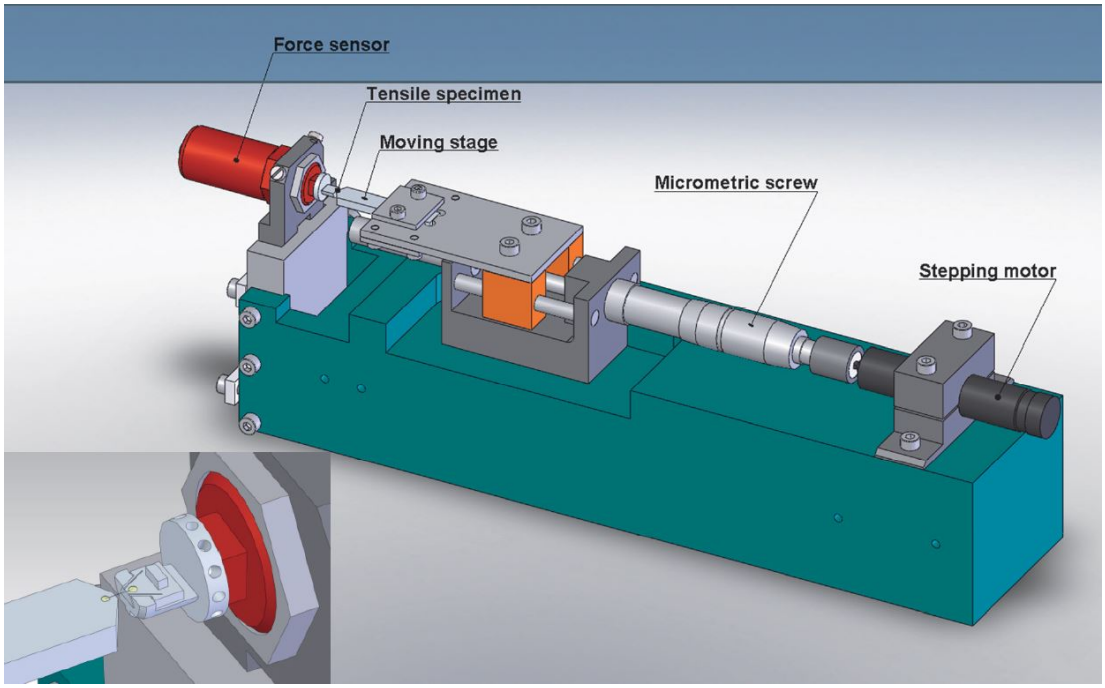

Figure 3.5: Schematic illustration of the tensile stage. On the right part, the motor rotates a micrometric screw, which in turn displaces linearly the stage. Opposite to the moving stage is the load cell on which a grip can be placed. One extremity of the sample is attached on this grip and the other glued on the moving stage prior to testing (see the inset) [23].

associated with a reduction gear and a micrometric screw transforming the motor motion into a linear displacement. The motor motion is continuously controlled with a precision of 10 nm. The linear displacement rate of the moving stage can be preset between 50 and 4000 nm/s (300 nm/s for the tests presented in this work), and the maximum displacement is 20 mm. A calibrated Futek LPM200 load cell with a nominal force of 500 mN was used to measure the applied load on wires. The resolution is 0.3 % of the nominal force. To control the tensile machine and record the data a LabView program was also developed at EPFL.

3.2.3 Acoustic emission measurement

In order to be able to record the AE response of tested microwires, to prevent microwire damage before the test, and to ensure optimal contact with the AE transducer, the following testing procedure was developed. First, the AE transducer was electrically insulated using a PTFE (Teflon) tape. A "tab" made of aluminum foil was glued to one end of the microwire. Prior to the testing, the tab side of the microwire was placed on the AE transducer with the help of a small amount of vacuum grease and glued down using a glue curable by ultraviolet light. Then, the other extremity of the microwire was glued (using again the UV

glue) directly to the load cell. The acoustic contact was verified before each test by scratching the end of the microwire carefully with a needle. A more common pencil lead break (Hsu-Nielsen source) test could not be carried out as it would pre-deform the microwire.

3.3 Parameters of AE measurements

As described in the preceding sections, experimental methods and devices were developed for the fabrication and testing of two types of microsamples (copper micropillars - tested in compression, and aluminum microwires - tested in tension) facilitating also a concurrent recording of the AE signal. After numerous unsuccessful attempts to employ the streaming AE device, it turned out that the parameter-based DAKEL-XEDO-3 computer controlled AE system (from DAKEL-ZD RPETY company) was the most sensitive device to be used for such fine experiments on the samples having very small volumes. In this way, sets of AE parameters involving counts, amplitudes and durations were recorded. By extensive tuning of the measurement parameters and testing different components, we ended up with the following, most sensitive setup. The gain of the device was set to 26 dB. A switch selectable gain preamplifier set to the signal gain of 60 dB and piezoelectric transducers (both from Physical Acoustic Corporation) were used.

A rectangular piece of material (with micropillar samples fabricated onto its surface) was attached directly to the AE transducer using a metallic spring. In addition, the acoustic contact was improved by means of a vacuum grease. In the case of aluminum microwires, the specimens were glued directly to the transducer, as described in detail in the previous section. The threshold level for the AE events individualization was always set only slightly above the noise level to ensure recording of as much AE data as possible. Except for the first set of data from the micropillars, a minimum event duration was set to zero. This modification allowed for collecting of even very short events and increased the number of registered events, what in turn made possible to perform the statistical evaluation.

3.3.1 Data treatment

Deformation and AE data recorded simultaneously during the compression of copper micropillars or tensile tests on aluminum microwires were processed using mostly home-written Matlab scripts (most important codes are shown in the Attachments). The time-force signal was recorded at a sampling rate of 50 Hz and 200 Hz for the tests on microwires and micropillars, respectively, to provide a sufficient resolution for the investigation of the intermittent character of defor-

mation curves. In order to obtain a workable signal, the raw data were filtered. A moving average filter of 10 points (simple averaging of 10 previous points in the signal) was used so that the random noise was removed while the sharp steps in the signal were retained. The AE count rates (number of counts per second) were evaluated to reveal the AE activity at particular stages of deformation. In order to be able to find precise correlations between the AE signal and the deformation curves, the AE events and their parameters (namely amplitude, duration, and counts per event) were also analyzed.

First, all load drops were extracted based on a relative change of the difference between two consecutive points. A minimum absolute drop size was set to 0.001 MPa, a maximum drop size was 0.1 MPa in order to filter out rare, atypical events. The AE events were also filtered in a way where the events consisting of less than two AE counts were ruled out. This step ensures that "small" events (which can be real signals, but also might be due to the closeness of the threshold level to the noise level) are not included in the statistics. In the next step, the AE events that are being very close to one another ($\pm$ 0.1 s) were merged together as there is a good chance that such events correspond to a single large stress drop. The algorithm then searches through the load drops and finds those having a time stamp (a precise time when the drop takes place) equal to the time stamp of a particular event within a short time interval of 0.3 s. Finally, the load drop sizes and corresponding AE event parameters were "binned" into bins such that: i) the minimum bin size is 0.005 MPa, ii) the minimum number of events in the bin is 5, iii) the histogram is normalized by a number of members in individual bins.

4. Microsamples: experimental results

First results from the abovedescribed newly developed testing methods combining the mechanical testing of microsamples with the AE measurement are presented in this chapter.

4.1 Copper micropillars

The experiments consisted of *in-situ* compression tests performed in the SEM with a concurrent recording of the AE data, as was described in the previous sections. Two different sets of micropillars were subjected to the testing:

1. Single-crystalline copper substrate predeformed to the flow stress of 20 MPa. The geometry of fabricated pillars was 5 µm in side length and 10 µm in height; the aspect ratio was thus 1:2 and 8 samples were tested.

2. Single-crystalline copper substrate predeformed to the flow stress of 10 MPa. The aspect ratio was 1:3 and three different geometries of micropillars were prepared:

   - side length of 2 µm, height of 6 µm (9 samples),
   - side length of 4 µm, height of 12 µm (4 samples),
   - side length of 8 µm, height of 24 µm (4 samples).

The orientation of the bulk single-crystalline copper onto which the micropillars were fabricated was very close to [123], which is the orientation favorable for the single slip. Identical orientation of all tested samples allowed for a direct comparison of the recorded stress-strain curves.

4.1.1 Results and discussion

Compression tests performed on micropillars from the first group are shown in Fig. 4.1. It is witnessed that the statistical variations in the flow stresses of individual samples are relatively high. There is quite large difference in the yield strength and flow stresses among the samples, which is most likely due to typical dislocation cells formed upon pre-straining of the substrate, resulting, in turn, in varying dislocation density from sample to sample.

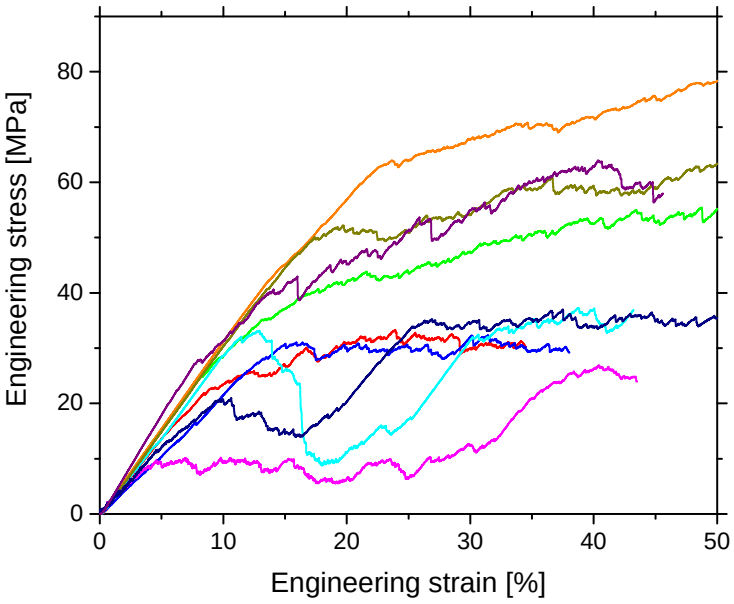

Figure 4.1: Compression curves of all tested copper micropillars from the first set.

Deformation curves together with the AE response of all the micropillars from this set are shown in Fig. 4.2a-h. It can be observed that there is a clear trend manifesting that the AE is more intensive in the pillars which exhibit low hardening, i.e. are "softer". Moreover, the AE response also varies in the course of individual compression tests, following very similar pattern: hardening stages of deformation are accompanied by very scarce AE signals, whereas the stages rich in large stress drops (i.e. where the reduction in the flow stress takes place) exhibit a distinctive AE activity. This is best visible in Fig. 4.2d,e,h. In Fig. 4.3 the compression curve of the micropillar from Fig. 4.2h was divided into four naturally occurring stages observed during this test; cumulative AE counts are also shown for a better demonstration. AE is almost absent throughout the elastic deformation in the stage I (such a characteristic is present in all the samples since the collective dislocation movement is not expected in the elastic region). As the compression proceeds further, the mechanical "softening" observed in Stage II is abundant in AE. The following hardening (stage III) is, in terms of AE, practically silent, and the plateau-like deformation in stage IV is accompanied by the AE signals again. It is worth noting that the trends observed in the cumulative counts curve are almost a mirror picture of the trends seen in the compression curve, thereby strongly indicating a relation between these two quantities.

One more micropillar sample from this set was tested using refined AE recording settings. The lower limit for an event duration was set to zero, and thus even very short events expected to occur during such fine tests are collected. Working with the AE events in comparison with the AE count rate has an advantage in

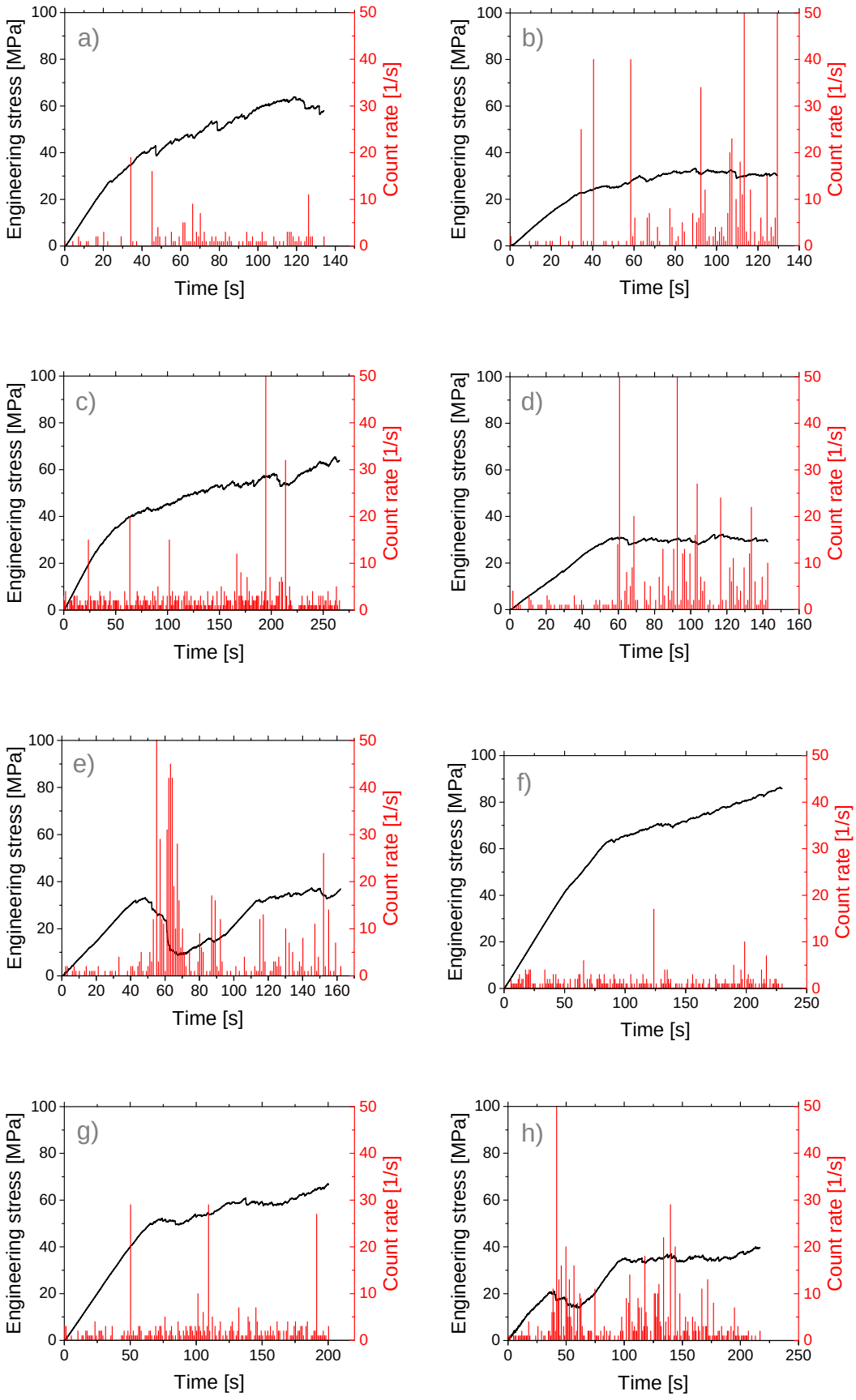

Figure 4.2: Compression curves and the AE response of copper micropillars from the first set.

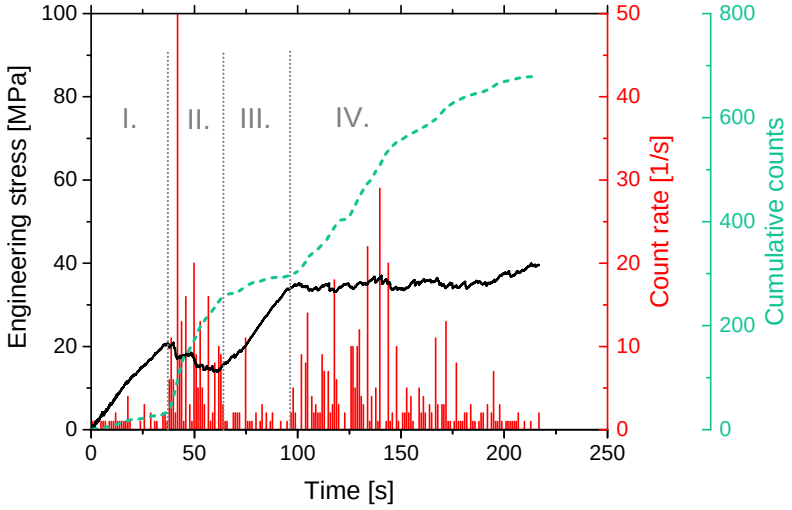

Figure 4.3: Typical AE response corresponding to different (hardening and softening) stages of micropillar compression.

precise time stamps recorded for particular AE events rather than an average value of counts per second, therefore allowing for evaluation of correlations between the stress drops and the AE event parameters. The results of this test are shown in Fig. 4.4. The AE-rich stage at the end of the test, reflecting a mechanical softening in the sample, confirms that the abovementioned results hold also when the AE events are of concern.

Upon zooming in to this region (see Fig. 4.5 and 4.6), an evident link is found between the load drops and the occurrence of AE events. Three parameters of AE events are plotted: counts per event, event durations, and event amplitudes. A couple of remarks calling for further attention can be made:

- Time-correlations between the drops and the AE events are very precise: the AE occurs exactly when the load drops take place.
- Not all stress drops are accompanied by the AE event, whereas the occurrence of AE is almost certainly linked to a stress drop.
- Stress drop size is not necessarily proportional to the magnitude of AE event parameters. For example, in Fig. 4.5 three successive drops are marked, decreasing in size from drop 1 to drop 3. The first (largest) drop produced only a weak AE; the second drop produced a relatively strong AE event; while the last drop did not lead to any AE signal.
- A fine structure of the stress drop can be caught by the AE technique, as shown in Fig. 4.6 demonstrating a detailed arrangement of the drop, where also minor steps making the large drop produce detectable AE.

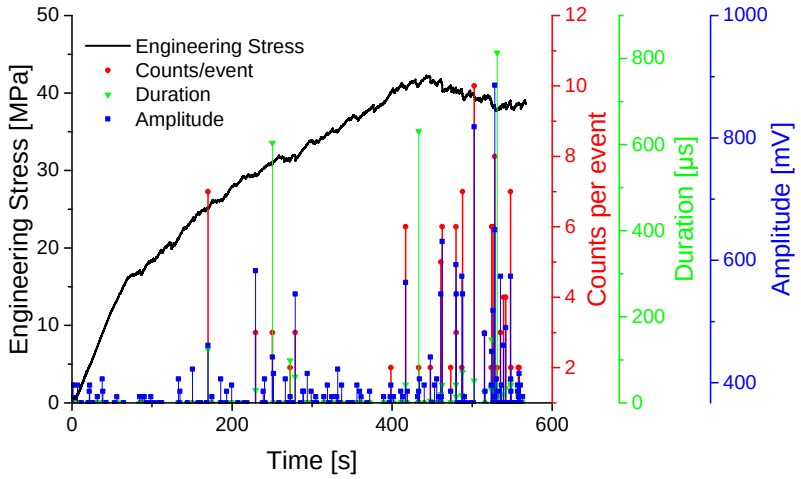

Figure 4.4: Compression test on a copper micropillar with precise simultaneous recording of the AE events and their parameters.

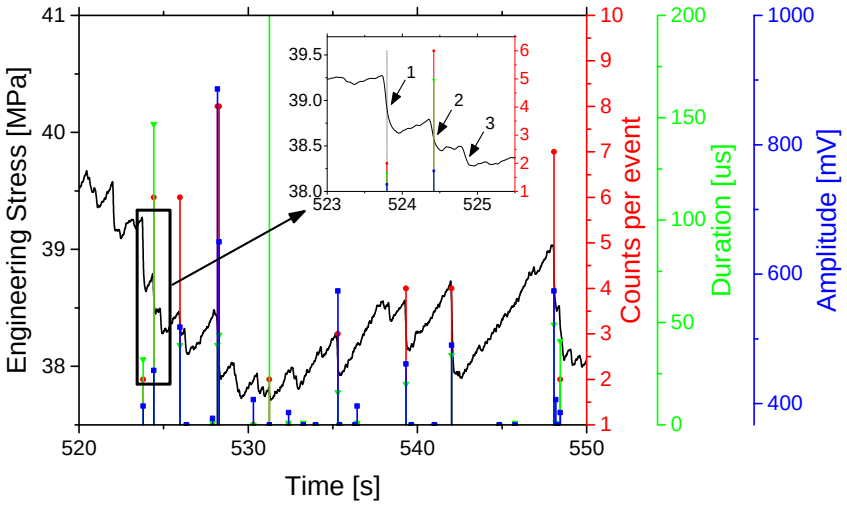

Figure 4.5: Compression test on a copper micropillar with precise simultaneous recording of the AE events and their parameters. Inset: successive load drops and corresponding AE response.

Tests on the second set of micropillars predeformed to lower strain were carried out using the abovementioned AE setup delivering a precise time stamps, therefore making possible a statistical evaluation of the data. Three types of micropillars were fabricated onto the copper substrate: a) pillars with side length of 2 µm and height of 6 µm, b) side length of 4 µm, height of 12 µm, and c) side length of 8 µm, height of 24 µm. Such different dimensions of micropillars enabled us to investigate also the size effect in their mechanical properties.

Compression data and the AE response (in terms of AE counts per event) of the largest pillars (side 8 µm, height 24 µm) are shown in Fig. 4.7a-d. It should

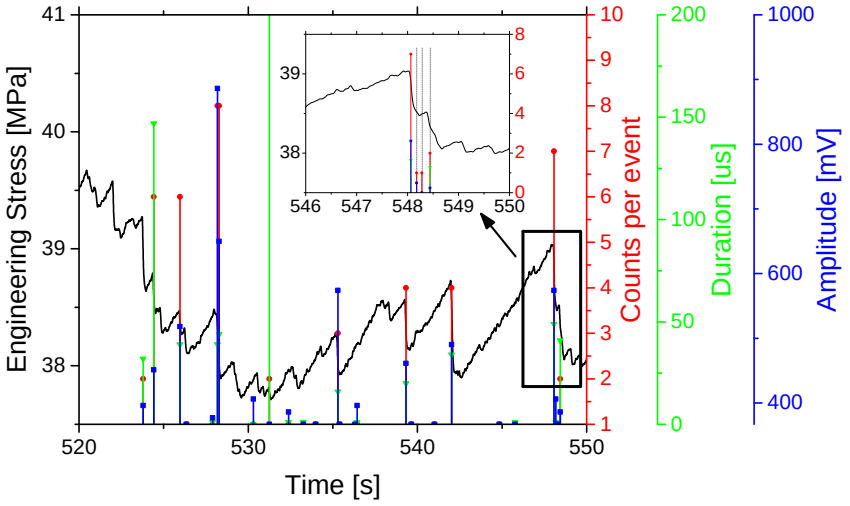

Figure 4.6: Compression test on a copper micropillar with precise simultaneous recording of the AE events and their parameters. Inset: fine structure of the load drop and corresponding AE response.

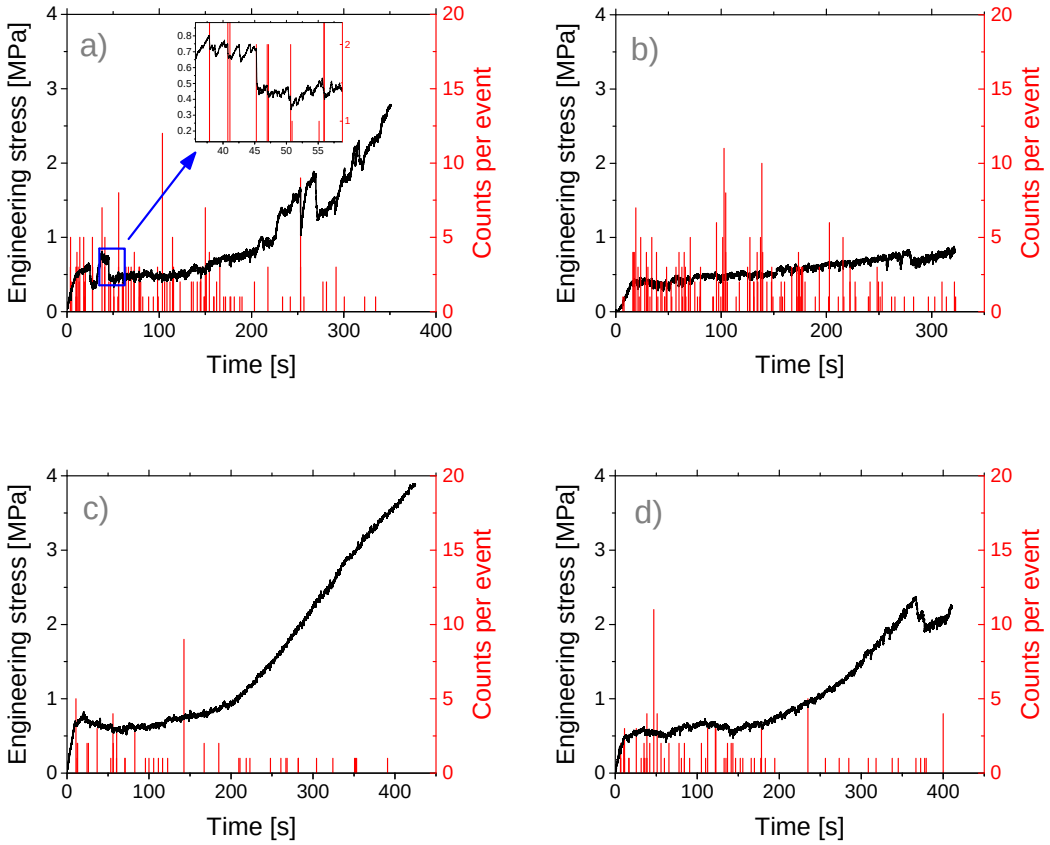

Figure 4.7: Compression curves and the AE response of copper micropillars from the second set with side length of 8 µm.

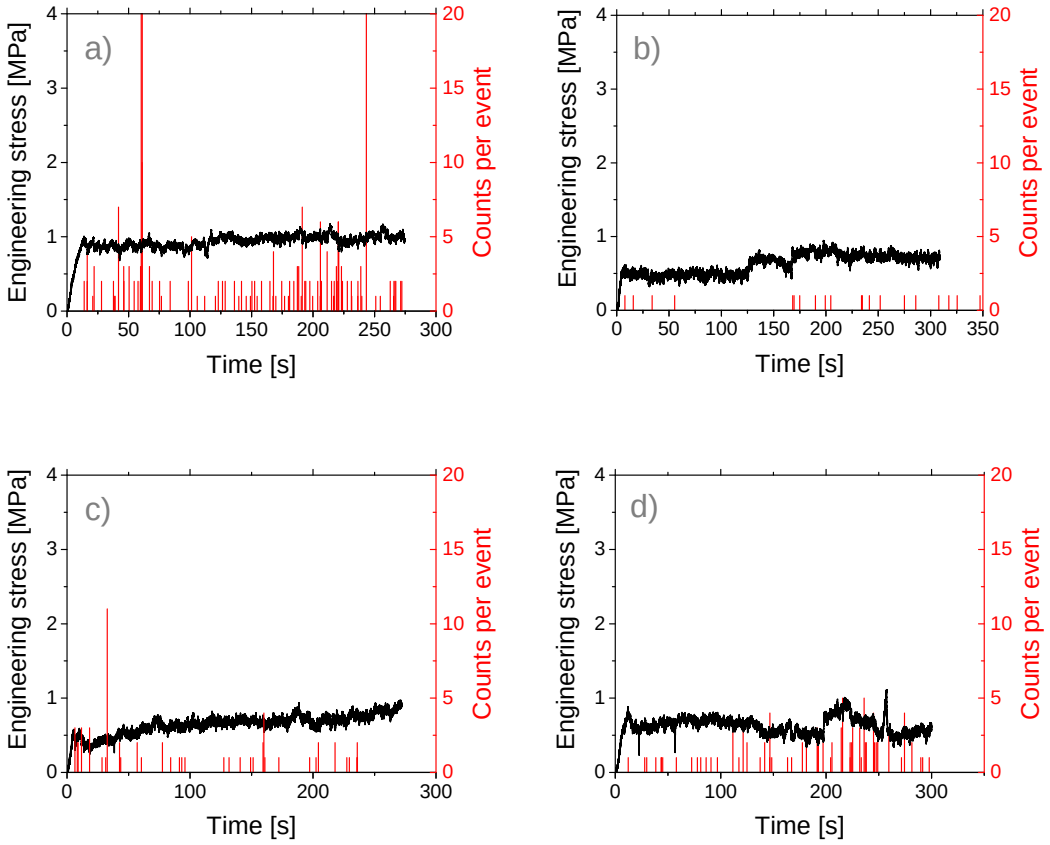

Figure 4.8: Compression curves and the AE response of copper micropillars from the second set with side length of 4 µm.

be mentioned here that the scales are different in these graphs compared with the first set in Fig. 4.2. The AE response is somewhat lower, and there is also a significant decrease in the mechanical strength in these micropillars. The AE activity is more pronounced in the plateau-like or "softer" regions of deformation and the correlations with the load drops on the deformation curve are observed in these samples, too (see the inset in Fig. 4.7a).

The results from compression tests on micropillars with side of 4 µm and height of 12 µm are shown in Fig. 4.8a-d. The deformation curves consist of an elastic region followed by a plateau in the flow stress till the end of the test. The compression is accompanied by a relatively weak AE activity.

During the compression of the smallest micropillars (2 µm in side length, 6 µm in height), practically no AE was detected. Individual curves from these tests are thus not shown here, however, the average curves of the tests performed on all three geometries of micropillars from this second set are presented in Fig. 4.9. As these three types of micropillars were fabricated onto the same bulk substrate,

they should vary only in one parameter, that is their size. Fig. 4.9 clearly shows that there is the size effect in the mechanical properties. The flow stresses are noticeably higher as the side length of the micropillar decreases, thus confirming the well-known conjecture that "the smaller is stronger" also in the microsamples used in this investigation.

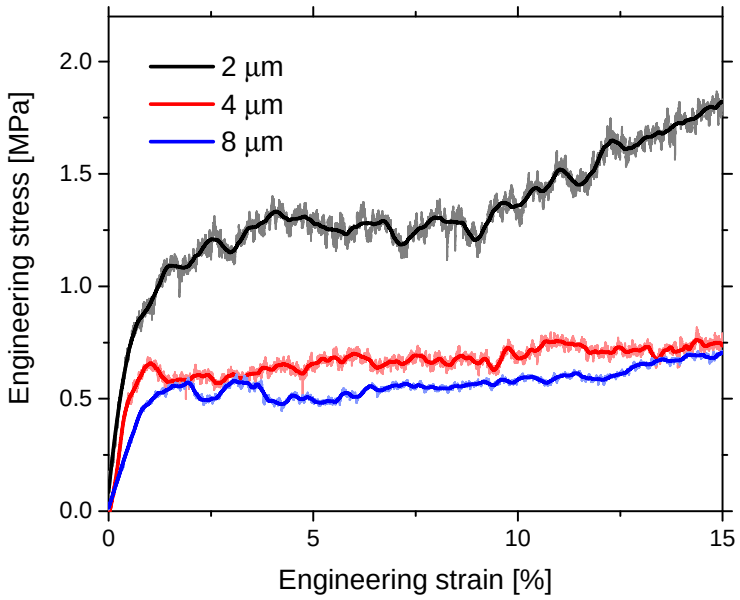

Figure 4.9: The size effect discovered in the flow stresses of copper micropillars from the second set, having three different geometries. Average curves from all the tests and their smoothed values (Savitzky-Golay filter, 1000 points) are displayed.

Diminishing AE activity with decreasing micropillar size has a twofold explanation. First, with decreasing micropillar dimensions there is implicitly a reduction in its volume. AE provides integral information from the whole specimen volume, therefore such a downsizing (all else constant) can lead to a declining AE activity. On the other hand, when the distance between dislocations becomes of the same scale as the specimen size, the plastic deformation starts to be carried by individual dislocations and exhaustion of dislocation sources takes place. This condition may arise as the side length of the pillar reaches 2 µm, thus hampering the collectiveness of dislocation activity, which in turn lead to the absence of AE. Two other arguments speak in favor of this second explanation:

- If the first argument were to be justified, the volume decrease would most likely lead only to a reduction in the number of events (since a lower amount of sources is present in the smaller volume), rather than their magnitudes.
- Size effect in the mechanical properties shown in Fig. 4.9 strongly indicates a change in the deformation mechanism with decreasing micropillar size.

In order to assess the relationship between the stress drops and the AE events, a procedure was employed (the algorithm is described in the Data treatment section) to collect the load drops from all the tests accompanied by the generation of AE, and to assign them to the corresponding AE events. In this way, a collection of data was obtained allowing for a statistical evaluation of stress drop sizes and possible correlations with the AE events parameters. In Fig. 4.10 "customized" histograms are shown representing average values of three typical AE event parameters: counts, amplitude, and duration, corresponding to a particular interval of stress drop magnitudes.

A slight increase in all AE parameters with the increasing drop size is present. Although there is only a relatively small number of events (several hundred) in the statistics and thus some scatter in the histograms is present, the increasing trend can be still identified. The AE event counts, amplitudes, and duration are thus larger, on average, for larger stress drops, even though individual load drops lead to an unpredictable AE response (as was shown in Fig. 4.5).

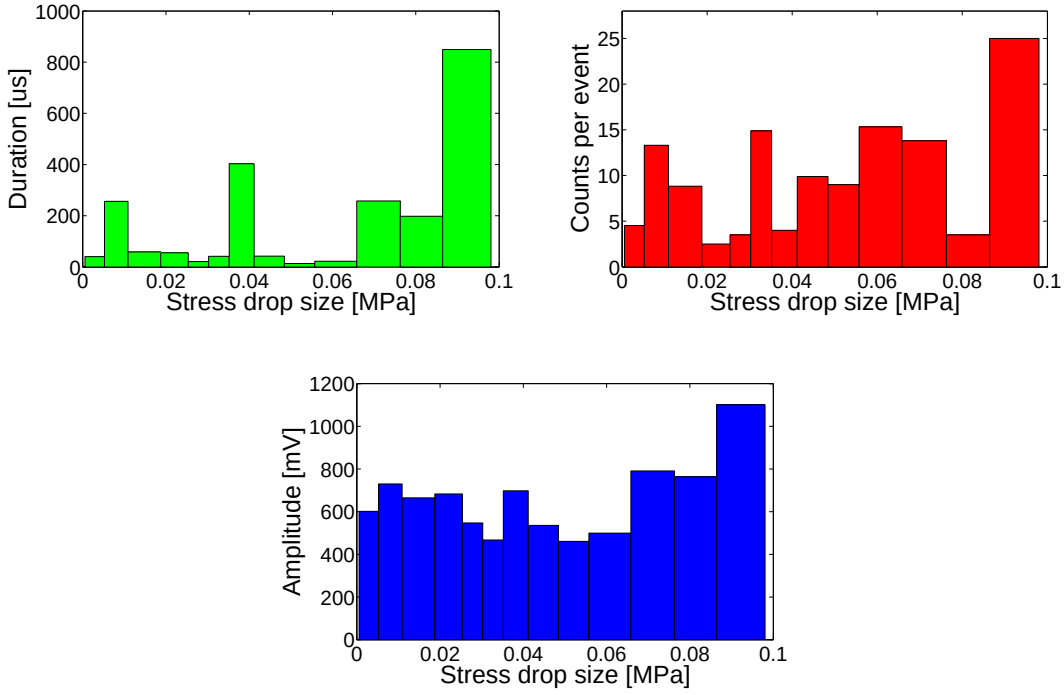

Figure 4.10: Distributions of the values of AE event parameters corresponding to the magnitude of stress drops in copper micropillars from the second set.

4.2 Aluminum microwires

Tensile tests on pure aluminum microwires with a concurrent recording of the AE were conducted in cooperation with EPFL, Lausanne. The diameter of wires was close to 100 µm. Due to the fabrication process, the individual microwires have

different orientations (see Tab. 4.1). Therefore, individual tensile curves exhibit different characteristics based on the orientation, which is a standard feature of fcc (and other) single crystals. Detailed evaluation of tensile stress-strain curves is however out of the scope of this work.

4.2.1 Results and discussion

Out of ten tested samples, four microwires produced a detectable AE, namely microwires 4, 6, 7 and 8. The results are shown in Fig. 4.11. The AE response was registered primarily in the early stage of tensile tests, shortly after the macroscopic yield point (wires 6, 7, and 8), or somewhat later (wire 4). Such behavior is typical of fcc single-crystalline metals, where the peak in the AE activity commonly begins at the onset of plastic flow, rises to its maximum, and then declines with increasing strain [96]. There is also a strong AE signal at the very end of the tests which results from a sample failure, confirming that there was a good acoustic contact between the wires and the AE transducer (test on microwire 4 in Fig. 4.11a was interrupted before the rupture took place). In the same way, the failure was registered by the AE device also from the samples that did not produce any other signals in the course of the test. The tensile curves of all aluminum microwires tested here are shown in Fig. 4.12

In the inset of Fig. 4.11b the data from the most AE-active microwire 6 are magnified, showing obvious correlations between the stress drops and the AE events. Such correlations were found in all four microwires and were further ex-

Table 4.1: Orientations and diameters of single-crystalline aluminum microwires tested in tension.

Sample	**[h k l]**	**Diameter** [µm]
microwire 1	[1 $\bar{1}$ 2]	105.0
microwire 2	[$\bar{1}$ $\bar{1}$ 8]	98.3
microwire 3	[4 3 1]	99.3
microwire 4	[0 4 $\bar{3}$]	100.0
microwire 5	[0 $\bar{3}$ 4]	106.0
microwire 6	[4 $\bar{3}$ 1]	104.0
microwire 7	[$\bar{3}$ 6 1]	99.0
microwire 8	[1 2 $\bar{1}$]	99.6
microwire 9	[1 1 0]	115.0
microwire 10	[4 $\bar{6}$ $\bar{1}$]	108.0

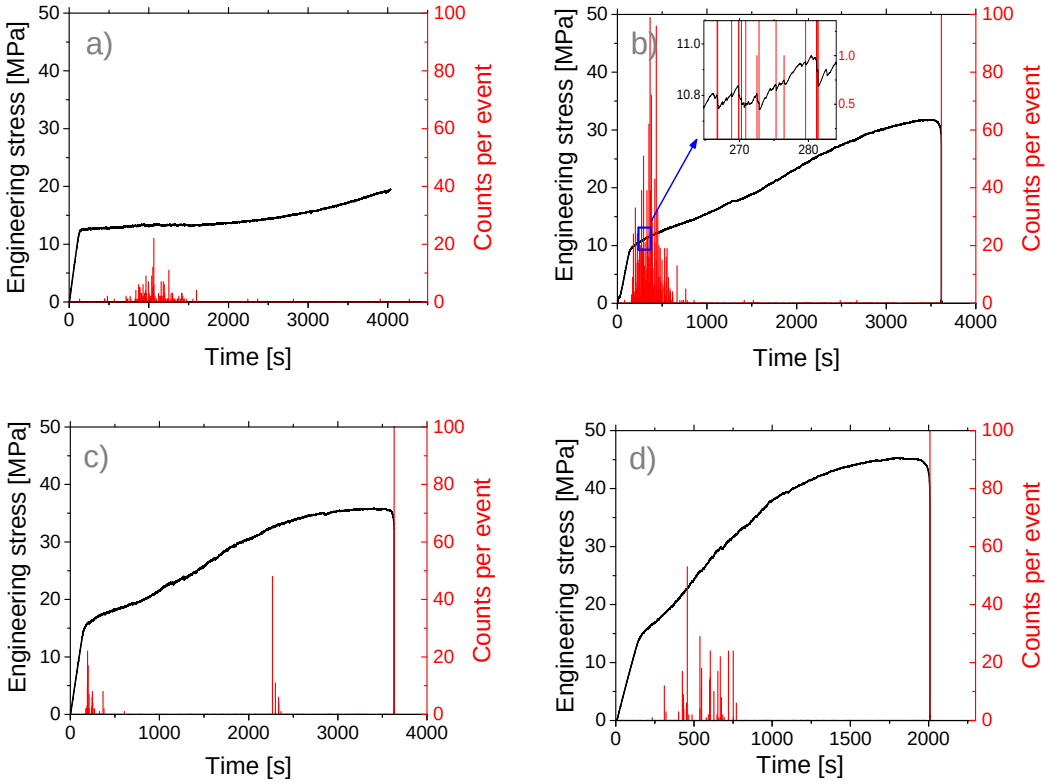

Figure 4.11: Tensile curves and the AE response of aluminum microwires tested in tension: a) microwire 4, b) microwire 6, c) microwire 7, and d) microwire 8.

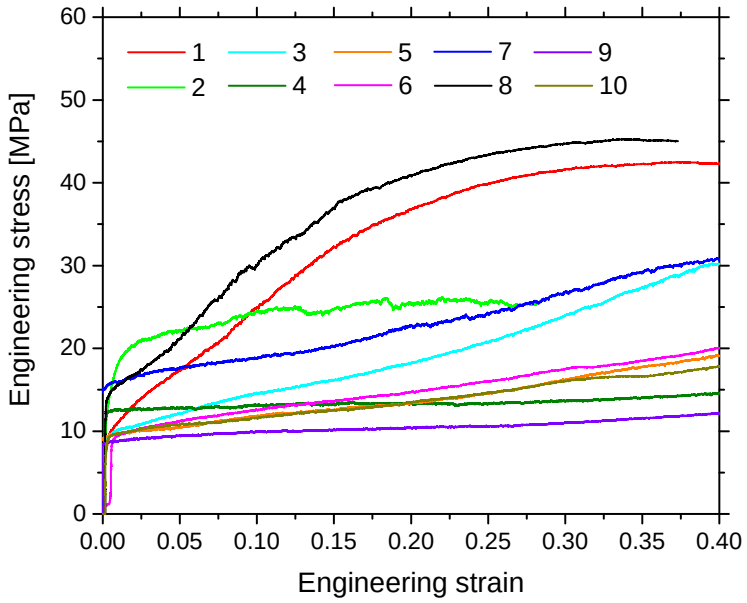

Figure 4.12: Tensile curves of all tested aluminum microwires.

amined. In Fig. 4.13a another graph is displayed showing data from this region of the test on microwire 6. A typical stress drop and resultant AE signal are marked with an arrow. A waveform of the corresponding AE event is shown in

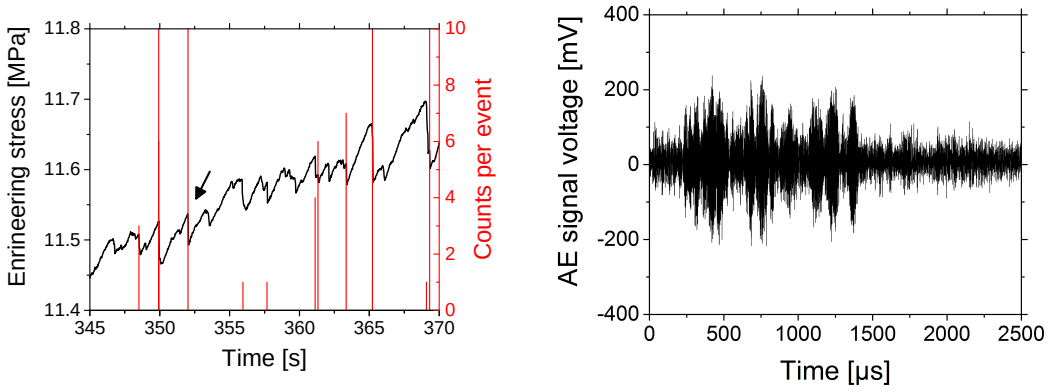

(a) typical stress drop

(b) corresponding waveform

Figure 4.13: Zoomed data (microwire 6) showing the stress drops and the AE signal corresponding to the drop marked with an arrow.

Fig. 4.13b, displaying successive and overlapping AE signals, which is a typical signature of dislocation avalanches.

Given the fabrication process, the initial dislocation density is expected to be relatively low and rather similar in the tested samples. The occurrence of the AE signals in these samples was not straightforward and most likely not related to the crystal orientation. Out of the four microwires, which produced AE during the test, three microwires — 4, 6, and 7 — had an orientation favorable for single slip, whereas microwire 8 was oriented for double slip. We did not therefore find any clear pattern in the AE response related to the slip systems being active. In Fig. 4.14 example SEM images of two tested microwires are shown. Microwire 4, which exhibits single-slip steps along its surface, produced AE signals during the test, which was shown to be in agreement with the response of samples 6 and 7, but unlike the other single slip microwire 10 displayed on the SEM micrograph, which did not emit acoustic signals. Further investigation and more data are needed to account for the absence of the AE activity in some samples and its presence in others.

As in the case of micropillars, statistical evaluation of the AE events related to the stress drops was performed for the microwires. Diagrams in Fig. 4.15 show distributions of values of the AE parameters. It can be seen that all the AE parameters (counts, amplitude, and duration) exhibit an increase in their values as the magnitude of stress drops increases up to 0.1 MPa, thus showing a positive relation between the drop size and the AE activity. Identical trends, although somewhat less pronounced, were evidenced in the data from micropillars. This observation suggests that the occurrence of larger drops is more likely to be driven by collective dislocation dynamics (resulting in distinctive dislocation

avalanches) when compared with the smaller drops.

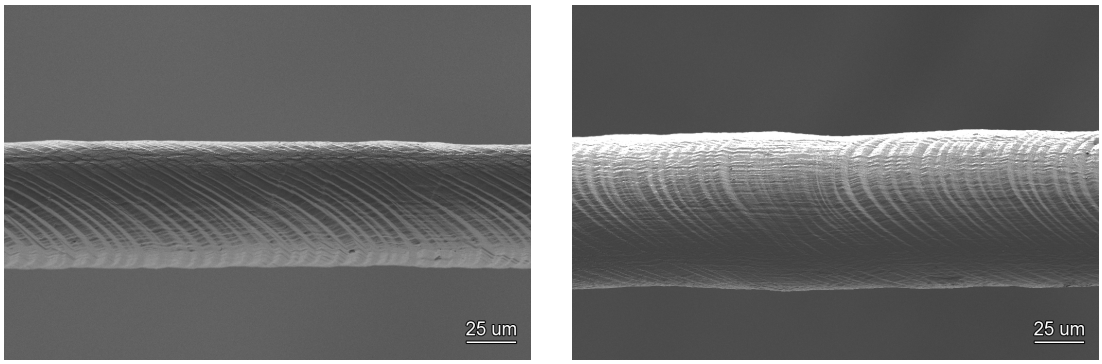

Figure 4.14: Example SEM micrographs of tested aluminum microwires. Left: microwire 4, Right: microwire 10, both oriented for single slip. (Courtesy of S. Verheyden, EPFL)

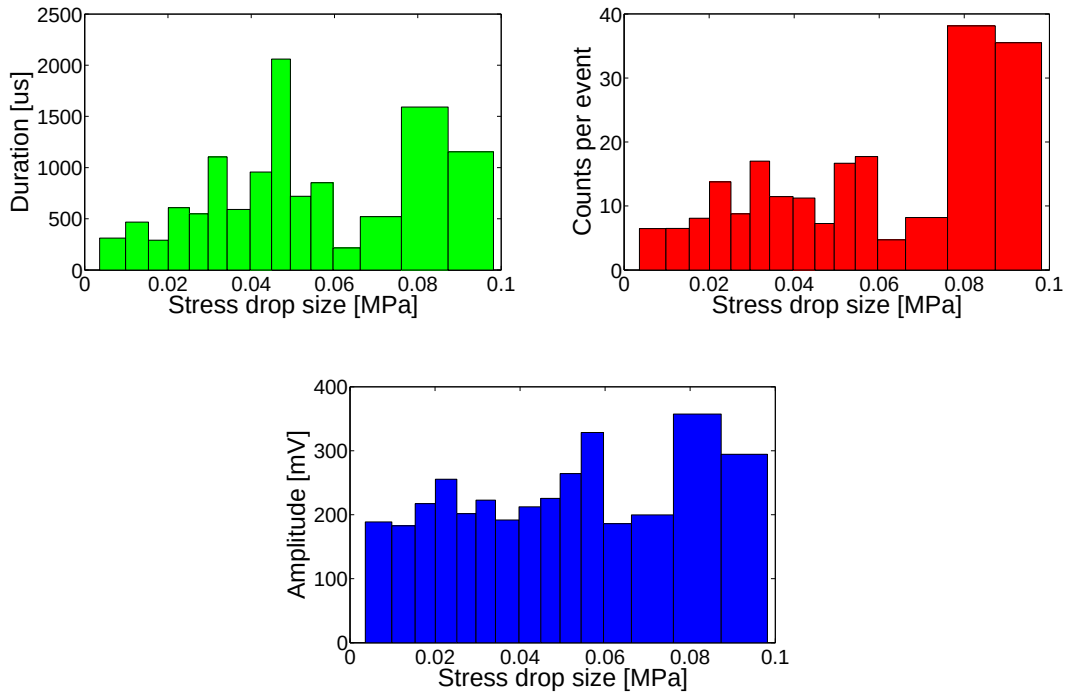

Figure 4.15: Distributions of the values of AE event parameters corresponding to the magnitude of stress drops in aluminum microwires.

5. Replicated aluminum foams: experimental procedure

5.1 Materials and sample preparation

The two main constituents used for the manufacture of foam samples were:

- Salt (sodium chloride) particles in two forms
  - coarse NaCl particles from Fluka Chemie GmbH, Buchs, Switzerland. The grain size was approximately 500 µm and the purity was ≥ 99.5 %,
  - finer NaCl grains supplied by Salines de Bex, Bex, Switzerland, having a grain size in the range 10–150 µm; the purity was roughly 98 %.
- Metals making the foam
  - 99.99 % pure aluminum purchased from Hydro Aluminum GmbH, Grevenbroich, Germany in the form of cast 26 kg ingots,
  - Al2Mg — pure aluminum containing 2.05±0.06 wt.% of magnesium, purchased from Alusuisse Technology & Management AG (Neuhausen am Rheinfall, Switzerland).

The foams tested in this work were produced at EPFL, Switzerland. In the following section, we briefly describe the sample preparation steps; details can be found in [69, 80].

5.1.1 Preform preparation

Sieving

In order to obtain a narrow distribution of NaCl particles, the powders were sieved according to the ISO 565 norm using an Analysette 3 apparatus from FRITSCH GmbH, Idar-Oberstein, Germany. In this way, salt powders comprising of grains of 400, 150, 75, and 25 µm in diameter were separated. The powders were then stored in airtight plastic containers.

Powder compaction

Based on prior experience, two groups of powders were prepared and processed in a slightly different way:

- first group: 400 µm powders (for the production on both, Al and Al2Mg foams) and 150 µm powders (only for Al foams),

- second group: 75 and 25 µm powders for Al foams; 150, 75, and 25 µm powders for Al2Mg foams.

In the case of the first group, the sieved salt particles were filled into a cylindrical silicone rubber mould (120 mm in height, 37 mm in diameter) and then vibrated to ensure the random dense packing. The rubber mould was sealed using latex condoms and inserted into a steel container filled with glycerin. Then, cold isostatic pressing was applied (30 kN for 1 min) in order to consolidate the powder.

For the compaction of fine powders (second group), smaller cylinders were used (50 mm in height, 12–14 mm in diameter) in order to ensure good powder consolidation. Otherwise, the process steps remained the same.

Infiltration

Cylindrical alumina crucibles (for the first group: inner diameter of 36–38 mm, 300 mm in height; for the second group: inner diameter of 12–14 mm, 150 mm in height; both closed with a hemispherical end) were used for the preform infiltration. Sintered salt preforms were put into the crucible coated with a graphite spray. A cylindrical cast metal ingot was placed inside the crucible on top of the preform. The crucible was then put into the gas pressure infiltration apparatus and the following procedure was carried out:

- heating from room temperature (RT) up to 700 °C in 90 min while evacuating the chamber to reach a pressure of 2–3 Pa in order to attain vacuum before the ingot was melted,
- keeping at 700 °C for 30–60 min to ensure complete melting of the metal. As a result, molten aluminum sealed the preform but did not infiltrate it due to adverse capillary forces,
- argon gas pressurized to 7 MPa was let into the apparatus to force the liquid metal into the preform (constant pressure was kept for 7 min to ensure complete infiltration),
- direct solidification of the metal was then induced by placing the crucible onto a copper chill while the pressure was still maintained in the apparatus until completion of metal solidification and cooldown.

Machining

Conventional techniques were used to machine the Al-NaCl ingots. The salt must be retained within the composite during machining to prevent crushing of the aluminum foam. The machining operations were therefore performed dry.

Salt dissolution

Standard salt removal can be performed in tap water. In order to minimize the oxidation of the samples, however, we used a chromate conversion solution (CCS, a corrosion inhibitor typically used to protect aluminum in saline environments) to leach the salt [128, 129]. The solution consisted of distilled water containing 1.62 g·l^{-1} of Na_2CrO_4 and 0.84 g·l^{-1} of $NaHCO_3$, corresponding to 0.01 mol concentration of both CrO_4 and HCO_3. The leaching time of 36–48 hours was used to guarantee total removal of the salt.

5.1.2 Specimens

The samples were prepared using the above-described method. Compression specimens dimensions and parameters are shown in Tab. 5.1[1]. As a result of many interconnected factors (particle size, preform size, infiltration pressure, etc.) affecting the volume fraction of solid V_s of final foam material, this quantity varies between different sets of samples. On the other hand, there is only a small variation in V_s of the samples within individual sample sets, as they were machined from the same ingot.

For the sake of simplicity, the sample sets will be hereafter referred to by acronyms as indicated in Tab. 5.1. Example photographs of two samples, Al75 and Al2Mg400, are shown in Fig. 5.1.

5.2 Experimental methods

5.2.1 Compression tests with concurrent acoustic emission acquisition

Compression tests were performed using a universal testing machine Instron 5882 at room temperature with a constant cross-head speed of 0.02 mm·s^{-1} (initial strain rate 10^{-3} s^{-1}). It should be noted here that the samples in this investigation contain a great number of pores and even the samples with the largest pore size (400 µm) have ∼50 pores along the shortest sample dimension. That is far more than the level typically required for data to be representative of the

[1] In order to ensure consistency of the experiments, some of the produced samples had to be discarded and are not listed in Tab. 5.1. There were a couple of samples containing inhomogeneities (these samples were most probably located near one of the ingot ends and were not completely infiltrated with a metal). In addition, the entire set of Al2Mg samples with a pore diameter of 150 µm had to be also rejected due to an apparent oxidation that could be observed visually. Other sample sets did not suffer from such imperfections.

Table 5.1: A list of salt-replicated microcellular samples prepared in this work.

Material	**Pore size [µm]**	**Diameter×height [mm]**	**Number of samples**	V_s [%]
Al	400	20×20	4	24.5–25.9
	150	10×20	8	26.9–27.5
	75	10×20	8	29.9–31.7
	25	10×20	3	35.8–36.4
Al2Mg	400	10×20	15	22.8–23.7
	75	10×20	8	30.8–33.1
	25	10×20	8	40.2–44.9

Figure 5.1: Photographs of: Al2Mg, pore size 400 µm (left) and Al, pore size 75 µm (right) salt-replicated foam samples.

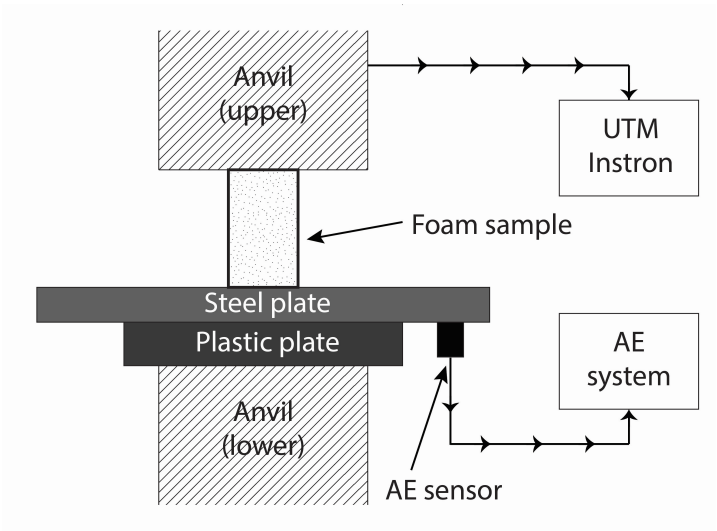

Figure 5.2: Experimental setup used for the uniaxial compression tests with concurrent AE recording.

material free of edge effects [71, 72, 87].

In order to record AE signals accompanying the compression of foam samples, the set-up shown in Fig. 5.2 was used (details in [130]), where a plastic plate was placed on top of the lower anvil of the UTM to insulate and prevent possible vibrations to interfere with the AE signals generated within the sample during testing. A flat steel plate, supposed to be in contact with the sample, was placed on the plastic plate. Due to a good "acoustic conductivity" of steel, sound waves originating in the tested samples were routed to the AE transducer which was attached to an end of the plate with the help of a wooden clip. The acoustic contact was also improved by the use of vacuum grease. The advantage of this setup is that the AE transducer can be kept in place throughout all the tests (only the sample is to be replaced by another one after each test), thus minimizing the possibility of variations in the acoustic contact between the samples with a circular cross section and the flat-end AE sensor.

AE acquisition was performed using a Physical Acoustics Corporation (PAC) PCI-2 board and a broadband AE sensor, also manufactured by PAC. To ensure high signal-to-noise ratio, a preamplifier with a gain set to 60 dB was used. The AE parameters were obtained by hit-based processing, in which the threshold level was set to 26 dB. The continuous AE streaming data were also recorded with a sampling rate of 2 MHz and stored.

5.2.2 Analysis of acoustic signals

Visual examination of AE signals allows distinguishing the main waveforms of acoustic signals accompanying plastic deformation of the material. Additional

quantitative information can be derived from spectral analysis of individual waveforms and raw signals. Spectral analysis was performed using a short-time Fourier transform (STFT) implemented as *spectrogram* Matlab function. Due to the large file size of raw acoustic signals, a block-wise processing was needed to be employed in order to bypass memory limitations.

To shed more light on the deformation mechanisms being active during the compression of foam samples, the AE signals were further analyzed using the Adaptive Sequential k-means (ASK) procedure. The ASK analysis, introduced recently by Pomponi and Vinogradov [131], uses a statistical approach for classifying the AE signals with different emitting sources. Details can be found in [131] and only a brief overview of the main steps is given here:

- The recorded AE signals are sectioned using so-called *time windows*. The window size can be varied; in the present work 500 µs window was used.
- For each time window, the power spectral density (PSD) of the signal is calculated.
- The characteristic features (such as median frequency, AE energy, peak value, etc.) are determined from the PSD function for data within the time window.
- The first cluster is defined by the parameters of the PSD in the first window.
- PSDs in the consecutive windows are analyzed one by one. If the statistical properties of a given PSD are similar to those in an already existing cluster, then this PSD is assigned to this cluster. Otherwise, a new cluster is established. The conditions for forming a new cluster are based on the *k-means* clustering method (see [131]).

When the clustering procedure is completed, a dominant AE source mechanism is assigned to each cluster. The assignment consists of three basic steps:

1. Examination of strain or stress at which the number of elements in a given cluster starts to increase. For example, the elements in the first cluster must belong to the background noise because the recording of the AE data starts already before the deformation to collect a sequence of the noise signal.
2. Inspection of the characteristic features of the PSDs, e.g. energy, frequency distribution, mean frequency, etc. For example, dislocation motion typically emits a low-frequency signal [33, 131].
3. Comparison of the time evolution of the number of elements in a given cluster with the deformation data and/or other supplementary datasets.

5.2.3 Microstructure characterization

The microstructure was observed using an SEM system Zeiss Auriga Compact equipped with the field emission gun (FEG) and the EDAX EDX detector. The micrographs were captured with SEM operating in secondary electrons imaging mode.

5.2.4 Digital image correlation (DIC) analysis

The DIC experiments were employed to reveal how the deformation proceeds within salt-replicated microporous samples. Pure Al foam sample, 10 mm in diameter and 20 mm in height was used for the experiment. The pore size of the sample was 400 µm and the volume fraction of solid was ∼24 %.

In order to assess the compression behavior of salt-replicated sample, a more conventional type of foam, namely metal matrix syntactic foam (MMS), was also analyzed. This type of metal foam is produced using the pressure infiltration technique [132] and comprises a metal matrix containing relatively large ceramic hollow spheres. Technical purity Al99.5 (99.5 wt.% Al, 0.25 wt.% Si, 0.40 wt.% Fe) matrix containing 65 vol.% of hollow spheres was used to make a foam. The hollow ceramic spheres consisted of 35 wt.% Al_2O_3, 45 wt.% SiO_2 and 20 wt.% mullite. The average outer diameter and wall thickness of the spheres were 1.45 mm and 58 µm, respectively; and the density was 1.81 g·cm^{-3}.

Uniaxial compression tests were performed using Instron 5882 screw-driven testing machine; constant crosshead speed was set to 0.02 m·s^{-1} (i.e. conditions identical to the AE experiments). The high-resolution camera was used to record the deformation process. Still images were captured with a time interval of 1 second. The DIC analysis was performed using *ncorr* evaluation algorithm implemented in Matlab [133, 134].

6. Replicated aluminum foams: experimental results

6.1 Microstructure characterization

Foams are visually regular, showing homogeneously distributed features where the pores can be distinguished by the naked eye for the samples with large pore size. With pores 75 µm or below, the porous nature of the foams starts to be no longer clearly discerned by visual inspection and the material appears as a very light, slightly matt metal.

Fig. 6.1 represents an SEM micrograph of the surface of Al (pore size 400 and 150 µm), and Al2Mg (pore size 400 and 150 µm) pure Al foam specimens. Some parallel machining marks can be distinguished originating in the machining using a lathe. In foams with 75 µm pores (mostly in the Al sample), a smearing of the metal perturbs to some extent the observation of the pore structure. It can be seen that the aluminum foam mesostructure reproduces nicely (in inverse) the salt preform pore structure.

It was ascertained in previous studies that a slow directional solidification of

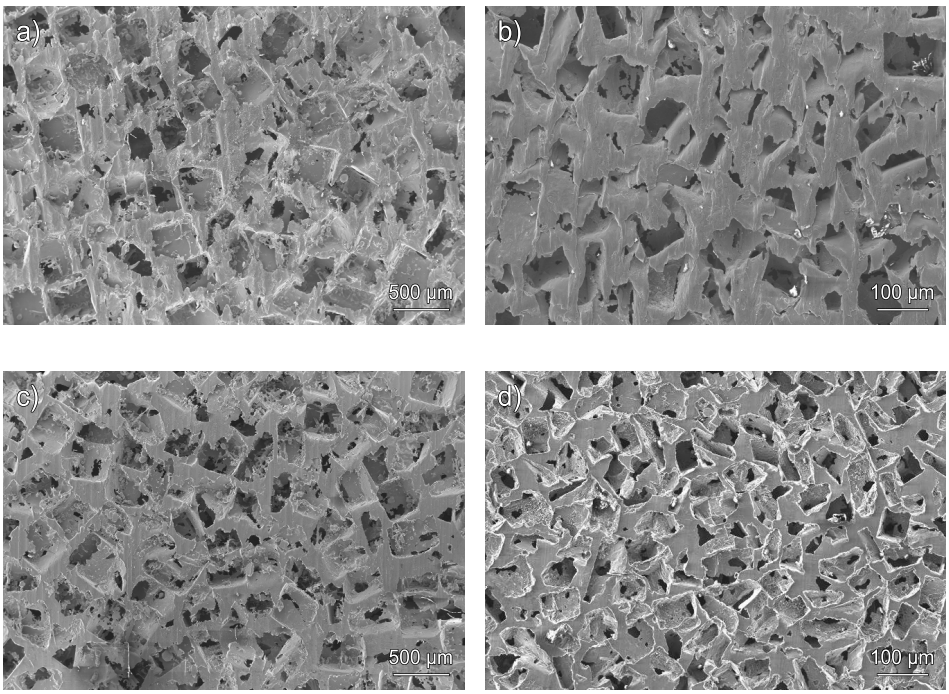

Figure 6.1: SEM micrographs of the machined surfaces of pure Al replicated foams made out of a) 400 µm and b) 150 µm salt preforms; and Al2Mg replicated foams made out of c) 400 µm and d) 75 µm salt preforms.

molten metal during fabrication of replicated foams results in a very large grain size compared with all pore sizes investigated in this work [34, 69, 87]. Typical grain sizes were shown to be on the order of a centimeter. It is worth noting that the metal making individual struts, nodes, or even around each cell in the foam, is therefore practically always a single crystal.

6.1.1 Uniaxial compression tests

Two to four samples from each set were tested in compression simultaneously with the AE acquisition. The compression stress-strain curves obtained for Al400, Al150, Al75, and Al25 sample sets are shown in Fig. 6.2. The curves are smooth, as is characteristic of replicated microcellular aluminum compression. Since the foams are comprised of many struts connected by nodes, the deformation of a foam material under compression is driven by collective deformation of single struts, which primarily deform by bending and also by some degree of torsion, tension, and compression [34]. The stress-strain dependence (as well as the corresponding AE response discussed later) recorded in the compression tests are,

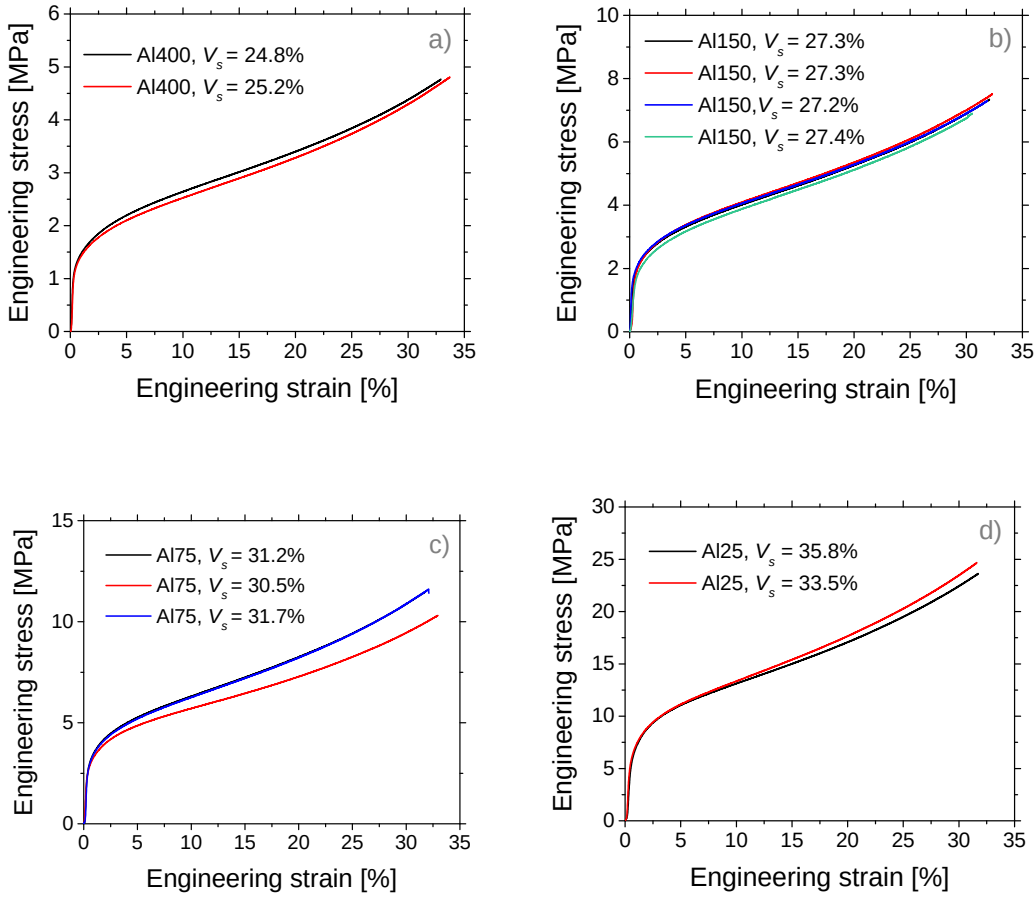

Figure 6.2: Compression stress strain curves of Al foam sample sets with different pore size of: a) 400 µm, b) 150 µm, c) 75 µm, and d) 25 µm.

therefore, the collective signals coming from many variously stressed small single crystals of irregular shape. As these crystals deform, they deform independently, interacting one with another, from strut to strut, via the nodes. The struts diameters are approximately of the order of one-tenth of the pore diameter. Thus, at these sizes, each strut is likely to deform plastically in intermittent mode [26]. Therefore, the recorded stress-strain curves are a collection of strain bursts from individual struts, each of which might emit the signal characteristic of intermittent deformation.

The foams continuously harden at all strains, thus resembling a behavior similar to the bulk material [32, 71–73, 87, 128, 135–137]. The stress-strain curves of each set almost superimpose, showing a good reproducibility of the results. This can be directly related to the fact mentioned above, that the volume fraction of solid V_s is rather constant across the samples originating in the same ingot. Moreover, finer pore samples exhibit a higher flow stress, as seen by comparing the deformation curves from 400 up to 25 µm pore sizes in Fig. 6.3. Such a comparison is, however, not that straightforward as the variations in V_s between the individual sample sets are quite significant and therefore must not be neglected.

To account for this effect and to be able to quantify the plasticity size effect, we first determined for each sample the stresses at 0.2, 1, 2, 3, 5, and 10 % plastic deformation (details of the method can be found in [69, 87, 137]). These values (shown in Tab. 6.1) are obviously still affected by the relative foam density

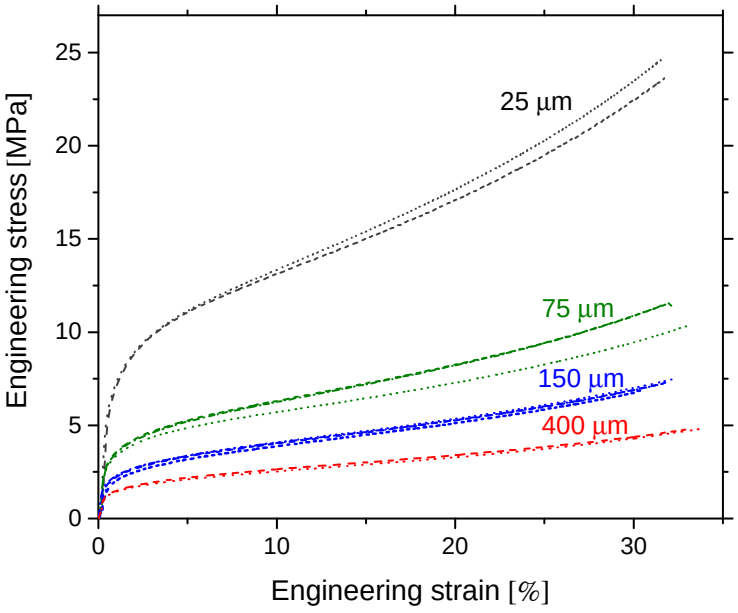

Figure 6.3: Comparison of the compression stress-strain curves of all Al samples. Red: 400 µm, blue: 150 µm, green: 75 µm, and black: 25 µm pore size.

Table 6.1: Flow stresses of Al foam samples calculated at 0.2, 1, 2, 3, 5, and 10 % plastic deformation.

Strain	**Flow Stress [MPa]**										
	Al400		**Al150**				**Al75**			**Al25**	
0.2 %	1.25	1.22	1.97	2.01	1.85	2.01	2.94	2.79	2.98	6.18	6.12
1 %	1.60	1.56	2.54	2.57	2.47	2.55	3.91	3.66	3.88	8.34	8.28
2 %	1.84	1.77	2.91	2.94	2.82	2.90	4.48	4.18	4.43	9.58	9.52
3 %	2.01	1.93	3.15	3.18	3.08	3.15	4.85	4.52	4.81	10.37	10.37
5 %	2.25	2.16	3.52	3.57	3.46	3.53	5.42	5.00	5.37	11.46	11.52
10 %	2.69	2.58	4.22	4.27	4.14	4.23	6.45	5.83	6.42	13.48	13.72

V_s (24–36 % for the Al samples). To eliminate this factor, a relatively simple calculation can be employed, where the foam sample flow stress, σ^*, is scaled using a power-law relation deduced by a mean square regression of data for replicated microcellular metals with a pore size of 400 µm [69, 87].

$$\frac{\sigma^*}{\sigma_0} = 1.62 V_s^{2.5}, \tag{6.1}$$

where σ_0 is the intrinsic flow stress of the dense metal with low dislocation density (for intact undeformed aluminum foam this value can be estimated experimentally using the microindentation of larger foam struts in 400 µm pore size samples). It can be seen in Fig. 6.4 that the plasticity size effect is present in Al foam sets even after this correction, as there is a clear increase in the flow stresses at fixed strains as the pore size decreases.

Standard Taylor relationship can be further used to calculate the global dislocation density if classical (dislocation) work hardening is the only hardening mechanism taking place during the plastic deformation. This condition is fulfilled in the highly pure aluminum used in this study, and therefore, the dislocation density ρ_d can be calculated as:

$$\rho_d = \left(\frac{\sigma_0}{\alpha_T G b} \right)^2 \tag{6.2}$$

where $\alpha_T = 1.25$ is a correction factor specific to Al, b is the magnitude of the Burgers vector ($2.86 \cdot 10^{-10}$ for Al) and $G = 26$ GPa is the shear modulus of Al.

If we assume a simple model where the foam pores are spherical [69, 138], the average surface-to-surface mean free path l can also be calculated as a function

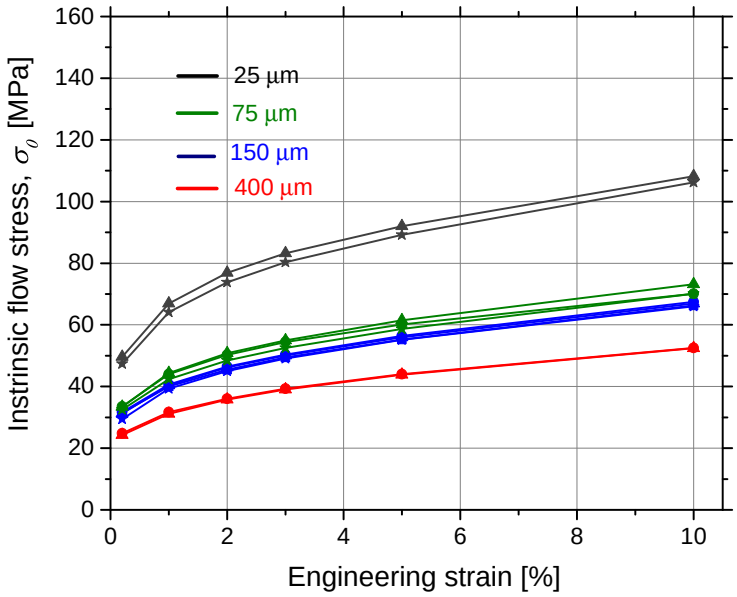

Figure 6.4: Intrinsic flow stresses calculated at fixed strain values for Al foam samples.

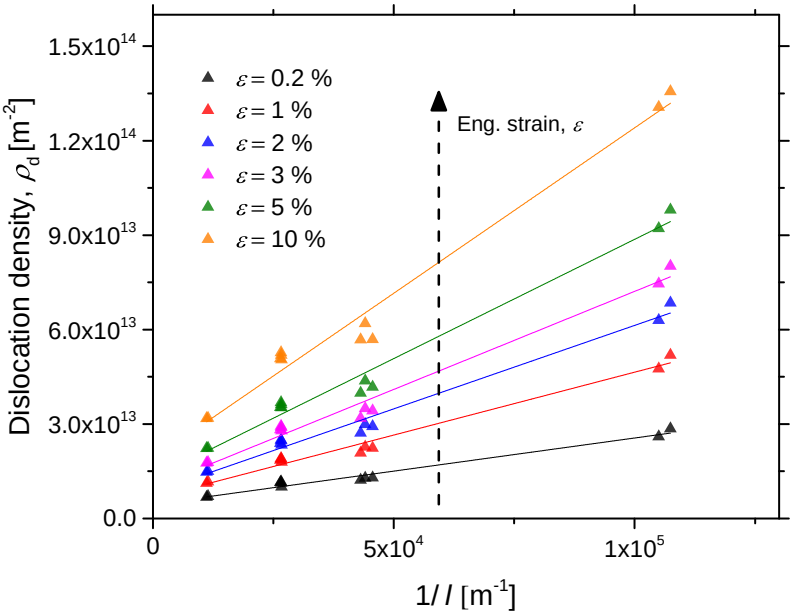

Figure 6.5: Dislocation density ρ_d against the inverse of average mean free path l calculated from the stresses determined at fixed plastic strains.

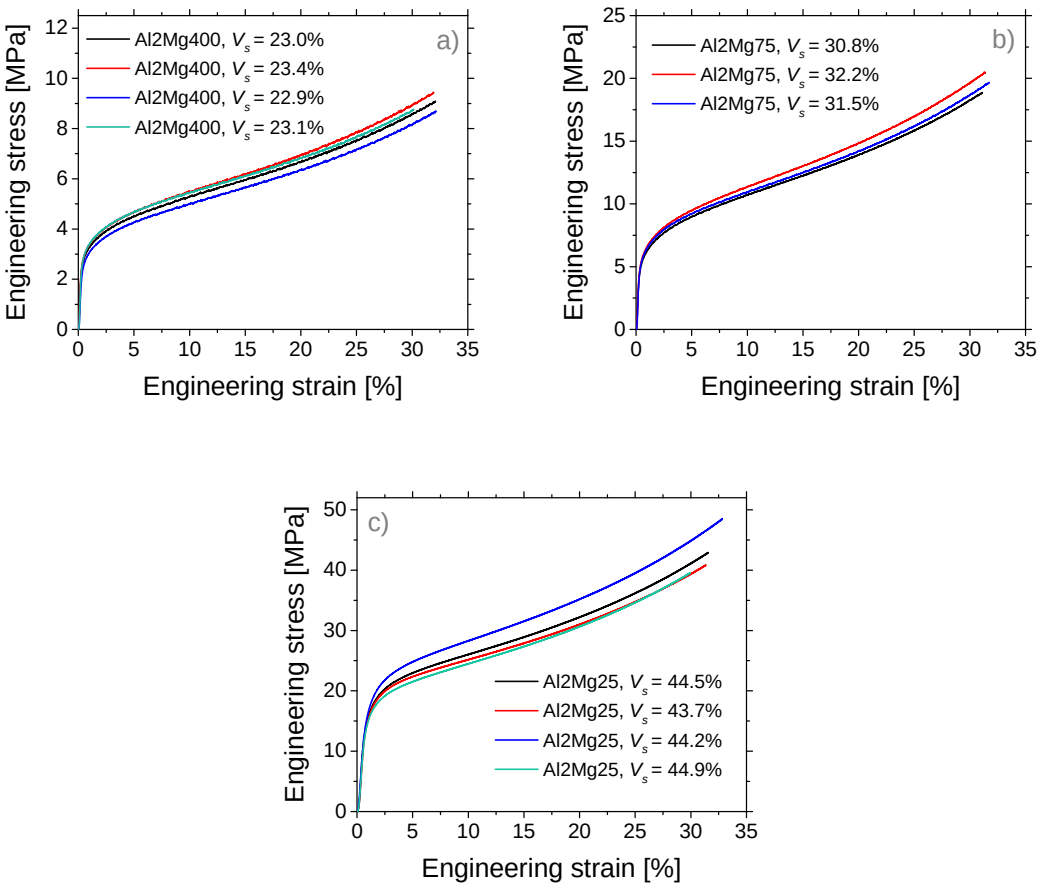

Figure 6.6: Compression stress strain curves of Al2Mg foam sample sets with different pore size of: 400, 75, and 25 µm.

of pore diameter d_p, and volume fraction of solid V_s:

$$l = d_\mathrm{p}\left(\frac{2V_\mathrm{s}}{3\left(1-V_\mathrm{s}\right)}\right) \tag{6.3}$$

Fig. 6.5 shows values of dislocation density ρ_d plotted against the inverse of average mean free path l calculated from the stresses determined at 0.2, 1, 2, 3, 5, and 10 % plastic strains. The data follow a linear relation for each of the fixed plastic strain levels. This is expected if the size effect is attributable to Taylor hardening originating in the emission of geometrically necessary dislocations. Positive slopes demonstrate again a clear size effect in the plastic deformation and these data are perfectly in line with the recent findings of Goodall et al. [87].

The Al2Mg compression curves shown in Fig. 6.6 also superimpose nicely within each set. When all three sets are plotted together to allow for a direct comparison, the size effect is apparently evidenced also in these foams (shown in Fig. 6.7). Al2Mg foam samples, however, suffer from even more pronounced variation in the volume fraction of solid V_s, when compared with the sets of pure Al foams. After the correction, using Eq. 6.1 again to calculate the intrinsic flow

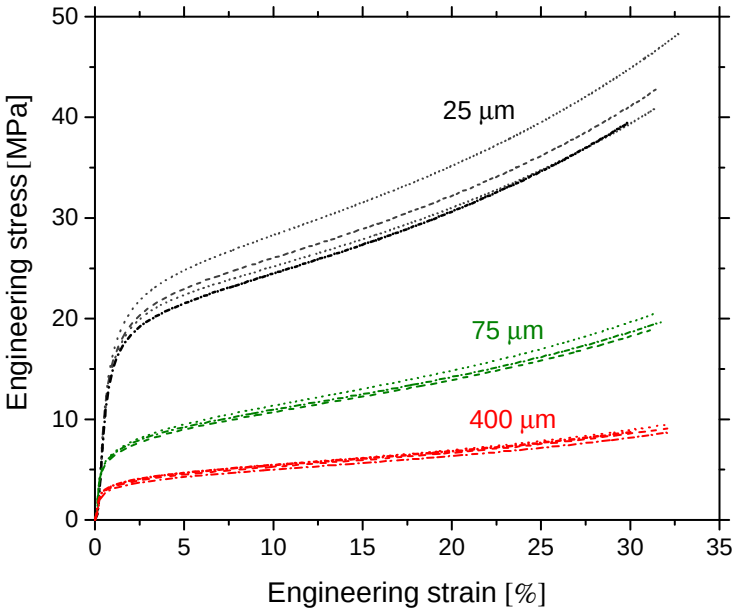

Figure 6.7: Comparison of the compression stress-strain curves of all Al2Mg samples.

stresses, σ_0, from the foam flow stresses, σ^*, at selected plastic strain levels (Tab. 6.2), the size effect vanishes. This is manifested in Fig. 6.8 showing that, given the experimental error typical for investigations on metal foams, the curves rather superimpose. Such behavior is indeed expected since there is another hardening mechanism active, i.e. the solid solution hardening, that is characteristic for the samples made from metal alloy. As a result, we also cannot simply use Eq. 6.2 to estimate the dislocation density, as it is valid solely for Taylor hardening.

In addition, an intriguing feature can be observed in Fig. 6.6, that is the serrations on the Al2Mg400 and (somewhat less pronounced) Al2Mg75 stress-strain curves. The saw-tooth curve is typically a signature of the Portevin-Le

Table 6.2: Flow stresses of Al2Mg foam samples calculated at 0.2, 1, 2, 3, 5, and 10 % plastic deformation.

Strain	**Flow Stress [MPa]**										
	Al2Mg400				**Al2Mg75**			**Al2Mg25**			
0.2 %	2.72	2.89	2.68	2.90	5.27	5.57	5.49	14.37	14.78	15.56	14.29
1 %	3.46	3.62	3.36	3.66	6.79	7.12	7.01	18.80	18.75	20.41	18.07
2 %	3.85	4.07	3.75	4.07	7.67	8.10	7.91	20.86	20.60	22.59	19.73
3 %	4.16	4.37	4.02	4.37	8.31	8.76	8.53	22.06	21.64	23.87	20.75
5 %	4.57	4.82	4.40	4.80	9.22	9.74	9.50	23.63	23.09	25.68	22.24
10 %	5.33	5.61	5.13	5.54	10.94	11.57	11.15	26.66	25.81	29.06	25.14

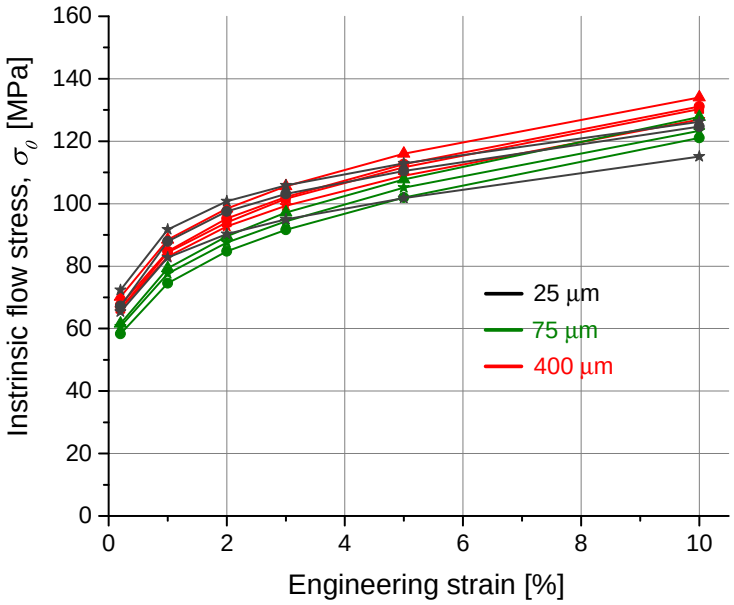

Figure 6.8: Intrinsic flow stresses calculated at fixed strains for Al2Mg foam samples.

Châtelier effect and will be analyzed below with the help of AE.

6.1.2 Digital image correlation

In Fig. 6.9 a total displacement of a) MMS foam b) and salt-replicated foam at 5, 10, and 15 % plastic strain is shown. It is observed that, compared with MMS foams, salt-replicated aluminum foams deform much more uniformly. The displacement maps show gradient-like displacement distribution even up to the relatively high strain of 15 %. On the other hand, syntactic foams exhibit disintegration and crumbling. The MMS sample breaks into two fragments already at the strain of 5 %. At 10 %, two more individual areas are formed which "move" separately up to 15 %. This is also confirmed in the strain maps (Fig. 6.10), where in the case of syntactic foams clear bands are formed where the deformation is localized. In replicated foam, on the other hand, no substantial collapse bands are formed even though a minor localization of strain is present in the center of the sample. These results confirm that, unlike conventional metal foams, salt-replicated open-cell foams exhibit homogeneous plastic flow.

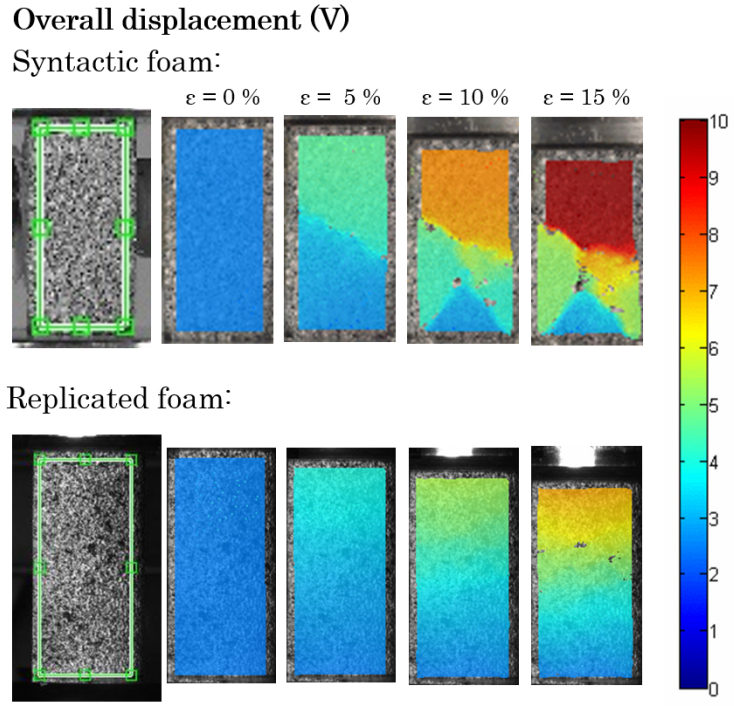

Figure 6.9: Overall displacement DIC maps of a) syntactic Al foam, b) salt-replicated pure Al foam.

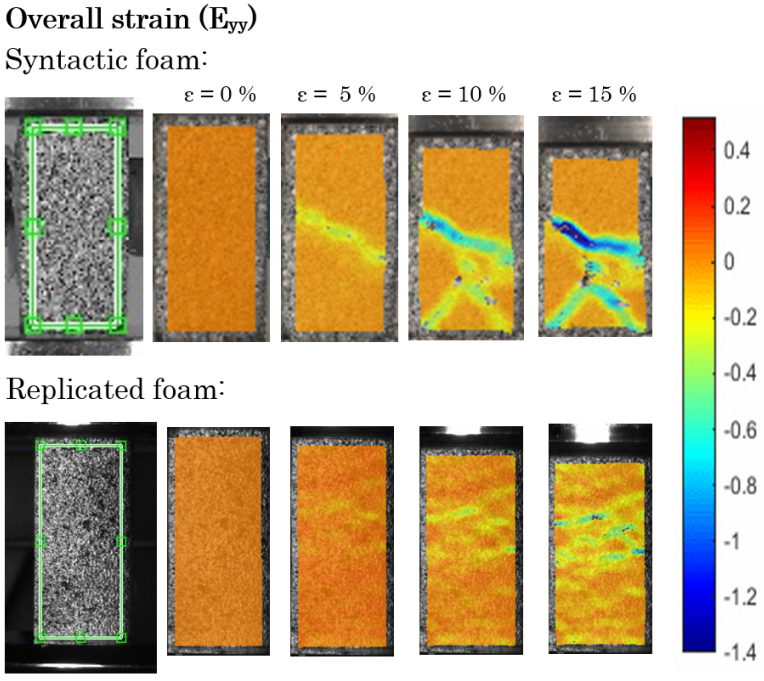

Figure 6.10: Overall strain DIC maps of a) syntactic Al foam, b) salt-replicated pure Al foam.

6.1.3 Acoustic emission

In Fig. 6.11a-d the compression curves of Al foams samples in combination with the AE parameters are presented. Only one sample from each sample type is shown, as all the tests were highly consistent and very similar AE data from each sample originating in the same set (ingot) were collected. Two characteristic AE parameters are examined, namely counts per AE event and AE event amplitudes. Strong AE activity around the yield point[1] is present throughout all the tests, with the decreasing trend towards the sample sets with smaller pore size. In the case of Al400 samples, the AE response remains relative intense in the course of the entire test. Samples from the sets with finer pores (Al150, Al75, and Al25) exhibit quite a rapid decrease in AE counts after the yield point and remain almost silent till the end of the test. In terms of AE amplitudes, however, the AE signals in the later stages of the compression, although very scarce, remain relatively intense.

[1]In this context, the yield point is presumed to be a point on the stress-strain curve where apparent elastic region ends. It is not possible to precisely define the yield point of metal foams because plasticity sets in early during the deformation due to a high density of stress concentration sites [69, 72].

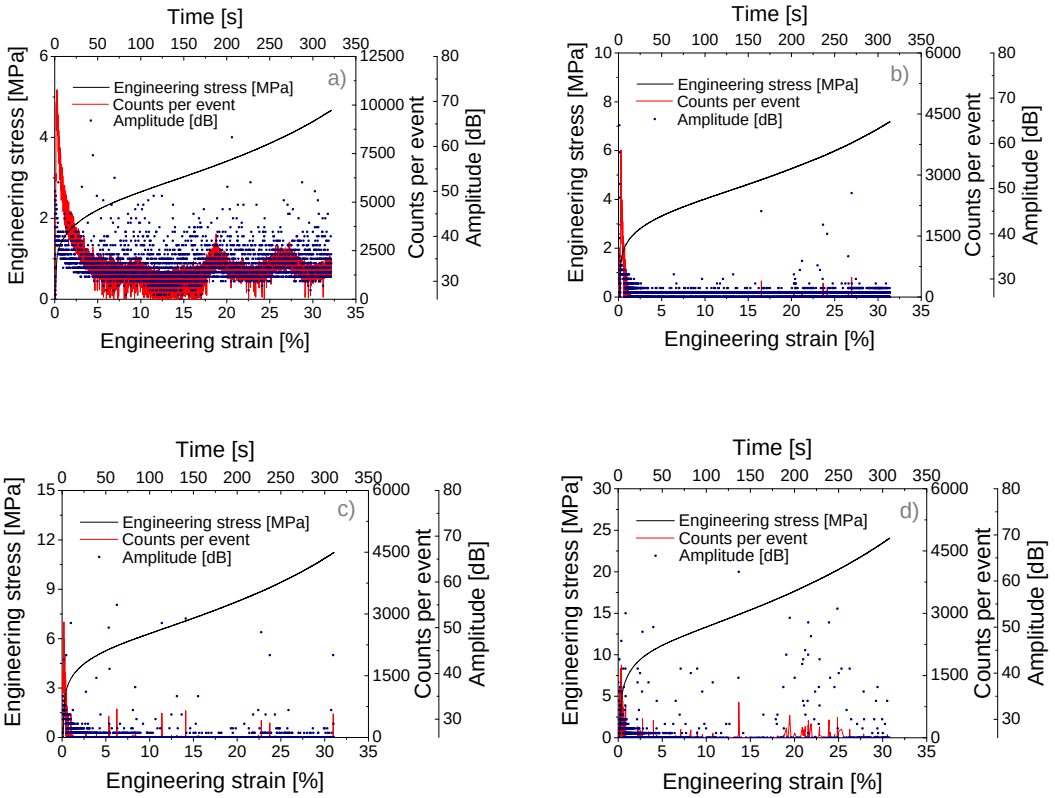

Figure 6.11: AE data recorded during the compression of Al foam samples: a) Al400, b) Al150, c) Al75, and d) Al25.

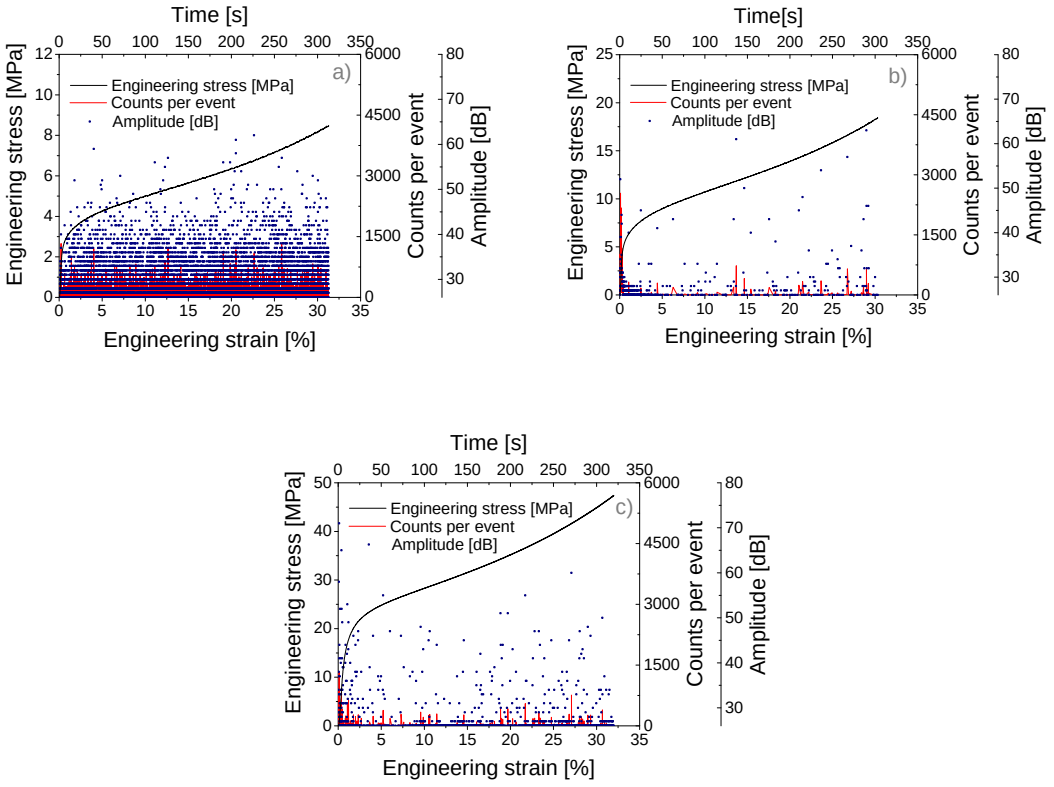

Figure 6.12: AE data recorded during the compression of Al2Mg foam samples: a) Al2Mg400, b) Al2Mg75, and c) Al2Mg25.

Similarly, Fig. 6.12a-c. show the data of Al2Mg samples. The AE response characteristics are similar to the Al microcellular samples in that, that the AE activity is stronger in the vicinity of the yield point. The effect is, however, slightly less pronounced in Al2Mg400 and almost absent in Al2Mg25. Samples Al2Mg400 with coarse pores are again the only samples to exhibit strong AE signals even in the post-yield stages of compression, and the AE signals remain constant until the end of the test. The AE amplitudes are quite moderate at the beginning of tests, given a relatively high value of counts per event in this stage of deformation. Later on, the AE signals are intermittent and not very frequent; but if present, the magnitude of their amplitudes is rather large, as in the pure Al foam samples.

6.2 Discussion and additional data analyses

6.2.1 Compression tests on Al foam samples

Many types of aluminum foams exhibit a compressive behavior similar to the idealized schematic curve proposed in 1997 by Ashby and Gibson [69, 71, 135], where first the stress rises linearly (elastic deformation), then a flat collapse plateau is observed as a result of perfect plasticity, which is finally followed by

a densification — an abrupt increase in the flow stress when the cell walls start to touch one another. In modern commercial closed-cell aluminum foams the plateau on the stress-strain curve is, however, caused by internal damage and localization of plastic deformation, resulting in discrete bands of collapsed cells [69, 71, 83, 128, 136, 137, 139, 140], as was also demonstrated in this work by the DIC analysis performed on MMS (syntactic) foam.

It was revealed in [69, 71, 72, 87, 137, 141, 142] and also confirmed in this work that, on the contrary, the compression curves of replicated aluminum foams are smooth and reproducible, and resemble metal-like hardening, with no plateau observed. By the DIC analysis, it was also confirmed that strain localization remains very limited, and the collapse bands are not observed. Strain concentrations, compared with average global deformation, are relatively low. There is in short a greater homogeneity in the compressive deformation of replicated pure aluminum foams than with commercial aluminum foams.

Three arguments have been proposed to explain such behavior [69, 72]:

1. The pore size is significantly smaller than in commercial metal foams – sample contains a great number of pores across the diameter, which is a very important condition for regular and highly reproducible behavior exempt of the size effect.

2. Aluminum and aluminum-magnesium are fairly ductile materials in comparison with composites or oxide-containing metals typically used for the production of commercial closed-cell Al foams. They also have a comparatively high rate of work hardening which stabilizes deformation.

3. Mesostructure does not contain large defects often found in commercial foams, such as highly oversized pores or broken and missing struts or cell walls.

It was also shown in this work that a precisely defined densification strain manifested as a steep increase in stress following the plateau is not present in salt-replicated foams. In [137], rather a different mechanism was discovered to be responsible for the gradual increase in work hardening, that is the strut impingement (in other words, new strut contacts created within the foam in the later stages of compression).

We have shown in Fig. 6.4 and 6.5 that the pore size exerts an influence on the flow stress of replicated pure Al foams, that is, as the pore size decreases, the flow stress of foam samples increases. This effect can be explained by a high density of dislocations initially present in the Al foam samples. These dislocations are introduced into the foam due to the mismatch in the thermal expansion coefficients

of aluminum and sodium chloride ($CTE_{\mathrm{Al}} = 2.36{\cdot}10^{-5}$ K^{-1} [143], $CTE_{\mathrm{NaCl}} = 4.05{\cdot}10^{-5}$ K^{-1} [144]). In this way, thermal phase strains develop during cooling, resulting in an emission of "thermal" dislocations. It was also evidenced that after annealing of foam samples at high temperature before testing, the plasticity size effect disappeared: dislocations that may have been introduced by the thermal expansion difference during the quenching of the metal/NaCl composite were in principle erased [69, 87]. The absence of the size effect in the flow stresses after annealing is expected if hardening is dislocational and thermal dislocations are indeed eliminated during the heat treatment, and also if dislocation multiplication during deformation is also size-independent. In the samples not subjected to the heat treatment, the thermal dislocations interfere with the movement and storage of dislocations generated to deform the metal ("multiplicative effect") [69].

This also shows that the size-dependence in the Al foam flow stress cannot be explained simply by an oxide layer formed on the free surfaces. This effect was, however, discovered to slightly affect the flow stresses as finer pore foams have larger free surface. However, the oxide layer along the metal free surfaces cannot bear a significant load, but rather it indirectly influences the processes of dislocation creation, motion, and blockage within the fine-scale foams [128]. Thus, the dislocational hardening of the matrix, linked with the generation of geometrically necessary dislocations with increasing density as the foam scales decrease, is understood to be the underlying mechanism of the plasticity size effect in salt-replicated foams.

To elucidate the dependence of plastic flow stress of Al metal foams on the intrinsic size of the pores, one must focus on the microprocesses that underlie the plastic deformation. When the size of pores or struts within the material becomes comparable with that of substructural features governing the plastic deformation of metals, such as the mean dislocation separation distance, the grain size, or the distance between precipitates, i.e. when the pore or strut diameter falls below a few micrometers, free surfaces start interfering with dislocation glide. This, in turn, alters the local flow stresses of the metal within the porous material [72, 87].

6.2.2 Compression tests on Al2Mg foam samples

In Al2Mg foam samples, the situation is quite different. Classical dislocational (Taylor) hardening is not the only operational mechanism in foams made of alloyed material and solid solution hardening is also present. Upon comparison of Fig. 6.4 with Fig. 6.8, it is clear that Al2Mg foam samples are stronger than Al ones. The strengthening effect of alloying is characteristic for aluminum and as well as for many other metals [145].

Another dissimilarity with the pure Al foams is that the plasticity size effect was not found in Al2Mg foam samples when the variations in volume fraction of solid V_s were taken into account. As discussed above, the plasticity size effect is dislocational in nature and can be identified when the Taylor hardening is operating. In these samples, a different hardening mechanism is active. Therefore, the absence of plasticity size effect should not be very surprising. However, the size effect was found in Al5Mg replicated foams [141]. The inconsistency in these results is not clear at this moment; yet, a different composition of metals making the foam in these studies may be of some significance, giving rise to different proportions of activity between the hardening mechanisms. Also the method for back-calculation of the deformation curves was somewhat different here.

An additional interesting feature of the Al2Mg foams is the presence of Portevin-Le Châtelier (PLC) effect observed as serrations on the stress-strain curves of Al2Mg400 and Al2Mg75 samples (Fig. 6.6). The occurrence of the PLC effect in Al5Mg foams was mentioned before in [141], however, no detailed explanation was given by the authors.

The PLC effect is characterized (in contrast to standard, "non-PLC" metals) by a negative strain rate sensitivity, i.e. in a displacement-driven test, the flow stress required for a given deformation speed increases as this deformation speed is decreased. Typically, the presence of PLC is corroborated by repeating the deformation experiments on additional samples at different strain rates. In the case of metal foams, however, this might be inconclusive as the foam structure is stochastic in nature and there are also variations (although only slight) in their relative density. For this reason, an additional experiment was proposed and carried out on a single sample where the strain rate was not kept constant but instead systematically changed in the course of compression. This type of experiment is deprived of intrinsic stochastic effects mentioned above.

The graph displaying results of this test is shown in Fig. 6.13. An initial strain rate of $10^{-3}\mathrm{s}^{-1}$ was gradually decreased in four steps to the strain rate as low as $2{\cdot}10^{-6}\mathrm{s}^{-1}$. It can be seen that the negative strain rate sensitivity is evident in Al2Mg400 since the flow stress rises with decreasing compression rate. Moreover, a transition from A-type PLC, to B- and finally C-type is also evidenced, which is another clear manifestation of the PLC effect (details on the PLC effect can be found in e.g. [109])[2].

[2]An identical test was performed also on Al400 foam sample (not shown here) in order to be sure that the negative strain rate sensitivity is not an artifact of the experimental device. Pure Al foam exhibited normal (positive) strain rate sensitivity, thus confirming the validity of the test on Al2Mg400 sample.

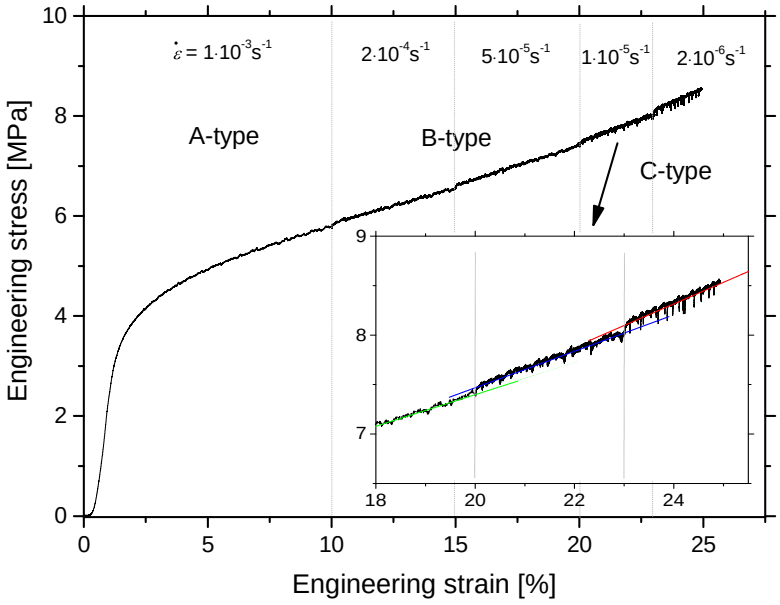

Figure 6.13: Occurrence of the PLC effect observed in Al2Mg400 foam sample.

The results presented in this section indicate that the situation is far more complicated in Al2Mg samples than in pure Al foams. This can be attributed to the fact that the deformation of Al2Mg foams is driven by three different and, in some sense, most likely competing mechanisms: work hardening, solid solution hardening, and the PLC effect.

6.2.3 Acoustic emission data

To cast more light on the results of mechanical tests, the AE data will be discussed in detail in the following sections.

It was shown that only the samples with a pore size of 400 µm produce intense AE in the course of the entire compression test (all the tests were carried out up to ∼30 % strain). Sample sets with a smaller pore size (150, 75, and 25 µm for Al foams; 75 and 25 µm for Al2Mg foams) exhibited a rapid decrease in the AE activity beyond the macroscopic yield point. Although these AE characteristics (in terms of counts and amplitudes) seem to be somewhat similar, small variations in the features could be distinguished between the Al and Al2Mg sample sets:

- the AE activity in the vicinity of the yield point is apparently more pronounced in Al foam samples with smaller pores,
- on the other hand, the scarce, intermittent AE signals with a relatively high amplitude are observed more frequently in Al2Mg smaller-pore samples.

It was discussed in the previous sections that the AE technique is particularly

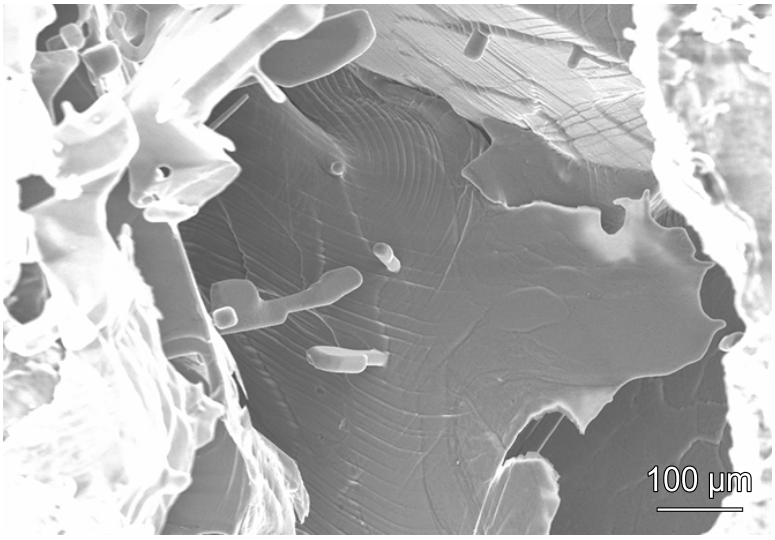

Figure 6.14: SEM micrograph showing slip steps found after the compression of Al400 foam sample. (Courtesy of P. Minárik)

sensitive to the collective motion of dislocation. To account for the vanishing of the AE signal as the pore size of Al and Al2Mg samples decrease, it is necessary to bring back the mechanism responsible for the plasticity size effect occurring in these materials. In addition to the intrinsic reduction in the mean free path of dislocations as the pore size decreases, the free surfaces exert image forces on the dislocations and reduce the effective shear stress required for dislocation motion [87, 146, 147]. This, in turn, results in a gradually poorer AE response in finer pore sample, notwithstanding that the AE in 400 µm pore size samples resembles rather a behavior of bulk material.

Solid solution magnesium atoms are known to have a strengthening effect on aluminum since they act as obstacles to the movement of dislocations [145]. On the other hand, the PLC effect is recognized to be a great source of acoustic signals (e.g. [96, 148–152]). These two mechanisms are coexistent in the Al2Mg samples and from the AE results it can be assumed that the solid solution hardening dominates in finer pore samples (compared with large pore Al2Mg400 samples). On the other hand, the Taylor hardening operating in Al samples allow for larger dislocation avalanches producing more powerful AE response at the beginning of compression. This assumption is fortified by a presence of slip bands along the struts in Al foams samples (observed in the SEM micrograph in Fig 6.14, and also before, in [34]), while such slip steps were almost absent in the Al2Mg foams.

Then, as the deformation proceeds further, high-amplitude signals appear more frequently in Al2Mg than in pure Al samples. This can be explained by a release of stresses concentrated at the sites occupied by Mg solid solution atoms as well as the presence of the PLC effect.

6.2.4 Advanced frequency analyses

Adaptive Sequential k-means (ASK) clustering analysis

ASK signal categorizing procedure was used to analyze deeply the raw AE signal in order to provide additional information on the mechanisms of plastic deformation. Details on the algorithm were presented above.

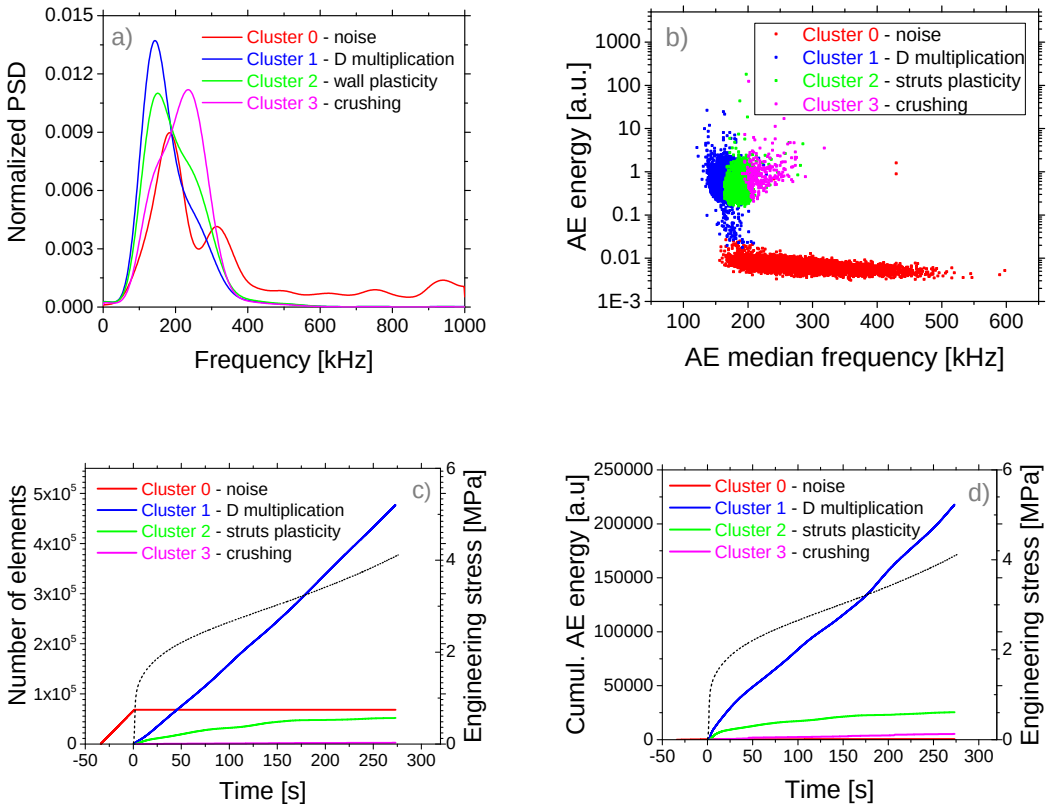

Figure 6.15: Sample Al400: a) "Mean" PSD functions corresponding to the clusters; b) Projection to the energy-median frequency space of the identified AE clusters; c) Time evolution of the cumulative number of elements in the clusters; d) Time evolution of the cumulative AE energy in the clusters.

In Fig. 6.15a-d, the fundamental outputs of the analysis performed on Al400 sample are presented. It was found that all AE signals naturally fall into four categories with mean PSD shapes (representing frequency distributions within individual clusters) shown in Fig. 6.15a. Projection of identified clusters to the energy-median frequency space is displayed in Fig. 6.15b. Fig. 6.15c and 6.15d represent time evolution[3] of two parameters of the individual clusters: cumulative

[3]It is worth noting here that given the dimensions of samples, an incidental advantage of constant cross-head speed of 0.02 mm·s^{-1} used for all the tests on metal foams in this work is that the strain value at a given time can be calculated simply by dividing a time value by 10 (e.g. 100 s = 10 % strain).

number of cluster elements and cumulative AE energy, respectively.

Source mechanisms can be now assigned to the clusters. The ASK analysis identified a cluster representing the noise and revealed three dominant deformation mechanisms, namely: dislocation multiplication, plastic deformation of struts, and the collapse of the foam structure (simply labeled as "crushing").

Cluster 0: *Noise*

The AE signal was always recorded several seconds before starting the compression test in order to identify the characteristics of the background noise exempt of "real" signals emitted from the sample during the test. Therefore, this cluster appears in the analyses first. There is a constant rise in the number of elements in the noise cluster at the beginning of the AE measurement before the deformation is started (see Fig. 6.15c); then, in the course of the test, this cluster remains inactive as the "real" signals dominate over the low-amplitude noise. The energy of the AE signals in this cluster is typically low, the frequency spectrum is relatively wide (Fig. 6.15a,b), and the signal has a continuous and constant character (Fig. 6.16). All these features have been reported as specific of the noise signal [131, 153].

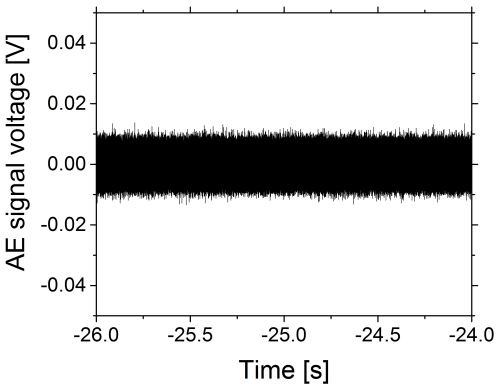

Figure 6.16: Noise sample recorded before the compression test on Al400 sample was launched.

Cluster 1: *Multiplication of dislocations*

The number of events in this cluster starts to increase at the beginning of compression, i.e. at low applied stresses (Fig. 6.17). Thermal dislocations stored within the samples as a result of the fabrication process start to interfere with the movement and storage of geometrically necessary dislocations generated to deform the metal. Microplasticity, as well as the massive movement and multiplication of dislocations, result in a high AE activity recorded at this stage, as was shown in many studies (e.g. [96]). Dislocation motion was reported to emit a low-frequency signal [131, 154, 155], that is in very good agreement with Fig. 6.15a,b.

Cluster 2: *Plastic deformation of struts*

Cluster 2 is formed shortly after the activation of Cluster 1 (this one being

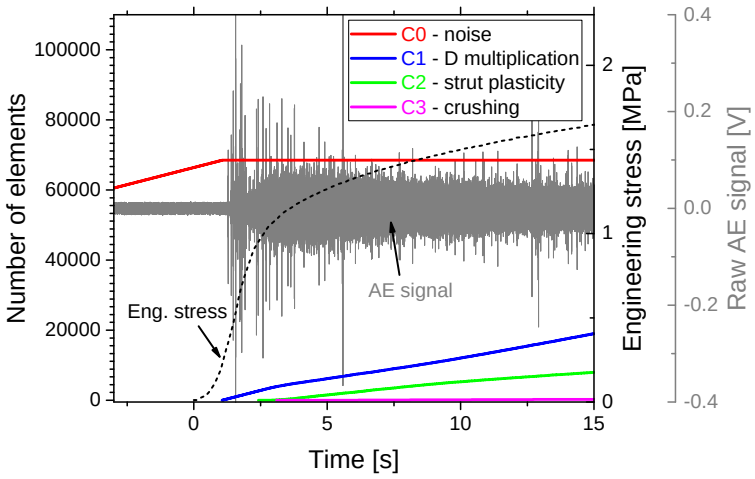

Figure 6.17: A detailed graph showing the evolution of raw AE signal and the activity of individual clusters at the very beginning of compression test.

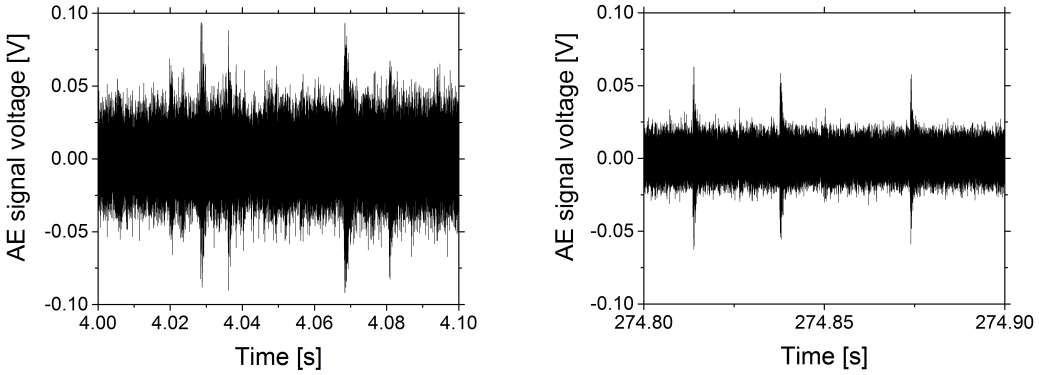

(a) Signal sample from an early stage of the compression of Al400 sample, showing an overlapping signals reflecting the collective dislocation motion.

(b) Signal sample from latter stage of the compression of Al400 sample, showing a sequence of burst signals originating in the collapse of foam structure.

Figure 6.18: Typical signals recorded during compression of Al400 foam sample.

still active) when the dislocation dynamics become more "stabilized". Characteristics of this cluster, in terms of frequency distributions, are very similar to the Cluster 1, although the spectrum is shifted to slightly higher frequencies. This is expected since the plastic deformation of foam struts is also governed by collective dislocation motion. The dislocation-type AE events usually consist of an array of overlapping signals [156]. The sample signal from the test on Al400 sample is shown in Fig. 6.18a.

Cluster 3: *Structure collapse (crushing)*

Somewhat wider frequency spectra representing the members of this cluster indicate that such AE signals originate in the collapse of structure making the foam [33]. The typical burst character of the AE signals observed in this stage is shown in Fig. 6.18b. At the same time, the characteristics of signals contributing to this cluster are in consonance with the observation of scarce signals in later stages of deformation in Fig. 6.11 and 6.12.

The situation in Al2Mg samples is seemingly very similar. In can be observed in Fig. 6.19 that almost identical four clusters were identified by the ASK algorithm, matching the results from sample Al400. Activity in the Cluster 0 assigned to the noise signals diminishes sharply with the onset of straining. Plasticity is represented by two clusters. First, the dislocation multiplication sets off, followed shortly by the formation of cluster assigned to the strut plasticity. Finally, the Cluster 3 representing foams structure collapse becomes active at higher strains. The presence of PLC effect in Al2Mg400 was not caught by this type of analysis since PLC is also a dislocation-driven process. Thereby, it is likely to be concealed within Cluster 2 representing plasticity of foam struts.

ASK analysis on Al and Al2Mg samples with smaller pore size was fairly consistent with the abovementioned results. Due to the related character of Cluster 1 and Cluster 2, the Cluster 2 was sometimes picked first by the algorithm; or these two clusters were actually not distinguished by the algorithm, and their contributions were merged together. These small inconsistencies can be probably attributed to the scarcity of tangible acoustic signals in the samples with smaller pore size. Otherwise, very similar features were found as in the case of sample Al400, as can be seen in Fig. 6.20 and Fig. 6.21 representing the data from ASK analysis on Al75 and Al2Mg75 samples, respectively. A somewhat more

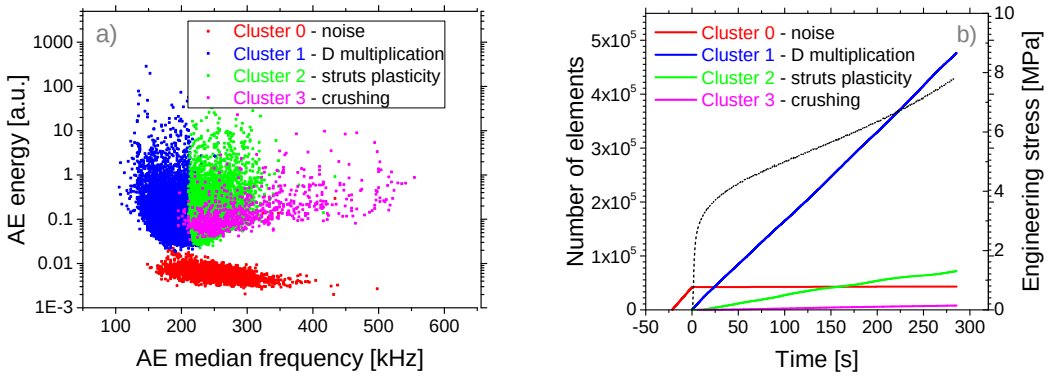

Figure 6.19: Sample Al2Mg400: a) Projection to the energy-median frequency space of the identified AE clusters. b) Time evolution of the cumulative number of elements in the clusters.

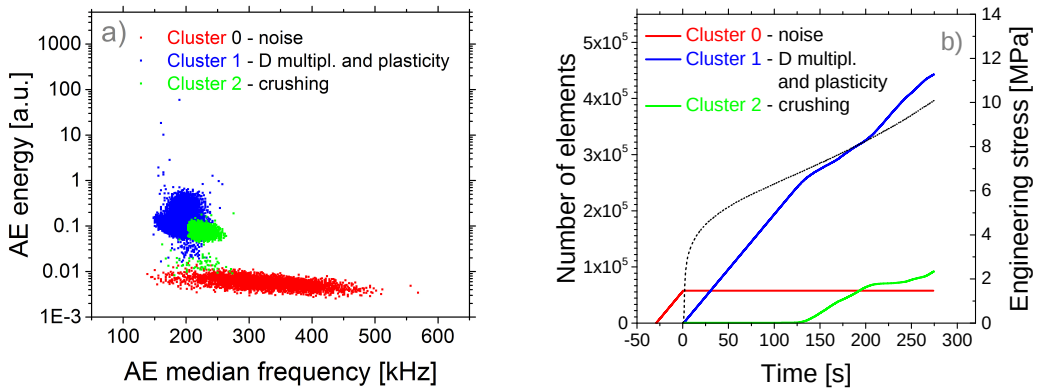

Figure 6.20: Sample Al75: a) Projection to the energy-median frequency space of the identified AE clusters. b) Time evolution of the cumulative number of elements in the clusters.

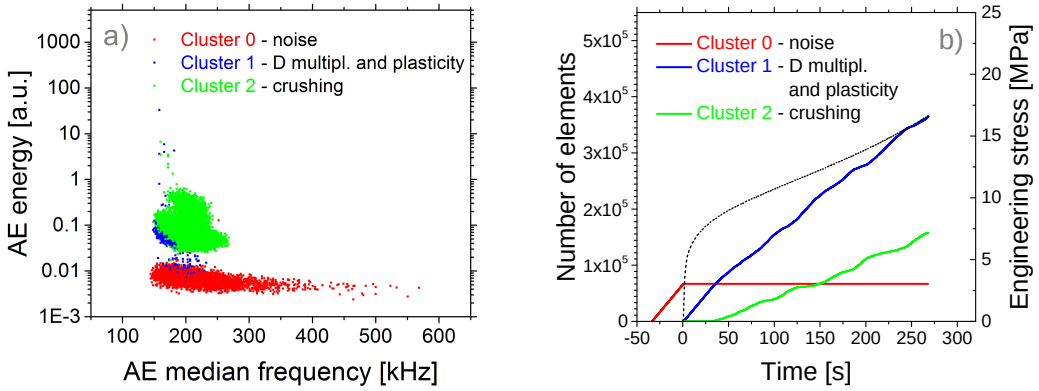

Figure 6.21: Sample Al2Mg75: a) Projection to the energy-median frequency space of the identified AE clusters. b) Time evolution of the cumulative number of elements in the clusters.

pronounced crushing (or collapse) of foam structure observed in the ASK results on finer pore samples is due to the higher volume fraction of solid, i.e. higher "density" of solid metal within the sample body, thus leaving less space for the plastic deformation of struts.

By inspecting additional parameters derived from the ASK analysis and zooming in on their evolution in early stages of deformation, further information can be obtained. In Fig. 6.22 the AE energy evolution is plotted in addition to the deformation curves and contributions of individual clusters.

In the very beginning of straining of both samples, the AE energy rapidly rises from its low-energy noise values, reaching its maximum in the vicinity of the

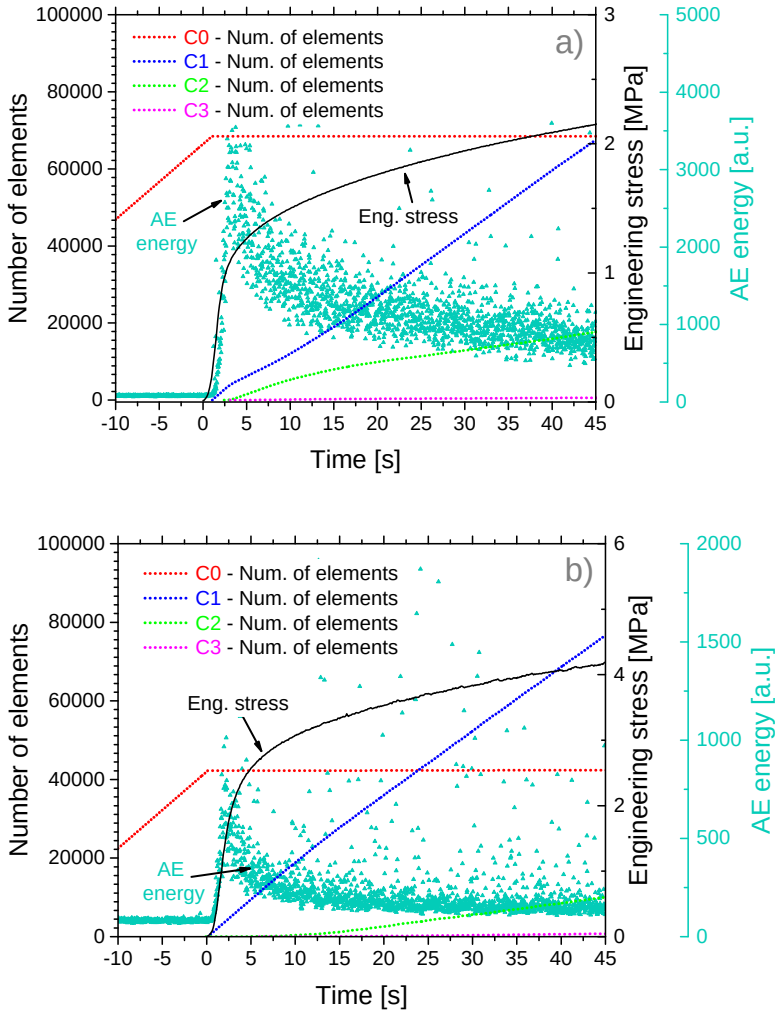

Figure 6.22: AE energy evolution in the early stage of compression of a) sample Al400 b) sample Al2Mg400.

macroscopic yield point. Then, it starts to decrease slowly. On the other hand, the evolution of AE median frequency presented in Fig. 6.23 follows somehow opposite trends: it steeply decreases (from its relatively high value in the wide-spectrum noise region) at the onset of compression; this stage is followed by a small increase, and finally a certain stabilization of its value takes place. It is known that high AE activity is usually accompanied by a decrease in the median frequency, as well as by an increase in the energy [109, 152] (as demonstrated also in Fig. 6.15). These observations thus support and are in line with trends in the basic AE parameters reported above: it can be clearly seen that the peak in AE activity found at the beginning of compression (Fig. 6.11 and 6.12) nicely correlates with the evolution of AE energy and AE median frequency shown in Fig. 6.22 and 6.23, respectively.

Furthermore, upon a detailed inspection, it can be discerned that both, the

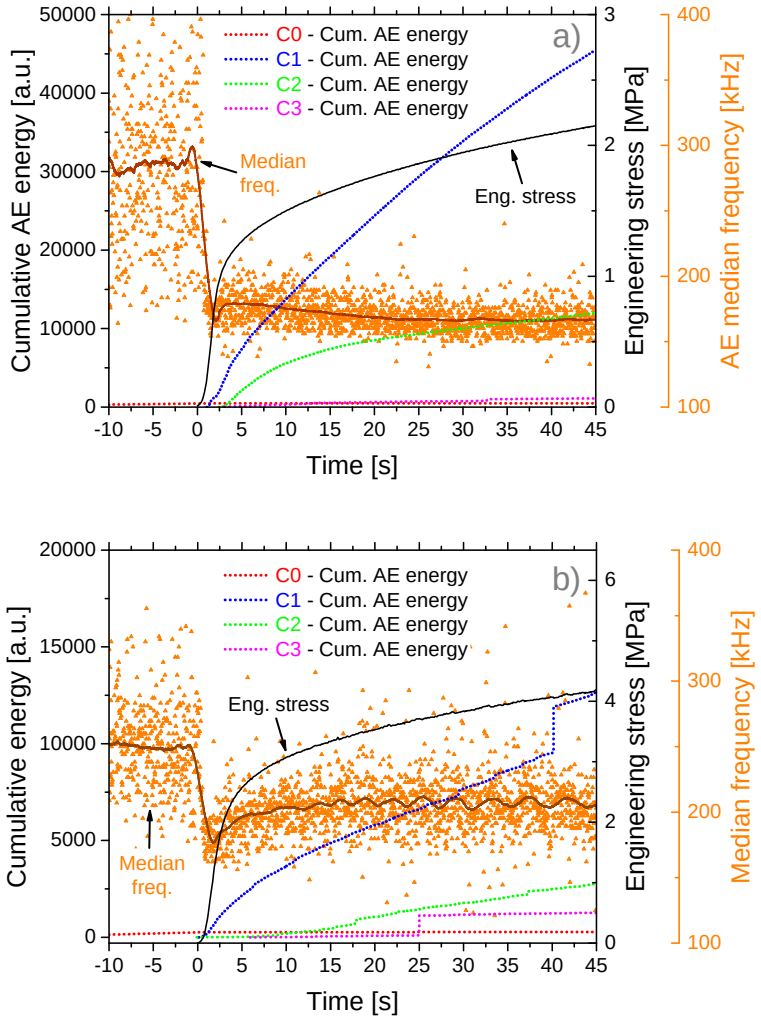

Figure 6.23: Median AE frequency evolution in the early stage of compression of a) sample Al400 b) sample Al2Mg400. To better demonstrate the evolution of this parameter, the scatter plot was smoothed using a Savitzky-Golay filter.

AE energy and the median frequency fluctuate somehow in the case of Al2Mg400. As shown in "zoomed" Fig. 6.24, the oscillations in median frequency are directly related to the PLC serrations on the deformation curve and very precise correlations can be seen. This observation agrees well with similar investigations on bulk Al5Mg samples [109, 152]; albeit, no straightforward correlations between the load drops and the AE energy were evidenced in this work. The reduction in median frequency is typically attributed to enhanced correlations in dislocation processes and strain localization [109, 157]. It is worth noting that the decrease in median frequency begins always before the actual stress drop, and thus can be considered as a predecessor of "catastrophic event", as was argued also in [109].

Another observation which advocates these conclusions is a short-time Fourier transform (STFT) analysis. Shown in Fig. 6.25 are the spectrograms calculated

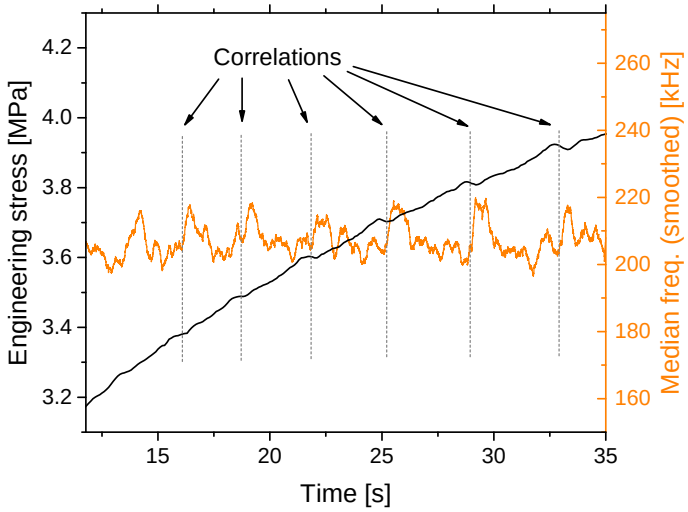

Figure 6.24: Time correlations between PLC serrations and median AE frequency found in the Al2Mg400 sample.

from the raw AE data recorded during compression of Al400 and Al2Mg400 samples. Qualitatively, the results are similar for the two samples; however, vertical higher-power stripes spanning wide frequency spectra can be identified in the spectrogram of Al2Mg400 sample. The stripes reflect an intermittent AE activity during the test and therefore this observation speaks again in favor of a relationship between the PLC effect and AE signal spectra. The time evolution of frequencies of the AE signal shown in the form of spectrograms is also, in terms of frequency evolution, in line with the results of ASK clustering analysis (even though the ASK diagrams does not have the capacity to identify the PLC effect).

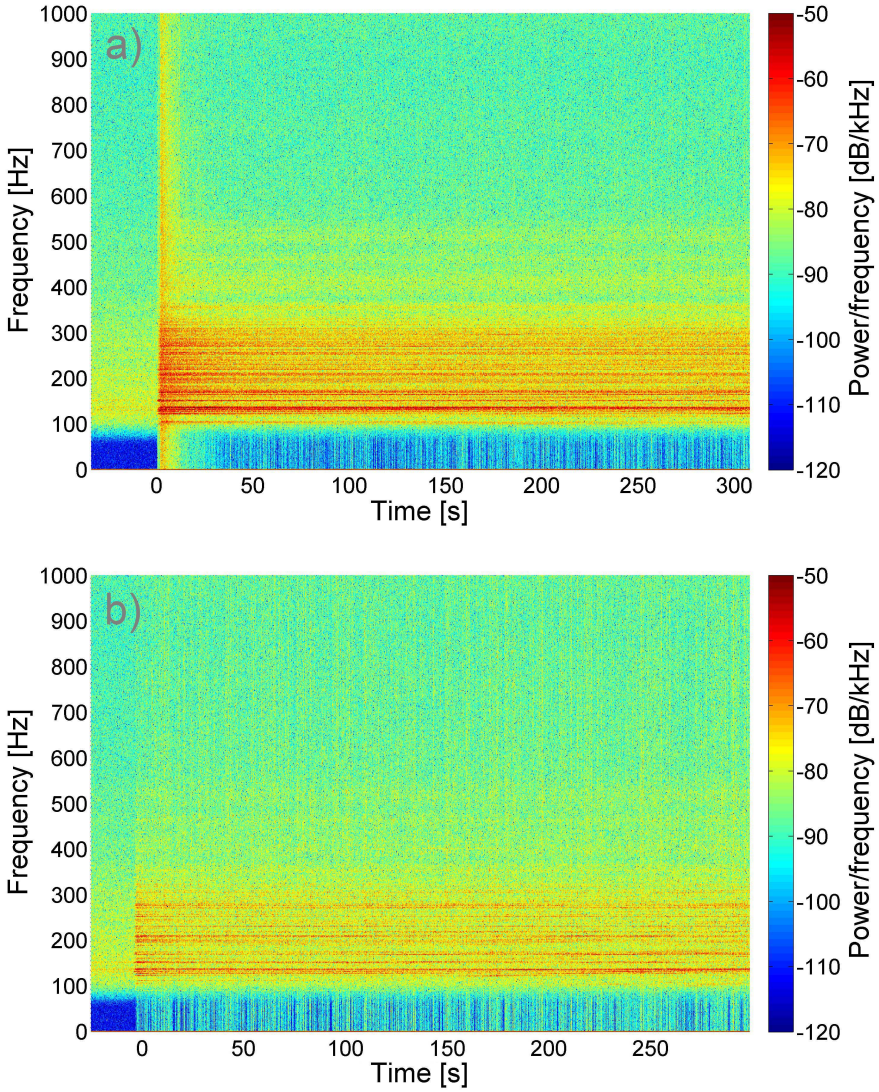

Figure 6.25: Spectrograms derived from the raw AE signals of a) Al400 and b) Al2Mg400 samples.

7. General discussion

It was presented in this thesis that the AE response can be recorded even at microscales, from samples having very small volumes. To accomplish this, very sensitive measurement devices have to be used and carefully set, since many factors may affect the success of recording the AE response. In addition, rather intricate procedures for the fabrication of microsamples are needed.

Mechanical tests coupled with the AE measurements carried out on microscopic samples, namely copper micropillars and aluminum microwires, presented in this thesis delivered several interesting results. First, the AE signals were recorded, for the first time, from microsamples in general. Although the acoustic signals were weak and relatively scarce, these tests helped to confirm directly that the deformation is realized by a collective movement of dislocations even at these scales. Specifically, the tests carried on the first set of micropillars (side length of 5 µm) show an evident relationship between the mechanical and AE response of the samples. The AE activity was much more pronounced in the softening stages of micropillar compression. Since AE is particularly sensitive to the collective dislocation dynamics, i.e. avalanches, it signifies that mutual dislocation activity in these stages is explicitly high.

Moreover, when finer experimental settings were employed for the experiments on the second set of micropillars and on the microwires, precise time-correlations were also found. AE signals were shown to correspond to the individual stress drops on the deformation curve. This testifies that not only is the AE generated during the longer periods of softening, but also it reflects an occurrence of individual, abrupt stress drops. Therefore, collective and rapid dislocation movement must take place to account for these stochastic drops when AE is recorded.

Three geometries of micropillars were indeed tested from this set (8 µm, 4 µm , and 2 µm in side length), and the size effect ("smaller is harder") was found in the flow stresses of these samples. Only larger pillars (side length 8 µm and 4 µm) were producing detectable AE during the compression, whereas the smallest pillars (2 µm) were dormant. The following explanation is proposed for this behavior: As the micropillar size decreases, the distance between dislocations becomes of the same scale as the specimen size and the plastic deformation starts to be carried by individual dislocations and exhaustion of dislocation sources takes place. This criterion might be fulfilled as the side length of the pillar decreases to 2 µm, limiting in this way also the collectiveness of dislocation activity, which in turn lead to diminishing AE. This is supported also by the existence of size effect in the mechanical properties, which strongly indicates a change in the de-

formation mechanism with decreasing micropillar size.

Since the salt-replicated foams are comprised of many struts (connected by nodes), the deformation is driven by collective deformation of single struts. Although the intermittent plasticity of individual struts is hidden within the collective response of a great number of struts making the macroscopic foam samples, the plasticity size effect is present in these samples and the flow stresses needed for the plastic deformation of finer foams were shown to be higher. This behavior is analogic to that of the microsamples. Similar trends in the AE response, such as those found in the microsamples, are also valid for the investigated foams: AE diminishes as the pore (as well as strut) size decreases. These findings emphasize the importance of mesostructure (or "architecture") of the foams and its key influence on the mechanical properties. Structural size scales govern the deformation processes and theories used to account for size (and other) effects observed in microsamples can be, at least partially, applied also to the microcellular porous metals.

A novel, intriguing result of this work is the presence of Portevin-Le Châtelier (PLC) effect in Al2Mg foams. The PLC effect is a plastic instability observed in dilute alloys, caused by interaction between dislocations and solute atoms (simply put, it is pinning and depinning of dislocations it the atmosphere of solute atoms). PLC is known to appear during mechanical testing of aluminum-magnesium (and many other) alloys as one of the very few cases when heterogeneity of plastic flow shows up at the macroscopic scale and requires collective behavior of large numbers of dislocations. In bulk samples, the effect consists of repetitive localization of plastic strain within transversal deformation bands. It is therefore intriguing, how the PLC effect can occur in an extremely complicated foams structure, where the dislocation depinning cannot simultaneously take place or be easily propagated across the sample. Yet, macroscopic serrations appear on the stress-strain curve and ask for an explanation. We propose that the sample can be a system in a critical state [158] and therefore the stress relaxation from the pilled-up pinned dislocations (i.e. the localized deformation) which takes place within individual strut results in an abrupt change in the local stresses in the neighbouring struts, thus causing a "chain reaction" of strain bursts in a considerable number of struts within the sample. One strut is not expected to produce visible serrations on the stress-strain curve, but collective relaxation in a large number of struts most likely will.

If the system is in a critical state, complex dynamics of such systems are manifested through a power-law relationship. In Fig. 7.1 are shown the complementary cumulative distribution functions (CCDF) of squared AE amplitudes (which were shown to be proportional to the energy released along with the occurrence

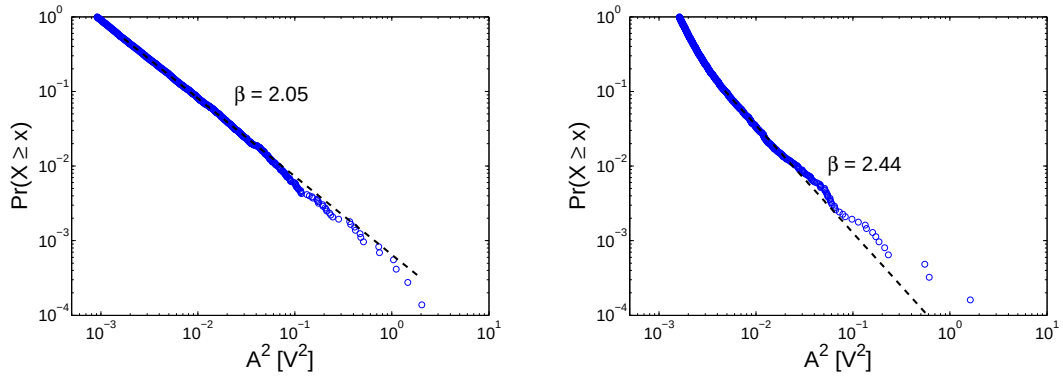

Figure 7.1: Complementary cumulative distribution functions of squared AE amplitudes. Left: sample Al2Mg400. Right: Al400 sample.

of the load drop [159]) of Al400 and Al2Mg400 samples (method adapted from [160]). Almost perfect power-law distribution is found in the case of Al2Mg400, suggesting that it meets the abovementioned criteria for criticality. On the other hand, the distribution in sample Al400 deviates somewhat from the power-law relation[1]. Consequently, the dislocation dynamics might be in this case different. In this way, the distributions of squared AE amplitudes also support the explanation of the PLC effect given above. Complete clarification of this effect, however, calls for further investigations.

[1]Such an analysis could not be performed on the foams with finer pores due to the scarcity of AE signals in those samples.

Conclusions and perspectives

Recently, a demand for microparts has increased significantly in many industries. Size effects in the mechanical properties of (sub)micron-scale materials have, therefore, become one of the central topics in materials science.

In this doctoral thesis, two types of materials were investigated:

1. Single-crystalline microsamples (in a form of copper micropillars with 2–8 µm side length and aluminum microwires with diameters of ∼100 µm),
2. Aluminum and aluminum containing 2 wt.% of magnesium (Al2Mg) salt-replicated microcellular metal foams (pore size of 25–400 µm).

Delicate experimental set-ups were developed and used to characterize the properties of the samples primarily in terms of compression and tensile test, and concurrent acoustic emission (AE) experiments (followed by an advanced signal analysis), whereby the AE was successfully applied at such small scales for the first time. The experiments have led to the following main results:

Microsamples:

- Improved focused ion beam (FIB) milling technique was presented for the fabrication of rectangular micropillars, resulting in faster preparation times and, presumably, reduced surface damage.
- Copper micropillars displayed a typical stochastic character of their mechanical properties, i.e. an intermittent plastic flow and variations in the flow stresses from sample to sample.
- Given the average deformation curves calculated from the data of several samples, the plasticity size effect was clearly identified in copper micropillars, therefore confirming the "smaller is harder" conjecture.
- The AE signals were found to be in good correlation with the features observed on the deformation curves: softer micropillars (and "softening stages" of compression in general) were, as a rule, accompanied by a strong AE activity, whereas the hardening stages generated only very weak AE signals. The AE response was shown to be also dependent on the micropillar size, as it was diminishing with decreasing micropillar dimensions. Since AE is sensitive only to collective movement of dislocation ensembles, this effect can be accounted for by recalling the explanation for the size effect at microscales, i.e. the transition from bulk-like deformation driven by massive dislocation interaction into a source-controlled regime where deformation is

carried rather by individual dislocations. In this way, the AE technique delivered a direct, in situ proof for the dislocation nature of the size effect.

- Moreover, it was discovered that the AE signals exhibit precise time correlations with the stress drops present on the deformation curves from both, copper micropillars tested in compression and aluminum microwires tested in tension. The statistical evaluation showed that, on average, the magnitude of evaluated AE parameters is larger if the signals originate from more massive stress drops, thereby indicating higher collectiveness of dislocation processes within such large drops.

Replicated Al and Al2Mg microcellular metal foams:

- Microcellular metal foams are, besides their other attractive properties, one of the very few materials where the size effects are (owing to the foam structure) discoverable also in bulk samples, and therefore can be tested by any conventional testing methods available for bulk materials.

- Salt-replication technique has proven to be a convenient method for the production of open-cell metal foams that differ in their mechanical properties from most other aluminum foams. Even though the individual struts may deform in an intermittent mode, the "overall" compression curves were shown to be smooth and reproducible. It was also confirmed by the DIC analysis that these foams have very low tendency to strain localization in comparison with commercial aluminum-based foams (e.g. syntactic MMC foams that were also partially analyzed in this work).

- The size effect was found in the plastic deformation of pure Al foams (the finer the pore size, the higher the flow stress if other parameters are kept constant). On the other hand, the Al2Mg foam samples do not exhibit the size effect, because, besides the Taylor hardening, the solid solution hardening and the Portevin-Le Châtelier (PLC) effect (observed as serrations on the stress-strain curves) are also operating in the alloyed aluminum.

- The AE response vanishes as the pore size becomes smaller in both types of foam material. In the case of pure Al foams, this can be explained by the change in deformation mechanism analogic to that observed in the copper micropillars. In Al2Mg foams, the explanation is not completely straightforward. We suggest that in addition to the Taylor hardening, solid solution atoms may also play an important role when the struts become smaller, thus hindering further the collective movement of dislocations.

- Advanced clustering evaluation of the AE signal revealed three stages of deformation in both types of foams: microplasticity and rapid multiplication of dislocations early during the compression, followed immediately by foam plasticity, and later by crushing (collapse of the structure).

- A novel and rather surprising observation of the PLC effect in the foam material with such a complicated structure was further supported by the AE signal spectra determined by the short time Fourier transform analysis as well as the median frequency evaluation (while the effect was concealed when only basic AE parameters were examined). We propose that the PLC effect in Al2Mg foams might be due to the "chain reaction" of PLC strain bursts within the foam material in a critical state, i.e. the stress relaxation within individual strut results in an abrupt change in the local stresses in the neighbouring struts, leading to almost simultaneous occurrence of strain bursts in a large number of struts within the sample.

Perspectives for future research

It was shown in this work that the AE technique exhibits a great potential as a new method applied in the field of mechanical properties research at microscales: it provides in-situ information about the underlying deformation dynamics in a non-destructive manner, at a great time resolution. There is an open space for its utilization and further development.

- Notwithstanding that the development of the presented methods themselves was rather challenging, they could be refined in the future, especially for the investigation of microsamples, as only the parameter-based AE analyses were effectively applied in this work for their characterization. Recording of the entire raw AE signals (streaming) would allow for complex signal examination as in the case of metal foams. In addition, options how to improve the sensitivity and/or to scale down the noise of the AE setup should be addressed in order to be able to collect a higher volume of relevant signals and to obtain, in turn, more robust statistics. Distributions of the AE event parameters could be of interest, in the first place, to explore in detail the notion of scale-free behavior (self-organized criticality) at microscales, as it was beyond the scope of this thesis. Such results could be then further tested by employing additional signal analysis methods, such as wavelet or multifractal analysis.

- Detailed inspection of the samples before and after the mechanical testing could be of concern, particularly by means of a microstructure characterization. Especially, the influence of initial dislocation density on the mechanical response is of high relevance at the microscale. It would be therefore interesting to determine and/or to be able to optimize the initial dislocation density. In this way, many different sets of microsamples could be prepared and tested with the help of AE, presumably shedding more light on the processes that lie behind the plasticity size effect.

- Occurrence of the PLC effect in Al2Mg foam specimens deserve further attention since its realization within the very complex foam structure is not perfectly clear at the moment. First of all, high-resolution 3D X-ray tomography and 3D digital image correlation have the ability to help to clarify this observation. Furthermore, foam parameters and experimental conditions (e.g. magnesium content, pore size or test temperature) can be varied systematically in order to confront these results with the well-documented results on the PLC effect in bulk aluminum alloys.

Bibliography

[1] J. P. Hirth and J. Lothe, *Theory of Dislocations*. Krieger Pub. Co., Virginia, 1992.

[2] M. D. Uchic, D. M. Dimiduk, J. N. Florando, and W. D. Nix, "Sample dimensions influence strength and crystal plasticity," *Science*, vol. 305, no. 5686, pp. 986–989, 2004.

[3] P. D. Ispánovity, Á. Hegyi, I. Groma, G. Györgyi, K. Ratter, and D. Weygand, "Average yielding and weakest link statistics in micron-scale plasticity," *Acta Materialia*, vol. 61, no. 16, pp. 6234–6245, 2013.

[4] D. M. Dimiduk, M. D. Uchic, and T. A. Parthasarathy, "Size-affected single-slip behavior of pure nickel microcrystals," *Acta Materialia*, vol. 53, no. 15, pp. 4065–4077, 2005.

[5] D. Kiener, C. Motz, T. Schöberl, M. Jenko, and G. Dehm, "Determination of mechanical properties of copper at the micron scale," *Advanced Engineering Materials*, vol. 8, no. 11, pp. 1119–1125, 2006.

[6] K. S. Ng and A. H. W. Ngan, "Stochastic nature of plasticity of aluminum micro-pillars," *Acta Materialia*, vol. 56, no. 8, pp. 1712–1720, 2008.

[7] S. Brinckmann, J.-Y. Kim, and J. R. Greer, "Fundamental differences in mechanical behavior between two types of crystals at the nanoscale," *Physical Review Letters*, vol. 100, p. 155502, 2008.

[8] M. D. Uchic and D. M. Dimiduk, "A methodology to investigate size scale effects in crystalline plasticity using uniaxial compression testing," *Materials Science and Engineering: A*, vol. 400-401, pp. 268–278, 2005.

[9] M. Zaiser, J. Schwerdtfeger, A. S. Schneider, C. P. Frick, B. G. Clark, P. A. Gruber, and E. Arzt, "Strain bursts in plastically deforming molybdenum micro- and nanopillars," *Philosophical Magazine*, vol. 88, no. 30-32, pp. 3861–3874, 2008.

[10] A. S. Schneider, D. Kaufmann, B. G. Clark, C. P. Frick, P. A. Gruber, R. Mönig, O. Kraft, and E. Arzt, "Correlation between critical temperature and strength of small-scale bcc pillars," *Phyical Review Letters*, vol. 103, p. 105501, 2009.

[11] J.-Y. Kim and J. R. Greer, "Size-dependent mechanical properties of molybdenum nanopillars," *Applied Physics Letters*, vol. 93, no. 10, p. 101916, 2008.

[12] E. M. Nadgorny, D. M. Dimiduk, and M. D. Uchic, "Size effects in LiF micron-scale single crystals of low dislocation density," in *Symposium EE – Size Effects in the Deformation of Materials – Experiments and Modeling*, vol. 976 of *MRS Proceedings*, pp. 0976–EE06–24, 2006.

[13] M. D. Uchic, P. A. Shade, and D. M. Dimiduk, "Plasticity of micrometer-scale single crystals in compression," *Annual Review of Materials Research*, vol. 39, pp. 361–386, 2009.

[14] O. Kraft, P. A. Gruber, R. Mönig, and D. Weygand, "Plasticity in confined dimensions," *Annual Review of Materials Research*, vol. 40, pp. 293–317, 2010.

[15] J. R. Greer and J. T. M. De Hosson, "Plasticity in small-sized metallic systems: Intrinsic versus extrinsic size effect," *Progress in Materials Science*, vol. 56, no. 6, pp. 654–724, 2011.

[16] C. A. Volkert, A. Donohue, and F. Spaepen, "Effect of sample size on deformation in amorphous metals," *Journal of Applied Physics*, vol. 103, no. 8, pp. 1–6, 2008.

[17] H. Bei, S. Shim, E. George, M. Miller, E. Herbert, and G. Pharr, "Compressive strengths of molybdenum alloy micro-pillars prepared using a new technique," *Scripta Materialia*, vol. 57, no. 5, pp. 397–400, 2007.

[18] F. Mompiou, M. Legros, A. Sedlmayr, D. S. Gianola, D. Caillard, and O. Kraft, "Source-based strengthening of sub-micrometer Al fibers," *Acta Materialia*, vol. 60, no. 3, pp. 977–983, 2012.

[19] A. T. Jennings and J. R. Greer, "Tensile deformation of electroplated copper nanopillars," *Philosophical Magazine*, vol. 91, pp. 1108–1120, 2011.

[20] C. Yang, B. S. Li, M. X. Ren, and H. Z. Fu, "Studies of microstructures made of Zn–Al alloys using microcasting," *The International Journal of Advanced Manufacturing Technology*, vol. 46, no. 1, pp. 173–178, 2010.

[21] G. Baumeister, B. Okolo, J. Rögner, R. Ruprecht, E. Kerscher, V. Schulze, J. Haußelt, and D. Löhe, "New results on microcasting of Al bronze," *Microsystem Technologies*, vol. 14, no. 12, pp. 1813–1821, 2008.

[22] J. Rögner, K.-H. Lang, G. Baumeister, and V. Schulze, "Microstructure and mechanical properties of micro tensile specimens made of CuAl10Ni5Fe4 produced by micro casting," *Microsystem Technologies*, vol. 17, no. 2, pp. 301–311, 2011.

[23] J. Krebs, *Cast aluminium microwires: processing and plastic deformation.* PhD thesis, 2015. École polytechnique fédérale de Lausanne, Switzerland.

[24] J. R. Greer and W. D. Nix, "Nanoscale gold pillars strengthened through dislocation starvation," *Physical Review B*, vol. 73, p. 245410, 2006.

[25] M.-C. Miguel, A. Vespignani, S. Zapperi, J. Weiss, and J.-R. Grasso, "Intermittent dislocation flow in viscoplastic deformation," *Nature*, vol. 410, no. 6829, pp. 667–671, 2001.

[26] D. M. Dimiduk, C. Woodward, R. LeSar, and M. D. Uchic, "Scale-free intermittent flow in crystal plasticity," *Science*, vol. 312, no. 5777, pp. 1188–1190, 2006.

[27] F. F. Csikor, C. Motz, D. Weygand, M. Zaiser, and S. Zapperi, "Dislocation avalanches, strain bursts, and the problem of plastic forming at the micrometer scale," *Science*, vol. 318, no. 5848, pp. 251–254, 2007.

[28] N. Yazdi, F. Ayazi, and K. Najafi, "Micromachined inertial sensors," *Proceedings of the IEEE*, vol. 86, no. 8, pp. 1640–1659, 1998.

[29] N. V. Lavrik, M. J. Sepaniak, and P. G. Datskos, "Cantilever transducers as a platform for chemical and biological sensors," *Review of scientific instruments*, vol. 75, no. 7, pp. 2229–2253, 2004.

[30] J. Weiss and D. Marsan, "Three-dimensional mapping of dislocation avalanches: Clustering and space/time coupling," *Science*, vol. 299, no. 5603, pp. 89–92, 2003.

[31] J. Weiss, F. Lahaie, and J. R. Grasso, "Statistical analysis of dislocation dynamics during viscoplastic deformation from acoustic emission," *Journal of Geophysical Research: Solid Earth*, vol. 105, no. B1, pp. 433–442, 2000.

[32] Cs. Kádár, F. Chmelík, M. Cieslar, and J. Lendvai, "Acoustic emission of salt-replicated foams during compression," *Scripta Materialia*, vol. 59, no. 9, pp. 987–990, 2008.

[33] Cs. Kádár, K. Máthis, I. N. Orbulov, and F. Chmelík, "Monitoring the failure mechanisms in metal matrix syntactic foams during compression by acoustic emission," *Materials Letters*, vol. 173, pp. 31–34, 2016.

[34] M. Knapek, P. Dobroň, F. Chmelík, M. Zimina, J. Pešička, E. Combaz, and A. Mortensen, "Deformation of open-cell microcellular pure aluminum investigated by the acoustic emission technique," in *Light Metals 2014* (J. Granfield, ed.), pp. 337–342, John Wiley & Sons, Inc., San Diego, USA, 2014.

[35] Cs. Kádár, F. Chmelík, Z. Rajkovits, and J. Lendvai, "Acoustic emission measurements on metal foams," *Journal of Alloys and Compounds*, vol. 378, no. 1-2, pp. 145–150, 2004.

[36] A. H. Brothers, D. W. Prine, and D. C. Dunand, "Acoustic emissions analysis of damage in amorphous and crystalline metal foams," *Intermetallics*, vol. 14, no. 8–9, pp. 857–865, 2006.

[37] M. E. Cox and D. C. Dunand, "Acoustic emission analysis of damage during compressive deformation of amorphous Zr-based foams with aligned, elongated pores," *Metallurgical and Materials Transactions A*, vol. 44, no. 7, pp. 3114–3122, 2013.

[38] R. W. K. Honeycombe, *The plastic deformation of metals*. American Society for Metals, Ohio, 2nd ed., 1984.

[39] E. Schmid and W. Boas, *Plasticity of Crystals with Special Reference to Metals*. Hughes & Co., London, 1950.

[40] "Deformation of single crystals." `http://academic.uprm.edu/pcaceres/Courses/MechMet/`. Accessed: 2016-06-10.

[41] N. F. Mott, "A theory of work-hardening of metal crystals," *Philosophical Magazine*, vol. 43, pp. 1151–1178, 1952.

[42] S. Mader, "Elektronenmikroskopische Untersuchung der Gleitlinienbildung auf Kupfereinkristallen," *Zeitschrift für Physik*, vol. 149, pp. 73–102, 1957.

[43] L. M. Clarebrough and M. E. Hargreaves, "Work hardening of metals," *Progress in Metal Physics*, vol. 8, pp. 1–103, 1959.

[44] S. J. Basinski and Z. S. Basinski, "Plastic deformation and work hardening," in *Dislocations in Solid* (F. R. N. Nabarro, ed.), pp. 261–362, Amsterdam, 1979.

[45] H. Fujita, "Continuous observation of dynamic behaviors of dislocations in aluminum," *Journal of the Physical Society of Japan*, vol. 23, no. 6, pp. 1349–1361, 1967.

[46] G. F. Taylor, "A method of drawing metallic filaments and a discussion of their properties and uses," *Physical Review*, vol. 23, pp. 655–660, 1924.

[47] S. S. Brenner, "Tensile strength of whiskers," *Journal of Applied Physics*, vol. 27, no. 12, pp. 1484–1491, 1956.

[48] S. S. Brenner, "Plastic deformation of copper and silver whiskers," *Journal of Applied Physics*, vol. 28, no. 9, pp. 1023–1026, 1957.

[49] K. Yoshida, M. Yamamoto, Y. Gotoh, and T. Onozuka, "Plastic deformation of copper and iron whiskers," *Transactions of the Japan Institute of Metals*, vol. 9, pp. 863–&, 1958.

[50] K. Sieradzki, A. Rinaldi, C. Friesen, and P. Peralta, "Length scales in crystal plasticity," *Acta Materialia*, vol. 54, no. 17, pp. 4533–4538, 2006.

[51] R. Dou and B. Derby, "A universal scaling law for the strength of metal micropillars and nanowires," *Scripta Materialia*, vol. 61, no. 5, pp. 524–527, 2009.

[52] P. S. Phani, K. Johanns, G. Duscher, A. Gali, E. George, and G. Pharr, "Scanning transmission electron microscope observations of defects in as-grown and pre-strained Mo alloy fibers," *Acta Materialia*, vol. 59, no. 5, pp. 2172–2179, 2011.

[53] J. Zimmermann, S. van Petegem, H. Bei, D. Grolimund, E. George, and H. van Swygenhoven, "Effects of focused ion beam milling and pre-straining on the microstructure of directionally solidified molybdenum pillars: A Laue diffraction analysis," *Scripta Materialia*, vol. 62, no. 10, pp. 746–749, 2010.

[54] H. Bei, S. Shim, G. Pharr, and E. George, "Effects of pre-strain on the compressive stress–strain response of Mo-alloy single-crystal micropillars," *Acta Materialia*, vol. 56, no. 17, pp. 4762–4770, 2008.

[55] M. D. Uchic, P. A. Shade, and D. M. Dimiduk, "Micro-compression testing of FCC metals: A selected overview of experiments and simulations," *Journal of the Minerals Metals & Materials Society*, vol. 61, no. 3, pp. 36–41, 2009.

[56] D. Kiener, C. Motz, M. Rester, M. Jenko, and G. Dehm, "FIB damage of Cu and possible consequences for miniaturized mechanical tests," *Materials Science and Engineering: A*, no. 1-2, pp. 262–272, 2007.

[57] R. Gu and A. Ngan, "Effects of pre-straining and coating on plastic deformation of aluminum micropillars," *Acta Materialia*, vol. 60, no. 17, pp. 6102–6111, 2012.

[58] A. Schneider, D. Kiener, C. Yakacki, H. Maier, P. Gruber, N. Tamura, M. Kunz, A. Minor, and C. Frick, "Influence of bulk pre-straining on the size effect in nickel compression pillars," *Materials Science and Engineering: A*, vol. 559, pp. 147–158, 2013.

[59] D. Kiener and A. M. Minor, "Source truncation and exhaustion: Insights from quantitative in situ TEM tensile testing," *Nano Letters*, vol. 11, no. 9, pp. 3816–3820, 2011.

[60] C. A. Volkert and E. T. Lilleodden, "Size effects in the deformation of sub-micron Au columns," *Philosophical Magazine*, vol. 86, no. 33-35, pp. 5567–5579, 2006.

[61] J. R. Greer, "Bridging the gap between computational and experimental length scales: a review on nano-scale plasticity," *Reviews on advanced materials science*, vol. 13, no. 1, pp. 59–70, 2006.

[62] T. A. Parthasarathy, S. I. Rao, D. M. Dimiduk, M. D. Uchic, and D. R. Trinkle, "Contribution to size effect of yield strength from the stochastics of dislocation source lengths in finite samples," *Scripta Materialia*, vol. 56, no. 4, pp. 313–316, 2007.

[63] D. Norfleet, D. Dimiduk, S. Polasik, M. Uchic, and M. Mills, "Dislocation structures and their relationship to strength in deformed nickel microcrystals," *Acta Materialia*, vol. 56, no. 13, pp. 2988–3001, 2008.

[64] S. Rao, D. Dimiduk, T. Parthasarathy, M. Uchic, M. Tang, and C. Woodward, "Athermal mechanisms of size-dependent crystal flow gleaned from three-dimensional discrete dislocation simulations," *Acta Materialia*, vol. 56, no. 13, pp. 3245–3259, 2008.

[65] S. I. Rao, D. M. Dimiduk, M. Tang, T. A. Parthasarathy, M. D. Uchic, and C. Woodward, "Estimating the strength of single-ended dislocation sources in micron-sized single crystals," *Philosophical Magazine*, vol. 87, pp. 4777–4794, 2007.

[66] K. S. Ng and A. H. W. Ngan, "Breakdown of Schmid's law in micropillars," *Scripta Materialia*, vol. 59, no. 7, pp. 796–799, 2008.

[67] J. A. El-Awady, M. Wen, and N. M. Ghoniem, "The role of the weakest-link mechanism in controlling the plasticity of micropillars," *Journal of the Mechanics and Physics of Solids*, vol. 57, no. 1, pp. 32–50, 2009.

[68] D. Kiener, M. Rester, S. Scheriau, B. Yang, R. Pippan, and G. Dehm, "Influence of external and internal length scale of the flow stress of copper," *International Journal of Materials Research*, vol. 98, no. 11, pp. 1047–1053, 2007.

[69] J. F. Despois, *Replicated aluminium foam: Processing and properties*. PhD thesis, 2005. École polytechnique fédérale de Lausanne, Switzerland.

[70] A. Kennedy, "Porous metals and metal foams made from powders," in *Powder Metallurgy* (K. Kondoh, ed.), pp. 31–46, InTech, Nottingham, 2012.

[71] M. F. Ashby, A. Evans, N. A. Fleck, L. J. Gibson, J. W. Hutchinson, and H. N. Wadley, "Metal foams: a design guide," *Materials & Design*, vol. 23, no. 1, 2002.

[72] R. Goodall and A. Mortensen, "Porous metals," in *Physical Metallurgy, 5th ed., vol. 7* (D. Laughlin and H. K., eds.), pp. 2399–2595, Elsevier, Amsterdam, 2014.

[73] J. Banhart, "Manufacture, characterisation and application of cellular metals and metal foams," *Progress in Materials Science*, vol. 46, no. 6, pp. 559–632, 2001.

[74] H.-P. Degischer and B. Kriszt, eds., *Handbook of Cellular Metals*. Wiley-VCH Verlag GmbH & Co. KGaA, Weinheim, 2002.

[75] G. J. Davies and S. Zhen, "Metallic foams: their production, properties and applications," *Journal of Materials Science*, vol. 18, no. 7, pp. 1899–1911, 1983.

[76] H. Nakajima, "Fabrication, properties and application of porous metals with directional pores," *Progress in Materials Science*, vol. 52, no. 7, pp. 1091–1173, 2007.

[77] V. Shapovalov, "Porous metals," *MRS Bulletin*, vol. 19, pp. 24–28, 1994.

[78] J. Banhart, "Manufacturing routes for metallic foams," *Journal of the Minerals Metals & Materials Society*, vol. 52, no. 12, pp. 22–27, 2000.

[79] J. Banhart, "Metal foams: Production and stability," *Advanced Engineering Materials*, vol. 8, no. 9, pp. 781–794, 2006.

[80] Y. Conde, J.-F. Despois, R. Goodall, A. Marmottant, L. Salvo, C. San Marchi, and A. Mortensen, "Replication processing of highly porous materials," *Advanced Engineering Materials*, vol. 8, no. 9, pp. 795–803, 2006.

[81] A. D. Smigelskas and E. O. Kirkendall, "Zinc diffusion in alpha-brass," *Transactions of the Metallurgical Society of AIME*, pp. 130–142, 1947.

[82] R. M. Brick, A. W. Pense, and R. B. Gordon, *Structure and properties of engineering materials*. McGraw-Hill, Michigan, 4th ed., 1977.

[83] A.-F. Bastawros, H. Bart-Smith, and A. G. Evans, "Experimental analysis of deformation mechanisms in a closed-cell aluminum alloy foam," *Journal of the Mechanics and Physics of Solids*, vol. 48, no. 2, pp. 301–322, 2000.

[84] E. W. Andrews, G. Gioux, P. Onck, and L. J. Gibson, "Size effects in ductile cellular solids. Part II: Experimental results," *International Journal of Mechanical Sciences*, vol. 43, no. 3, pp. 701–713, 2001.

[85] Y. Chino, M. Mabuchi, Y. Yamada, S. Hagiwara, and H. Iwasaki, "An experimental investigation of effects of specimen size parameters on compressive and tensile properties in a closed cell Al foam," *Materials transactions*, vol. 44, no. 4, pp. 633–636, 2003.

[86] M. Idris, T. Vodenitcharova, and M. Hoffman, "Mechanical behaviour and energy absorption of closed-cell aluminium foam panels in uniaxial compression," *Materials Science and Engineering: A*, vol. 517, no. 1–2, pp. 37–45, 2009.

[87] R. Goodall, J. F. Despois, and A. Mortensen, "The plasticity size effect in replicated microcellular aluminium," *Scripta Materialia*, vol. 69, no. 6, pp. 469–472, 2013.

[88] G. Dehm, "Miniaturized single-crystalline fcc metals deformed in tension: New insights in size-dependent plasticity," *Progress in Materials Science*, vol. 54, no. 6, pp. 664–688, 2009.

[89] J.-F. Despois, Y. Conde, C. Marchi, and A. Mortensen, "Tensile behavior of replicated aluminium foams," *Advanced Engineering Materials*, vol. 6, no. 6, pp. 444–447, 2004.

[90] R. Goodall, J.-F. Despois, A. Marmottant, L. Salvo, and A. Mortensen, "The effect of preform processing on replicated aluminium foam structure and mechanical properties," *Scripta Materialia*, vol. 54, no. 12, pp. 2069–2073, 2006.

[91] R. Goodall, A. Marmottant, L. Salvo, and A. Mortensen, "Spherical pore replicated microcellular aluminium: Processing and influence on properties," *Materials Science and Engineering: A*, vol. 465, no. 1-2, pp. 124–135, 2007.

[92] A. M. Hodge, J. R. Hayes, J. A. Caro, J. Biener, and A. V. Hamza, "Characterization and mechanical behavior of nanoporous gold," *Advanced Engineering Materials*, vol. 8, no. 9, pp. 853–857, 2006.

[93] D. Lee, X. Wei, X. Chen, M. Zhao, S. Jun, J. Hone, E. G. Herbert, W. C. Oliver, and J. W. Kysar, "Microfabrication and mechanical properties of nanoporous gold at the nanoscale," *Scripta Materialia*, vol. 56, no. 5, pp. 437–440, 2007.

[94] C. A. Volkert, E. T. Lilleodden, D. Kramer, and J. Weissmüller, "Approaching the theoretical strength in nanoporous Au," *Applied Physics Letters*, vol. 89, no. 6, pp. 061920–1–3, 2006.

[95] J. Biener, A. M. Hodge, J. R. Hayes, C. A. Volkert, L. A. Zepeda-Ruiz, A. V. Hamza, and F. F. Abraham, "Size effects on the mechanical behavior of nanoporous Au," *Nano Letters*, vol. 6, pp. 2379–2382, 2006.

[96] C. R. Heiple and S. H. Carpenter, "Acoustic emission produced by deformation of metals and alloys - A review, part I and II," *Journal of Acoustic Emission*, vol. 6, pp. 177–204, 215–237, 1987.

[97] H. Vallen, "AE testing fundamentals, equipment, applications," *NDTnet*, vol. 43, no. 3, 2002.

[98] A. A. Pollock, "Acoustic emission inspection," in *ASM Handbook Vol. 17, Nondestructive Evaluation and Quality Control*, pp. 278–294, 1989.

[99] K. Illková, *Influence of Solid Solution Elements and Precipitate Formation on the Mechanical Behaviour of Magnesium Alloys.* PhD thesis, 2013. Charles University in Prague, Czech republic.

[100] "Acoustic emission technology." `http://www.physicalacoustics.com/ae-technology`. Accessed: 2016-05-30.

[101] V. D. Natsik and K. A. Chishko, "Emission of sound from dislocations moving near the surface of a crystal," *Fizika Tverdogo Tela*, vol. 20, no. 2, pp. 457–465, 1978.

[102] C. B. Scruby, H. N. G. Wadley, and J. E. Sinclair, "The origin of acoustic-emission during deformation of aluminum and an aluminum-magnesium alloy," *Philosophical Magazine A*, vol. 44, no. 2, pp. 249–274, 1981.

[103] C. B. Scruby, H. N. G. Wadley, K. Rushbridge, and D. Stockham-Jones, "Influence of microstructure on acoustic-emission during deformation of aluminum alloy," *Metal Science*, vol. 15, no. 11-1, pp. 599–608, 1981.

[104] S. H. Carpenter, "Acoustic emission from plastic deformation." `http://lib.dr.iastate.edu/qnde/1975/allpapers/41/`, 1975. Accessed: 2016-06-18.

[105] M. Kaphle, *Analysis of acoustic emission data for accurate damage assessment for structural health monitoring applications.* PhD thesis, 2012. Queensland University of Technology, Australia.

[106] J. Kaiser, "Erkenntnisse und Folgerungen aus der Messung von Geräuschen bei Zugbeanspruchung von Metallischen Werkstoffen," *Archiv für das Eisenhüttenwesen*, vol. 24, no. 1-2, pp. 43–45, 1953.

[107] P. P. Gillis and M. A. Hamstad, "Some fundamental aspects of the theory of acoustic emission," *Materials Science and Engineering*, vol. 14, no. 2, pp. 103–108, 1974.

[108] J. Weiss, T. Richeton, F. Louchet, F. Chmelík, P. Dobroň, D. Entemeyer, M. Lebyodkin, T. Lebedkina, C. Fressengeas, and R. J. McDonald, "Evidence for universal intermittent crystal plasticity from acoustic emission and high-resolution extensometry experiments," *Physical Review B*, vol. 76, no. 22, p. 224110, 2007.

[109] I. Shashkov, *Multiscale study of the intermittency of plastic deformation by acoustic emission method*. PhD thesis, 2012. Université de Lorraine, Metz, France.

[110] K. Máthis and F. Chmelík, "Exploring plastic deformation of metallic materials by the acoustic emission technique," in *Acoustic Emission* (S. Wojciech, ed.), pp. 23–48, InTech, Rijeka, 2012.

[111] M. Huang, L. Jiang, P. K. Liaw, C. R. Brooks, R. Seeley, and D. L. Klarstrom, "Using acoustic emission in fatigue and fracture materials research," *The Member Jounal of The Minerals, Metals & Materials Society*, vol. 50, no. 11, 1998.

[112] J. Weiss and J.-R. Grasso, "Acoustic emission in single crystals of ice," *The Journal of Physical Chemistry B*, vol. 101, no. 32, pp. 6113–6117, 1997.

[113] J. W. Cooley and J. W. Tukey, "An algorithm for the machine calculation of complex fourier series," *Mathematics of Computation*, vol. 19, pp. 297–301, 1965.

[114] A. Vinogradov, "Principles of statistical and spectral analysis of acoustic and their application to plastic deformation of metallic glasses," *Journal of Acoustic Emission*, vol. 16, pp. 158–169, 1998.

[115] S. Reyntjens and R. Puers, "A review of focused ion beam applications in microsystem technology," *Journal of Micromechanics and Microengineering*, vol. 11, no. 4, p. 287, 2001.

[116] A. T. Jennings, M. J. Burek, and J. R. Greer, "Microstructure versus size: Mechanical properties of electroplated single crystalline Cu nanopillars," *Physical review letters*, vol. 104, no. 13, p. 135503, 2010.

[117] M. J. Burek and J. R. Greer, "Fabrication and microstructure control of nanoscale mechanical testing specimens via electron beam lithography and electroplating," *Nano letters*, vol. 10, no. 1, pp. 69–76, 2009.

[118] G. Moser, H. Felber, B. Rashkova, P. Imrich, C. Kirchlechner, W. Grosinger, C. Motz, G. Dehm, and D. Kiener, "Sample preparation by metallography and focused ion beam for nanomechanical testing," *Practical Metallography*, vol. 49, no. 6, pp. 343–355, 2012.

[119] J. Hütsch and E. T. Lilleodden, "The influence of focused-ion beam preparation technique on microcompression investigations: Lathe vs. annular milling," *Scripta Materialia*, vol. 77, pp. 49–51, 2014.

[120] S. Wurster, R. Treml, R. Fritz, M. Kapp, E. Langs, M. Alfreider, C. Ruhs, P. Imrich, G. Felber, and D. Kiener, "Novel methods for the site specific preparation of micromechanical structures," *Practical Metallography*, vol. 52, no. 3, pp. 131–146, 2015.

[121] J. Li, T. Malis, and S. Dionne, "Recent advances in FIB–TEM specimen preparation techniques," *Materials characterization*, vol. 57, no. 1, pp. 64–70, 2006.

[122] T. Ishitani, K. Umemura, T. Ohnishi, T. Yaguchi, and T. Kamino, "Improvements in performance of focused ion beam cross-sectioning: Aspects of ion-sample interaction," *Journal of electron microscopy*, vol. 53, no. 5, pp. 443–449, 2004.

[123] J. R. Greer, H. Espinosa, K. Ramesh, and E. Nadgorny, "Comment on "Effects of focused ion beam milling on the nanomechanical behavior of a molybdenum-alloy single crystal"," *Applied Physics Letters*, vol. 92, no. 9, 2008.

[124] J. Bohlen, F. Chmelík, P. Dobroň, D. Letzig, P. Lukáč, and K. U. Kainer, "Acoustic emission during tensile testing of magnesium AZ alloys," *Journal of alloys and compounds*, vol. 378, no. 1, pp. 214–219, 2004.

[125] P. Dobroň, F. Chmelík, J. Bohlen, K. Hantzsche, D. Letzig, and K. U. Kainer, "Acoustic emission study of the mechanical anisotropy of the extruded AZ31 alloy," *International Journal of Materials Research*, vol. 100, no. 6, pp. 888–891, 2009.

[126] Zs. Kovács, M. Ezzeldien, K. Máthis, P. Ispánovity, F. Chmelík, and J. Lendvai, "Statistical analysis of acoustic emission events in torsional deformation of a Vitreloy bulk metallic glass," *Acta Materialia*, vol. 70, pp. 113–122, 2014.

[127] C. B. Scruby, H. N. G. Wadley, K. Rusbridge, and D. Stockham-Jones, "Influence of microstructure on acoustic emission during deformation of aluminium alloys," *Metal Science*, vol. 15, no. 11-12, pp. 599–608, 1981.

[128] F. Diologent, R. Goodall, and A. Mortensen, "Surface oxide in replicated microcellular aluminium and its influence on the plasticity size effect," *Acta Materialia*, vol. 57, no. 1, pp. 286–294, 2009.

[129] B. D. Oakes in *Inhibitors in desalination systems* (C. C. Nathan, ed.), NACE, Houston, 1979.

[130] M. Knapek, P. Gabriel, R. Král, F. Chmelík, and P. Sladký, "Monitoring of the deformation of cereal grains by the acoustic emission technique," *Journal of Food & Nutrition Research*, vol. 54, no. 3, pp. 275–279, 2015.

[131] E. Pomponi and A. Vinogradov, "A real-time approach to acoustic emission clustering," *Mechanical Systems and Signal Processing*, vol. 40, no. 2, pp. 791–804, 2013.

[132] I. Orbulov and J. Ginsztler, "Compressive behaviour of metal matrix syntactic foams," *Acta Polytechnica Hungarica*, vol. 9, no. 2, pp. 43–56, 2012.

[133] J. Blaber, B. Adair, and A. Antoniou, "Ncorr: Open-source 2D digital image correlation Matlab software," *Experimental Mechanics*, vol. 55, no. 6, pp. 1105–1122, 2015.

[134] R. Harilal, "Adaptation of open source 2D DIC software ncorr for solid mechanics applications." `http://ncorr.com/download/publications/harilalapplication.pdf`, 2014. Accessed: 2016-06-23.

[135] L. J. Gibson and M. F. Ashby, *Cellular Solids: Structure and Properties (Cambridge Solid State Science Series)*. Cambridge University Press, 2 ed., 1999.

[136] E. Koza, M. Leonowicz, S. Wojciechowski, and F. Simančík, "Compressive strength of aluminium foams," *Materials Letters*, vol. 58, no. 1–2, pp. 132–135, 2004.

[137] C. San Marchi and A. Mortensen, "Deformation of open-cell aluminum foam," *Acta Materialia*, vol. 49, no. 19, pp. 3959–3969, 2001.

[138] A. Mortensen and M. C. Flemings, "Solidification of binary hypoeutectic alloy matrix composite castings," *Metallurgical and Materials Transactions A*, vol. 27, no. 3, pp. 595–609, 1996.

[139] H. Bart-Smith, A.-F. Bastawros, D. Mumm, A. Evans, D. Sypeck, and H. Wadley, "Compressive deformation and yielding mechanisms in cellular Al alloys determined using X-ray tomography and surface strain mapping," *Acta Materialia*, vol. 46, no. 10, pp. 3583–3592, 1998.

[140] L. Gibson, "Mechanical behavior of metallic foams," *Annual Review of Materials Science*, vol. 30, pp. 191–227, 2000.

[141] F. Diologent, R. Goodall, and A. Mortensen, "Activation volume in microcellular aluminium: Size effects in thermally activated plastic flow," *Acta Materialia*, vol. 59, no. 18, pp. 6869–6879, 2011.

[142] J.-F. Despois, R. Mueller, and A. Mortensen, "Uniaxial deformation of microcellular metals," *Acta Materialia*, vol. 54, no. 16, pp. 4129–4142, 2006.

[143] D. R. Lide, *CRC Handbook of Chemistry and Physics*. CRC Press, Boca Raton, Florida, 90 ed., 2009.

[144] D. W. Kaufmann, *Sodium chloride: the production and properties of salt and brine*. Reinhold Publishing, Michigan, 1960.

[145] J. R. Davis, ed., *Alloying: understanding the basics*. ASM International, Ohio, 2001.

[146] S. Kumar, *Fracture mechanics of nanoscale thin films*. PhD thesis, The Pennsylvania State University, USA, 2012.

[147] J. C. Grosskreutz and D. K. Benson, "The effects of the surface on the mechanical properties of metals," in *Surfaces and Interfaces II: Physical and Mechanical Properties* (J. J. Burke, N. L. Reed, and V. Weiss, eds.), pp. 61–94, Springer US, Boston, 1968.

[148] F. Chmelík, Z. Trojanová, Z. Převorovský, and P. Lukáč, "The Portevin-Le-Chatelier effect in Al-2.92-percent-Mg-0.38-percent-Mn alloy and linear location of acoustic emission," *Materials Science and Engineering: A*, vol. 164, no. 1-2, pp. 260–265, 1993.

[149] F. Chmelík, J. Balík, P. Lukáč, and E. Pink, "The Portevin-Le Chatelier effect in an AlZn10 alloy investigated by the acoustic emission technique," *Kovové Materiály - Metallic Materials*, vol. 36, no. 1, pp. 10–14, 1998.

[150] F. Chmelík, F. B. Klose, H. Dierke, J. Šachl, H. Neuhäuser, and P. Lukáč, "Investigating the Portevin–Le Châtelier effect in strain rate and stress rate controlled tests by the acoustic emission and laser extensometry techniques," *Materials Science and Engineering: A*, vol. 462, no. 1–2, pp. 53–60, 2007.

[151] Z. Kovács, F. Chmelík, J. Lendvai, and P. Lukáč, "Acoustic emission due to Portevin-Le Chatelier instabilities in load rate controlled experiments," *Kovové Materiály - Metallic Materials*, vol. 40, no. 5, pp. 298–306, 2002.

[152] I. V. Shashkov, M. A. Lebyodkin, and T. A. Lebedkina, "Multiscale study of acoustic emission during smooth and jerky flow in an AlMg alloy," *Acta Materialia*, vol. 60, no. 19, pp. 6842–6850, 2012.

[153] R. K. Miller, *Nondestructive Testing Handbook: Vol. 5 - Acoustic Emission Testing*. American Society for Nondestructive Testing, Ohio, 2nd ed., 1987.

[154] A. Vinogradov, D. L. Merson, V. Patlan, and S. Hashimoto, "Effect of solid solution hardening and stacking fault energy on plastic flow and acoustic emission in Cu–Ge alloys," *Materials Science and Engineering: A*, vol. 341, no. 1, pp. 57–73, 2003.

[155] A. Vinogradov, M. Nadtochiy, S. Hashimoto, and S. Miura, "Acoustic emission spectrum and its orientation dependence in copper single crystals," *Materials Transactions, JIM*, vol. 36, no. 4, pp. 496–503, 1995.

[156] M. A. Lebyodkin, I. V. Shashkov, T. A. Lebedkina, K. Máthis, P. Dobroň, and F. Chmelík, "Role of superposition of dislocation avalanches in the statistics of acoustic emission during plastic deformation," *Physical Review E*, vol. 88, no. 4, p. 042402, 2013.

[157] A. Vinogradov and A. Lazarev, "Continuous acoustic emission during intermittent plastic flow in α-brass," *Scripta Materialia*, vol. 66, no. 10, pp. 745–748, 2012.

[158] P. Bak, C. Tang, and K. Wiesenfeld, "Self-organized criticality," *Physical review A*, vol. 38, no. 1, p. 364, 1988.

[159] D. Rouby, P. Fleischmann, and C. Duvergier, "An acoustic emission source model for both continuous and burst-type emission analysis: 1. Theory," *Philosophical Magazine A*, vol. 47, no. 5, pp. 671–687, 1983.

[160] A. Clauset, C. R. Shalizi, and M. E. J. Newman, "Power-law distributions in empirical data," *SIAM Review*, vol. 51, no. 4, pp. 661–703, 2009.

List of Figures

List of Tables

List of Abbreviations and Symbols

AE	acoustic emission
Al2Mg	aluminum containing 2 wt. % of magnesium
ASK	Adaptive Sequential k-means algorithm
bcc	body-centered cubic lattice
DIC	digital image correlation
EBSD	electron back-scattered diffraction
EDM	electric discharge machining
fcc	face-centered cubic lattice
FFT	fast Fourier transform
FIB	focused ion beam
HDT	hit definition time
HLT	hit lockout time
MMS	metal matrix syntactic foam
NDT	non-destructive technique
PEP	piezoelectric positioning stage
PLC	Portevin-Le Châtelier effect
PSD	power spectral density
RMS	root mean square
SEM	scanning electron microscope
STFT	short-time Fourier transform
A_0	initial crystal cross-section perpendicular to the loading direction
b	Burgers vector
c	empirical constant of the size effect
c_L	longitudinal wave velocity
c_T	transversal wave velocity
CTE	coefficient of thermal expansion
d	microsample diameter
d_p	pore diameter
D	depth of dislocation loop below the surface
$\mathrm{dB_{AE}}$	preamplifier gain in dB
e	spring elongation
E	AE signal energy
f	signal frequency
f_k	AE signal in frequency domain
f_{med}	median frequency
$f(t)$	AE signal in time domain
F	force

G	shear modulus
l	average surface-to-surface mean free path
m	power-law exponent of the size effect
n	number of dislocation loops
$P(f)$	power spectral density
r	final radius of dislocation loop
s	spring stiffness
U_0	threshold voltage
U	maximum amplitude of the AE event
v	velocity of dislocation loop growth
V_s	volume fraction of solid
x	PEP stage displacement
Δy	surface displacement
α_T	correction factor in Taylor hardening
ε	engineering strain
$\Delta\varepsilon$	strain increment caused by the dislocation avalanche
λ	angle between the slip direction and the tensile axis
ϕ	angle between the normal of the slip plane and the tensile axis
ρ_d	density of dislocations
σ_0	intrinsic flow stress of dense metal with low dislocation density
σ^*	foam flow stress
τ_0	friction stress within the crystal
τ	critical resolved shear stress

Attachments

Important Matlab evaluation scripts

Collecting stress drops

```
function [dropsAll dropsT dropsTs dropsS]=LDE(Time,EngStress)
% load drops evaluation

dropTresh=0.001;

count=0;
dropStress=0;
dropTime=0;

x=EngStress;

j=0;
k=0;

lngth=length(x);

for i=1:lngth-1 % finds load drops

    if x(i)>x(i+1)
        dropStress=dropStress+x(i)-x(i+1);
        count=count+1; % increases size
        dropTime=dropTime+Time(i);

        if k==0
            TimeStart=Time(i);
        end;

        k=1;

    else   % if the drop is ended
        if count>0
            j=j+1;
            dropsS(j)=dropStress;
            dropsT(j)=dropTime/count;
            dropsTs(j)=TimeStart;
            k=0;
        end;
        count=0;
```

```
39          dropStress=0;
40          dropTime=0;
41      end
42
43      if i==lngth-1 && count>0 % saves the last drop
44          j=j+1;
45          dropsS(j)=dropStress;
46          dropsT(j)=dropTime/count; % time "in the middle" of
                the drop
47          dropsTs(j)=TimeStart; % time when the drop starts
48          count=0;
49      end;
50  end
51
52  dropsS=dropsS';
53  dropsT=dropsT';
54  dropsTs=dropsTs';
55
56  dropVec=dropsS; % saves also filtered-out drops
57
58  if exist('dropTresh','var')
59      ind=find(dropsS>dropTresh);
60      dropsS=dropsS(ind);
61      dropsT=dropsT(ind);
62      dropsTs=dropsTs(ind);
63  end;
64
65  dropsAll=dropVec;
66
67  end
68
69  % Michal Knapek 01/2016
```

AE events merging

```
1  function [MevTime MevC1 MevDur MevAmpl count timeDifference] =
       mergeEv(evTimeSec,evC1,evDur,evAmpl);
2  % Merges neighboring events within a defined interval (limit)
3
4  limit = 0.1; % seconds
5
6  cnt=0;
7  timeDiff=0;
8  count=[0 0];
9  timeDifference=[0 0];
```

```
10
11 for i=1:length(evTimeSec)
12
13     if i==1
14         MevTime(i)=evTimeSec(i);
15         MevC1(i)=evC1(i);
16         MevDur(i)=evDur(i);
17         MevAmpl(i)=evAmpl(i);
18     else
19
20         if (evTimeSec(i)-evTimeSec(i-1))<limit
21
22             MevTime(i)=evTimeSec(i);
23             MevC1(i)=MevC1(i-1)+evC1(i);
24             MevDur(i)=MevDur(i-1)+evDur(i);
25             MevAmpl(i)=MevAmpl(i-1)+evAmpl(i);
26
27             cnt=cnt+1;
28             count(i)=count(i-1)+cnt;
29
30             timeDiff=evTimeSec(i)-evTimeSec(i-1);
31             timeDifference(i)=timeDifference(i-1)+timeDiff;
32
33             MevTime(i-1)=NaN; % if merging occurs,
34             MevC1(i-1)=NaN; % former event is marked and ==>
35             MevDur(i-1)=NaN;
36             MevAmpl(i-1)=NaN;
37             count(i-1)=NaN;
38             timeDifference(i-1)=NaN;
39         else
40             MevTime(i)=evTimeSec(i);
41             MevC1(i)=evC1(i);
42             MevDur(i)=evDur(i);
43             MevAmpl(i)=evAmpl(i);
44
45             cnt=0;
46             count(i)=cnt;
47
48             timeDiff=0;
49             timeDifference(i)=timeDiff;
50         end;
51     end;
52 end;
53
54 MevTime(isnan(MevTime))=[]; % ==> ...deleted.
```

```
MevC1(isnan(MevC1))=[];
MevDur(isnan(MevDur))=[];
MevAmpl(isnan(MevAmpl))=[];
count(isnan(count))=[];
timeDifference(isnan(timeDifference))=[];

MevTime=MevTime';
MevC1=MevC1';
MevDur=MevDur';
MevAmpl=MevAmpl';
count=count';
timeDifference=timeDifference';

end

% Michal Knapek 02/2016
```

Assigning the stress drops to the AE events

```
function [dropTimeOut,dropStressOut] = LDEfind(MevTime,...
dropTime,dropStress,timeDifference)

interval = 0.15; % must be >= "limit" in the mergeEv function
% countFilter = 1;
% evTime=evTime(evTime>countFilter);

evTime=MevTime;

dropTimeOut=zeros(1,length(evTime)); % preallocation
dropStressOut=zeros(1,length(evTime));

for i=1:length(evTime)
    pom = find(dropTime < (evTime(i)+interval) & ...
        dropTime > (evTime(i)-interval-timeDifference(i)));

    x=dropTime(pom);
    y=dropStress(pom);

    if isempty(x)
        x=0;
        y=0;
    else
        x=mean(x)-timeDifference(i);
        y=sum(y);
    end;
```

```
27
28          dropTimeOut(i)=x;
29          dropStressOut(i)=y;
30  end;
31
32  dropTimeOut=dropTimeOut';
33  dropStressOut=dropStressOut';
34
35  % dropStressOut(dropStressOut==0)=[];
36  % dropTimeOut(dropTimeOut==0)=[];
37
38  end
39
40  % Michal Knapek 01/2016
```